Molecular Mechanism of the Hsf1-Chaperone System Responsible for Proteostasis

タンパク質恒常性の維持を担う
Hsf1-シャペロンシステムの分子機構解明

Soichiro Kawagoe

川越　聡一郎

Graduate School of Chemical Sciences and Engineering
Hokkaido University

北海道大学　大学院総合化学院

2023

ACKNOWLEDGEMENTS

I would like to express my sincere gratitude to Professor Koichiro Ishimori. He always gave me the continuous guidance, fruitful discussion, and hearty encouragement. I am also pleased to thank Secretary Maki Tanaka for accepting the troublesome office procedure, and the members of Structural Chemistry Laboratory for helps and assistance.

From September 2020, I have been conducting research at Tokushima University as a special research student. I sincerely appreciate Professor Tomohide Saio for his passionate guidance and kind advice. I also thank the previous and current members of Molecular Life Science Laboratory for helps and assistances, especially Dr. Motonori Matsusaki, Dr. Munehiro Kumashiro, Dr. Asuka Mukai, Dr. Yoshikazu Hattori, Ms. Eri Sakamoto, Ms. Miki Sanada, Ms. Honoka Kawamukai, and Mr. Ryowang Ko for contributing to this work.

It should be emphasized that the studies in this thesis have required the cooperation with many investigators. I wish to express sincere appreciation to Dr. Hiroyuki Kumeta (Hokkaido University) for the assistance with NMR measurements. I would like to express my special gratitude to Dr. Hiroshi Nakagawa (Japan Atomic Energy Agency) and Dr. Takuya Mabuchi (Tohoku University) for the fruitful discussion from the viewpoint of computational methods.

At the review of this work, Professor Kazuyasu Sakaguchi (Laboratory of Biological Chemistry), Professor Kazuki Sada (Material Chemistry Laboratory), and Professor Manabu Tokeshi (Laboratory of Bioanalytical Chemistry) gave me the valuable suggestion and guidance.

I have received a generous support from Japan Society for the Promotion of Science (JSPS) Research Fellowship DC1 since April 2020. This work was financially

supported by a Grants-Aid for Scientific Research.

I express my deep appreciation to my family. They always encouraged me. Finally, I would like to express my gratitude to Dr. Reimi Suzuki for her emotional support.

March 2023

Graduate School of Chemical Sciences and Engineering,

Hokkaido University

Soichiro Kawagoe

LIST OF PUBLICATIONS

CHAPTER II

"Structural insight into proline *cis/trans* isomerization of unfolded proteins catalyzed by the trigger factor chaperone"

Soichiro Kawagoe, Hiroshi Nakagawa, Hiroyuki Kumeta, Koichiro Ishimori, Tomohide Saio

J. Biol. Chem., **293**, 15095-15106 (2018).

CHAPTER III

"Heat-induced conformational transition mechanism of heat shock factor 1 investigated by tryptophan probe"

Soichiro Kawagoe, Munehiro Kumashiro, Takuya Mabuchi, Hiroyuki Kumeta, Koichiro Ishimori, and Tomohide Saio

Biochemistry, **61**, 2897-2908 (2022).

CHAPTER IV

"Phase Separation Mediated by α-Helical Structure in the Hsf1 intrinsically disordered domain"

Soichiro Kawagoe, Hiroyuki Kumeta, Koichiro Ishimori, and Tomohide Saio

Manuscript in preparation

CHAPTER V

"Oxidative hyperoligomerization drives phase transition of heat shock factor 1"

Soichiro Kawagoe, Motonori, Matsusaki, Takuya Mabuchi, Hiroyuki Kumeta, Koichiro Ishimori, and Tomohide Saio

Nat. commun., to be submitted

OTHER PUBLICATIONS

"Oligomerization of a molecular chaperone modulates its activity"

Tomohide Saio, Soichiro Kawagoe, Koichiro Ishimori, Charalampos G. Kalodimos

eLife, **7**, e35731 (2018).

"Regulation of Liquid-Liquid Phase Separation by Molecular Chaperones"

Soichiro Kawagoe, Eiichiro Mori, Tomohide Saio

Thermal Med., **37**, 31-44 (2021).

"Structural and Kinetic Views of Molecular Chaperones in Multidomain Protein Folding"

Soichiro Kawagoe, Koichiro Ishimori, Tomohide Saio

Int. J. Mol. Sci., **23**, 2485 (2022).

"Peptide-to-Small Molecule: A Pharmacophore-Guided Small Molecule Lead Generation Strategy from High-Affinity Macrocyclic Peptides"

Shuhei Yoshida, Shota Uehara, Noriyasu Kondo, Yu Takahashi, Shiho Yamamoto, Atsushi Kameda, Soichiro Kawagoe, Naoko Inoue, Masami Yamada, Norito Yoshimura, Yuki Tachibana

J. Med. Chem., **65**, 10655-10673 (2022).

LIST OF PRSENTATIONS

Oral Presentations

1. Soichiro Kawagoe, Tomohide Saio, Koichiro Ishimori

   "The mode of action of proline *cis-trans* isomerization by trigger factor chaperone"

   The Meeting in Winter 2016 of the Hokkaido Branch of the Chemical Society of Japan (Sapporo, Japan) January 19, 2016

2. Soichiro Kawagoe, Motonori Matsusaki, Koichiro Ishimori, Tomohide Saio

   "Oxidative phase transition of heat shock factor-1 droplet driven by higher-order oligomerization"

   The 22nd Annual Meeting of the Protein Science Society of Japan (Tsukuba, Japan) June 7, 2022

3. Soichiro Kawagoe

   "The liquid-liquid phase separation mechanism of heat shock factor 1 using spectroscopic measurements"

   The 48th Seminar of Institute of Advanced Medical Sciences Tokushima University (Tokushima, Japan) September 15, 2022

Poster Presentations

1. Soichiro Kawagoe, Tomohide Saio, Hiroyuki Kumeta, Fuyuhiko Inagaki, Koichiro Ishimori

   "Proline *cis-trans* isomerase activity of Trigger Factor chaperone as investigated by NMR"

   The 16th Annual Meeting of the Protein Science Society of Japan (Fukuoka, Japan) June 7, 2016

2. Soichiro Kawagoe, Tomohide Saio, Hiroyuki Kumeta, Fuyuhiko Inagaki, Koichiro Ishimori

   “Proline *cis-trans* Isomerase Activity of Trigger Factor Chaperone as Investigated by NMR”

   The 17th International Conference on Magnetic Resonance in Biological Systems, (Kyoto, Japan) August 23, 2016

3. Soichiro Kawagoe, Tomohide Saio, Hiroyuki Kumeta, Fuyuhiko Inagaki, Koichiro Ishimori

   “Proline *cis/trans* isomerase activity of Trigger Factor chaperone as investigated by NMR”

   The 12th Annual Meeting of Japanese Society for Chemical Biology (Sapporo, Japan) June 8, 2017

4. Soichiro Kawagoe, Hiroshi Nakagawa, Hiroyuki Kumeta, Koichiro Ishimori, Tomohide Saio

   “The catalytic mechanism of a PPIase chaperone investigated by the structural analysis at the transition state using NMR and MD simulation”

   The 20th Annual Meeting of the Protein Science Society of Japan (Osaka, Japan) July 28, 2020

5. Soichiro Kawagoe, Hiroshi Nakagawa, Hiroyuki Kumeta, Koichiro Ishimori, Tomohide Saio

   “Structural Dynamics of the Trigger Factor Chaperone Regulating Proline *cis/trans* Isomerization in Protein Folding”

   The 22nd International Society of Magnetic Resonance Conference (ISMAR-APNMR 2021) (Online) August 24, 2021

6. Soichiro Kawagoe, Motonori Matsusaki, Koichiro Ishimori, Tomohide Saio
   “Redox-dependent phase transition mechanism of Heat shock factor 1”
   The 45th Annual Meeting of the Molecular Biology Society of Japan (Yokohama, Japan) December 2, 2021

7. Soichiro Kawagoe, Hiroshi Nakagawa, Hiroyuki Kumeta, Koichiro Ishimori, Tomohide Saio
   “Structural insight into molecular recognition and catalytic mechanism of trigger factor chaperone in proline *cis/trans* isomerization”
   The International Chemical Congress of Pacific Basin Societies 2021 (Online) December 19, 2021

Contents

CHAPTER I

General Introduction

1.1. Hsf1-Chaperone System for Maintaining Proteostasis

Protein supports the basis of biological activities in the body. The homeostasis of protein dynamics called as “proteostasis”, such as synthesis, structure formation, and degradation, must be always maintained for proteins to function properly. However, cells are exposed to a variety of stressful environments, including heat, reactive oxygen species, and pH changes throughout their lifetime, then stress often induces the proteins to misfold and aggregate (Figure 1.1, upper panel), compromising the homeostasis of the cellular proteome [1].

The systems for maintaining the proteostasis are equipped in living cell even under stressed conditions. Typical systems include ribosome-associated quality control[2] for synthesis, Heat shock factor 1 (Hsf1) - chaperone system[3–5] and endoplasmic reticulum (ER) - quality control[6] for folding, and the ubiquitin-proteasome system[7] and ER-associated degradation[8] for degradation. Especially, Hsf1 - chaperone system[3–5] supports the protein folding at nucleus and cytosol. In this system, molecular chaperones suppress the protein aggregation and helps the protein folding [9,10]. Hsf1 upregulates the transcriptional level of these chaperones by sensing several stresses [11]. Therefore, Hsf1-chaperone system consists of chaperone, which functions as “player” to directly assist in substrate folding, and Hsf1, which acts as “operator” to control the amount of chaperone for maintaining the protein folding state under stress. Protein folding assistance by the Hsf1-chaperone system is crucial for the maintenance of biological activities because proteins get their functions by folding their own unique conformations, and the disruption of Hsf1-chaperone system is associated with diseases[12]. While this system is responsible for protecting normal cells from stress, the increased Hsf1 activity linked to malignancy and a poor prognosis of many cancers[13–15]. On the other hand, neurodegenerative diseases such as Alzheimer's disease and Parkinson's disease are associated with low Hsf1 activity[16]. Thus, from a clinical perspective, Hsf1-chaperone system is important in proteostasis. In this thesis, to elucidate the molecular mechanism of the Hsf1-chaperone

system, I focused on two reactions that occur within this system: (1) substrate protein folding assistance by chaperone (section 1.2) (Figure 1.1, center panel), and (2) transcriptional regulation of Hsf1 via stress-sensing assembly state changes (section 1.3-1.6) (Figure 1.1, bottom panel).

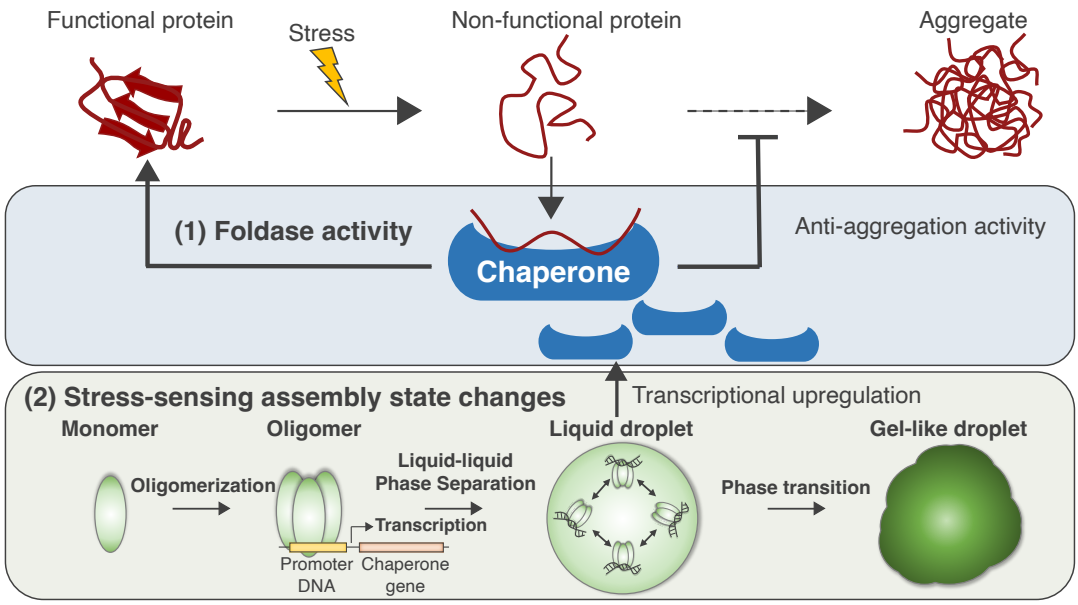

Figure 1.1 Hsf1 chaperone system
(Upper panel) Under stress, proteins often unfold and aggregate. (Center panel) Molecular chaperone assists the protein folding and suppresses the aggregation. (Bottom panel) Transcriptional activity of hsf1 links to its assembly state. The assembly of Hsf1 proceeds by stress-dependent manner. While Monomer is transcriptional inactivated state, oligomer and liquid droplet state is active. The transcriptional activity is decreased at Gel-like droplet.

1.2. Foldase Activity of Chaperone by Catalyzing the Proline *cis/trans* Isomerization (Chapter II)

In Hsf1-chaperone system, molecular chaperones are responsible for directly assistance to substrate protein folding. Assistance in the productive folding of substrate protein is achieved by the anti-aggregation activity and foldase activity, which accelerates the protein folding, of molecular chaperones. Of these two activities, with regards to anti-aggregation activity, most of the mechanism has been revealed. Environmental changes such as stress often break the protein structure, and hydrophobic regions, which normally encapsulated in the protein core, exposes to the solvent. Such hydrophobic regions can

cause nonspecific intermolecular interactions that drive aggregation. Molecular chaperones suppress such nonspecific hydrophobic interactions by interacting these hydrophobic regions and protect them from aggregation[17–19].

While the anti-aggregation mechanism of molecular chaperone is becoming clear, the foldase mechanism, how chaperone acts on the substrate to promote its folding from the substrate-bound state, is still unknown. In the foldase activity of molecular chaperone, the catalysis of peptidyl-prolyl *cis/trans* isomerization can be a key reaction. Because specific *cis/trans* conformations of peptide bonds are required in the native fold (Figure 1.2A), proline *cis/trans* isomerization can be a rate-limiting step in protein folding. Several molecular chaperones have peptidyl-prolyl *cis/trans* isomerase (PPIase) domain, which catalyses the proline *cis/trans* isomerization, for foldase activity (Figure. 1.2B). For example, Trigger Factor (TF), SurA, and PrsA contain the PPIase domain[20–23]. Heat shock protein 90 forms a complex with the PPIases FKBP51 and FKBP52 and use them as a functional module to promote substrate protein folding [24–26]. Then, I focused on PPIase activity for understanding the foldase mechanism of molecular chaperones. PPIase could act as a foldase by catalyzing the isomerization of proline, the rate-limiting step in protein folding, but which proline of the substrate protein PPIase targets and how it catalyzes is not yet elucidated. Further insight into the structure of the PPIase in complex with the client protein both at the ground state and at the transition state of isomerization is required because the lack of a comprehensive structural study that can track the entire *cis/trans* isomerization process has hindered the elucidation of the mechanism.

In chapter II, to unveil the molecular mechanism of PPIase, I conducted an integrated study on PPIase domain of TF chaperone exploiting solution NMR, molecular dynamics (MD) simulation, and activity assay. NMR structure analysis revealed that TF PPIase recognizes the proline-aromatic amino acid sequence and MD simulation analysis revealed stabilization of the intermediate transition state by the formation of intermolecular hydrogen bonds, which lowers the energy barrier of the transition state and catalyzes isomerization. Based on knowledge about binding specificity and catalytic mechanism from the results, I discuss the mechanism how PPIase domain of molecular chaperone acts as a foldase.

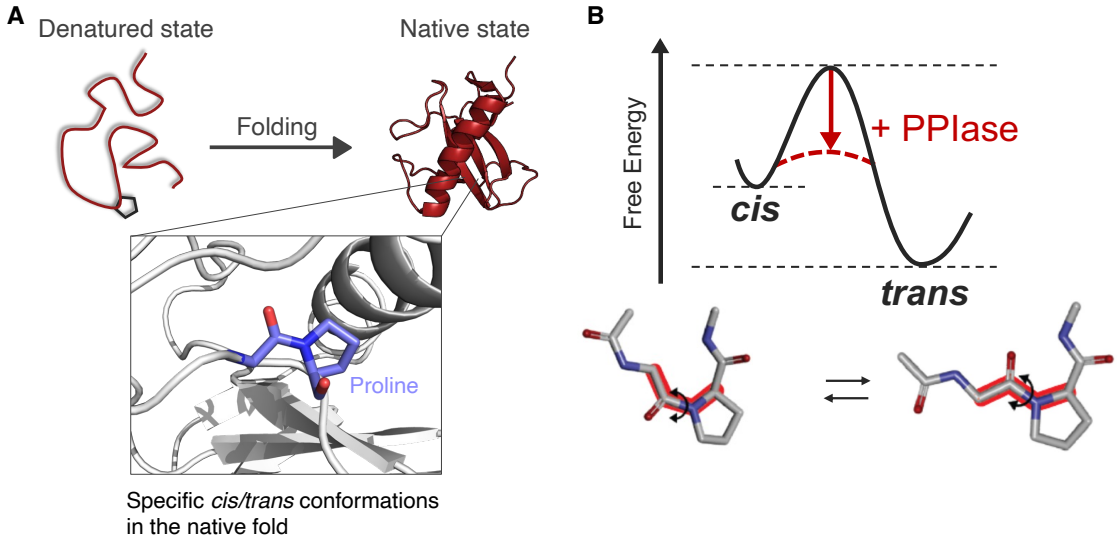

Figure 1.2 Proline *cis/trans* isomerization in protein folding
(A) Specific proline *cis/trans* conformations of peptide bonds are required in the native fold. (B) PPIase lowers the activation energy of proline *cis/trans* isomerization.

1.3. Functional Regulation of Hsf1 by the Assembly State Changes

The importance of the activity regulation of molecular chaperones in maintaining proteostasis has been described above. Since the amount of misfolded protein increases during stress, the Hsf1-chaperone system takes a countermeasure by upregulating the amount of chaperones having foldase function to prevent the accumulation of misfolded protein in the cell. In all eukaryotic cells, Hsf1 is responsible for transcriptional regulation

of the molecular chaperones[11,27]. The transcriptional activity of Hsf1 is regulated by its assembly state changes. Therefore, understanding the mechanism of Hsf1 assembly state changes is essential to clarify transcriptional regulation by Hsf1 in the Hsf1-chaperone system.

Hsf1 takes four states: monomer, oligomer, liquid droplet, and gel-like droplet. Under normal conditions, Hsf1 exists in transcriptionally inactivated monomeric state in cytosol. When Hsf1 senses stress, it translocates into the nucleus and forms oligomer (Figure 1.3). The Hsf1 oligomer binds to the heat shock element (HSE) DNA, which is comprised of at least three nGAAn repeats organized head to tail in the promoters of genes encoding chaperones, and promotes the transcription[28–30]. By forming the oligomer, the affinity of Hsf1 for the HSE increases as each Hsf1 of the trimer binds to a nGAAn repeat.

As the assembly progresses further, Hsf1 forms liquid droplets called Hsf1 foci by the liquid-liquid phase separation (LLPS) of Hsf1[31] around HSE. LLPS is a phenomenon in which specific biomolecules accumulate and are isolated from their surroundings while maintaining internal mobility through weak interactions[32]. Droplets formed by LLPS are loosely isolated from the surrounding environment but can rapidly assemble and dissolve by sensing the surrounding environment such as temperature and pH[33]. The Hsf1 foci is formed in a stress level-dependent manner, and the transcription of molecular chaperones are promoted in the Hsf1 foci[31] (Figure 1.3). Hsf1 also forms nuclear stress bodies (nSBs) on the satellite III (sat III) DNA, which is comprised of long nGAAn repeats organized head to head and encodes non-coding sat III RNA[34–36]. Although the function of the nSBs has not been clear in many aspects, it is shown that several splicing factors and co-activator of transcriptional factors are assembled in nSBs to promote the expression of the proteins required in the recovery stage[37–39]. It has been proposed that nSBs not only protect these molecules from stress by isolating them internally, but also play a role in suppressing the production of non-HSP transcripts to

preferentially synthesize HSPs under stress[39] (Figure 1.3).

Hsf1 foci and nSBs are transiently formed as membrane-less organelles that are generated under proteotoxic stress conditions and are resolved as the cell recovers from the stress[28,40,41]. Conversely, under prolonged stress, these liquid droplets undergo decreased internal-mobility and liquid-to-gel–like phase transition, which has been linked to downregulation of chaperones and mediate apoptosis[31,42]. While the mechanism that the phase transition of Hsf1 droplet induces apoptosis is not entirely clear, the maturation of caspase-9 by the downregulation of molecular chaperones, which suppress the apoptosis by forming the complex with Apaf-1 and cytochrome *c*[43] may leads to apoptosis. And, the remaining trapped of several splicing factors, required at the stress recovery stage, in gel-like nSBs could also be the reasons for apoptosis. Therefore, Hsf1 has opposing effects on cells by changing its own assembly state in a stress level-dependent manner, protects cells via upregulation of molecular chaperones in the liquid droplet state but mediates apoptosis by downregulation of molecular chaperones in the gel-like droplet state (Figure 1.3).

Hsf1 state change can be divided into the following three transition steps: oligomerization, LLPS, and phase transition to gel-like droplet (Figure 1.4). It is important to uncover the mechanism of these three steps to elucidate the regulatory mechanism of Hsf1 transcriptional activity. However, the current understanding of the HSR system is limited to the phenomenological level using cell biological techniques, and the molecular mechanism of how Hsf1 senses stress at the molecular level and how regulates its own assembly state remain to be elucidated. For elucidating the regulatory mechanism of Hsf1 assembly state, in this thesis, I focused on transition steps, monomer/oligomer, oligomer/liquid droplet, and liquid droplet/gel-like droplet (Figure 1.4).

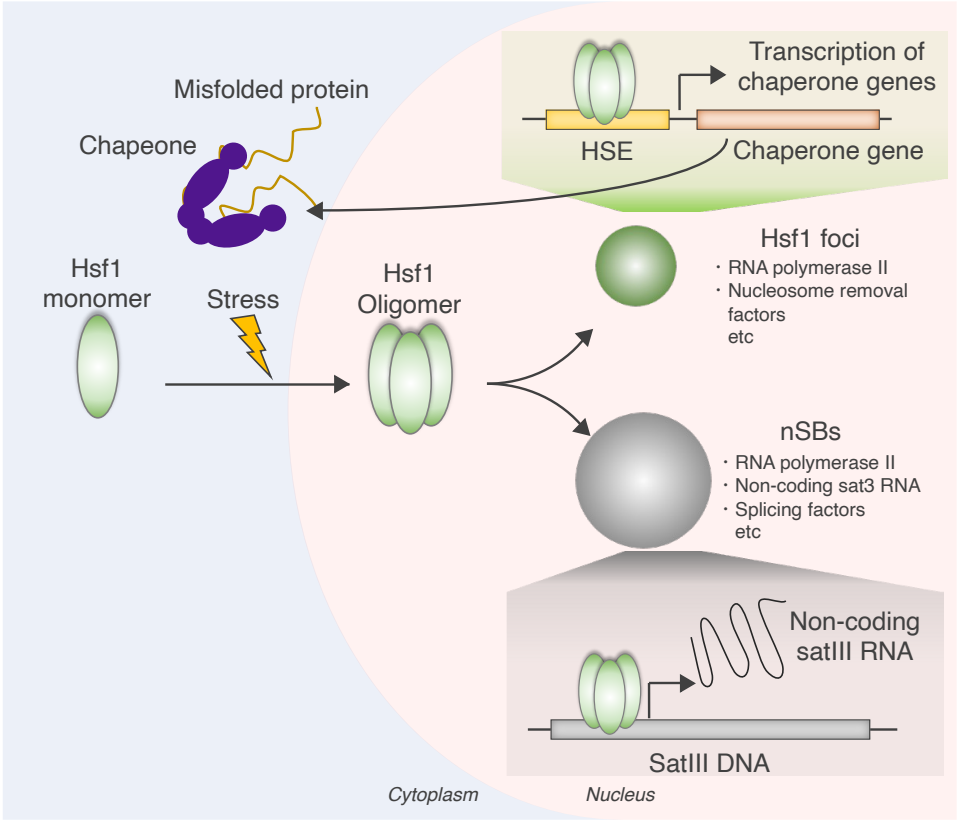

Figure 1.3 Hsf1 droplets in the nucleus

Under physiological conditions, Hsf1 is located at the cytoplasm with molecular chaperone. Under stress, Hsf1 translocate to the nucleus and oligomerizes. Hsf1 forms two distinct droplets. One is nSBs formed around satIII DNA, which promotes the synthesis of non-coding satIII RNA. The other is Hsf1 foci, which forms around HSE and promotes chaperone gene transcription inside the droplet.

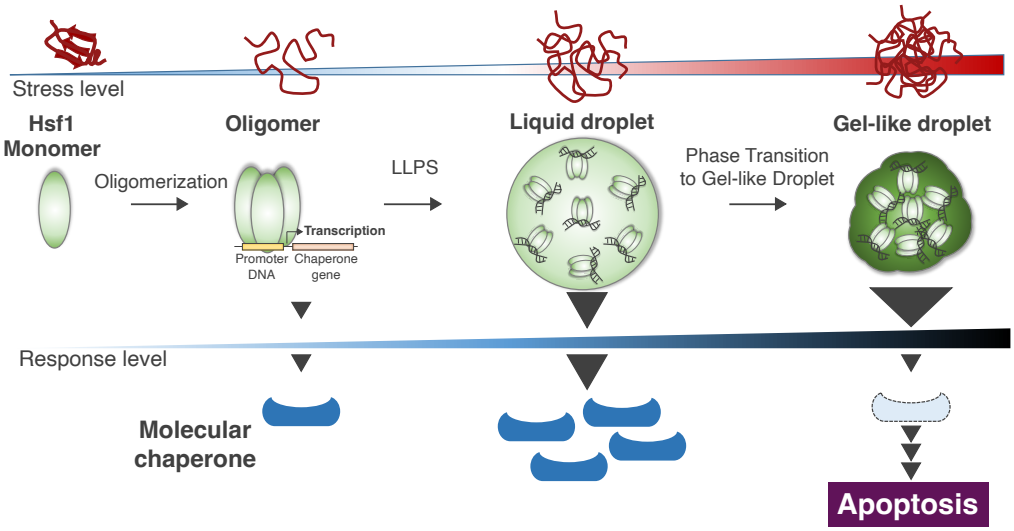

Figure 1.4 The assembly state changes of Hsf1

Hsf1 changes its assembly state, monomer/oligomer, oligomer/liquid droplet, and liquid droplet/gel-like droplet, depending on the stress level. Oligomer and liquid droplet states have a protective function for cells, but cells with gel-like droplets are induced to apoptosis.

1.4. Heat-induced Conformational Transition and Oligomerization of Hsf1 (Chapter III)

The function of Hsf1 is controlled by its assembly state. Within this assembly event, oligomerization is its first step. Hsf1 exists in monomeric state under normal conditions, and becomes oligomer formed by intermolecular interaction between its leucine zipper domain (LZ1-3) upon elevation of temperature from 37°C to 42°C in the cell [28–30]. Although this heat-induced oligomerization is the first step in the series of transcriptional regulation of Hsf1, its monomeric structure has not been experimentally determined, and the oligomerization mechanism has not been fully elucidated since the majority of Hsf1 structure consists of intrinsically disordered region (IDR).

In this chapter, I aimed to uncover the heat-induced oligomerization mechanism of Hsf1. First, the monomeric structure of Hsf1 was estimated using the structure prediction program AlphaFold2[44] and molecular dynamics (MD) simulation, and it was shown that the monomer forms closed state, which LZ1-3 and a short leucine zipper domain (LZ4) interacts intramolecularly. To trace the oligomerization process, I performed Trp and ANS fluorescence experiments, and the results showed that Hsf1 does not just undergo a simple monomer/oligomer change, but also oligomerizes via open conformational intermediate, where the intramolecular LZ interaction is dissolved, as the temperature increases. Furthermore, circular dichroism spectroscopy and MD simulation experiments showed that this tertial conformational change is coupled with the unfolding of LZ4. Based on these experimental analyses, I discussed the heat-induced conformational transition and oligomerization mechanism of Hsf1 and the functional significance of its intermediate.

1.5. Liquid-liquid Phase Separation of Hsf1 (Chapter IV)

In Chapter III, I analyzed the mechanism by which Hsf1 senses heat stress and oligomerizes. In the cell, Hsf1 further assembles to form Hsf1 droplets such as Hsf1 foci around HSE DNA and nSBs around sat III DNA. The transcriptional activity of Hsf1 is

further enhanced in Hsf1 foci and nSBs could protect several molecules from stress by isolating them internally. Thus, the droplet formation via LLPS of Hsf1 is crucial in the transcriptional activation of Hsf1, however, it is unknown what environmental changes promote Hsf1 interactions and droplet formation.

In this chapter, to uncover the LLPS mechanism of Hsf1, I investigated the environmental condition in which Hsf1 droplets form and the interaction mechanisms driving the LLPS of Hsf1. Since acidification is often induced in heat-stressed cells[45–47], we hypothesized that droplet formation of Hsf1 proceeds by acidification. Therefore, we performed turbidity measurements and microscopic observations that could track Hsf1 droplet formation, and found increased turbidity and droplet formation below pH 6.0. To clarify the mechanism of droplet formation by acidification, I traced the structural changes of Hsf1 by solution NMR and CD measurements, and found that LZ4, denatured at high temperature at neutral pH, forms a secondary structure at acidic pH, and the formation of Hsf1 droplets proceeds by the intermolecular interaction between the structured LZ4. Furthermore, FKBP52, a PPIase that interacts with Hsf1 in the cell, also promotes LLPS of Hsf1, suggesting that PPIase activity promotes Hsf1 assembly and enhances the transcriptional activity of Hsf1 during stress.

1.6. Liquid-to-gel Phase Transition of Hsf1 (Chapter V)

I revealed that Hsf1 forms liquid droplets via liquid-liquid phase separation under acidic or crowding condition in Chapter IV. Under prolonged stress, Hsf1 foci and nSBs undergo decreased fluidity and liquid-to-gel–like phase transition, which has been linked to down-regulation of chaperones and mediate apoptosis. The liquid-to-gel–like phase transition of Hsf1 may be the key response in cell fate decision, but the mechanisms of phase transition of Hsf1 droplet in response to stress remain to be elucidated.

In Chapter V, I investigated the condition and the mechanism that Hsf1 undergoes phase transition into gel-like condensates. The mechanism for phase transition of the Hsf1

liquid droplets were investigated by observation of the internal architecture of the Hsf1 droplets by holotomography imaging, corroborated by biophysical and biochemical experiments. The data showed that oxidative condition promotes the phase transition to gel-like state of Hsf1 droplet. In the oxidative condition, Hsf1 forms higher-order oligomer mediated by the disulfide-bond, and such oligomer leads the more condensed droplet.

In summary, to elucidate the molecular mechanism of the Hsf1-chaperone system, I focused on two points in this thesis.

(1) Molecular mechanism of PPIase playing an important role in foldase activity of chaperone (Chapter II).

(2) Mechanisms of conformational changes and intermolecular interactions that regulates the stress-induced Hsf1 assembly state changes (Chapter III, IV, and V)

References

1. Gasch, A. P. *et al.* Genomic expression programs in the response of yeast cells to environmental changes. *Mol. Biol. Cell* **11**, 4241–4257 (2000).
2. Joazeiro, C. A. P. Mechanisms and functions of ribosome-associated protein quality control. *Nat. Rev. Mol. Cell Biol.* **20**, 368–383 (2019).
3. Jolly, C. & Morimoto, R. I. Role of the Heat Shock Response and Molecular Chaperones in Oncogenesis and Cell Death. *J. Natl. Cancer Inst.* **92**, 1564–1572 (2000).
4. Vihervaara, A. *et al.* Transcriptional response to stress is pre-wired by promoter and enhancer architecture. *Nat. Commun.* **8**, 1–16 (2017).
5. Mahat, D. B., Salamanca, H. H., Duarte, F. M., Danko, C. G. & Lis, J. T. Mammalian Heat Shock Response and Mechanisms Underlying Its Genome-wide Transcriptional Regulation. *Mol. Cell.* **62**, 63–78 (2016).
6. Araki, K. & Nagata, K. Protein Folding and Quality Control in the ER. *Cold Spring Harb. Perspect. Biol.* **3**, a007256 (2011).
7. Tai, H. C. & Schuman, E. M. Ubiquitin, the proteasome and protein degradation in neuronal function and dysfunction. *Nat. Rev. Neurosci.* **9**, 826–838 (2008).
8. Vembar, S. S. & Brodsky, J. L. One step at a time: endoplasmic reticulum-associated degradation. *Nat. Rev. Mol. Cell Biol.* **9**, 944–957 (2008).
9. Hartl, F. U., Bracher, A. & Hayer-Hartl, M. Molecular chaperones in protein folding and proteostasis. *Nature* **475**, 324–332 (2011).
10. Baneyx, F. & Mujacic, M. Recombinant protein folding and misfolding in Escherichia coli. *Nat. Biotechnol.* **22**, 1399–1408 (2004).
11. Åkerfelt, M., Morimoto, R. I. & Sistonen, L. Heat shock factors: Integrators of cell stress, development and lifespan. *Nat. Rev. Mol. Cell Biol.* **11** 545–555 (2010).
12. Balch, W. E., Morimoto, R. I., Dillin, A. & Kelly, J. W. Adapting proteostasis for disease intervention. *Science* **319** 916–919 (2008).
13. Dai, C., Whitesell, L., Rogers, A. B. & Lindquist, S. Heat Shock Factor 1 Is a Powerful Multifaceted Modifier of Carcinogenesis. *Cell* **130**, 1005–1018 (2007).
14. Mendillo, M. L. *et al.* HSF1 drives a transcriptional program distinct from heat shock to support highly malignant human cancers. *Cell* **150**, 549–562 (2012).
15. Santagata, S. *et al.* Tight coordination of protein translation and HSF1 activation supports the anabolic malignant state. *Science* **341**, 1238303 (2013).
16. Neef, D. W., Jaeger, A. M. & Thiele, D. J. Heat shock transcription factor 1 as a therapeutic target in neurodegenerative diseases. *Nat. Rev. Drug Discov.* **10** 930–944 (2011).
17. Saio, T., Guan, X., Rossi, P., Economou, A. & Kalodimos, C. G. Structural basis for protein antiaggregation activity of the trigger factor chaperone. *Science* **344**, 1250494 (2014).
18. Huang, C., Rossi, P., Saio, T. & Kalodimos, C. G. Structural basis for the antifolding activity of a molecular chaperone. *Nature* **537**, 202–206 (2016).
19. Jiang, Y., Rossi, P. & Kalodimos, C. G. Structural basis for client recognition and activity of Hsp40 chaperones. *Science* **365**, 1313–1319 (2019).
20. Ferbitz, L. *et al.* Trigger factor in complex with the ribosome forms a molecular cradle for nascent proteins. *Nature* **431**, 590–6 (2004).
21. Hoffmann, A., Bukau, B. & Kramer, G. Structure and function of the molecular chaperone Trigger Factor. *Biochim. Biophys. Acta.* **1803**, 650–61 (2010).
22. Jakob, R. P. *et al.* Dimeric Structure of the Bacterial Extracellular Foldase PrsA. *J. Biol. Chem.* **290**, 3278–3292 (2015).
23. Xu, X., Wang, S., Hu, Y. X. & McKay, D. B. The Periplasmic Bacterial Molecular Chaperone SurA Adapts its Structure to Bind Peptides in Different Conformations to Assert a Sequence Preference for Aromatic Residues. *J. Mol. Biol.* **373**, 367–381 (2007).
24. Oroz, J. *et al.* Structure and pro-toxic mechanism of the human Hsp90/PPIase/Tau

complex. *Nat. Commun.* **9**, 1–13 (2018).
25. Guo, Y. *et al.* Evidence for a Mechanism of Repression of Heat Shock Factor 1 Transcriptional Activity by a Multichaperone Complex. *J. Biol. Chem.* **276**, 45791–45799 (2001).
26. Lee, K. *et al.* The structure of an Hsp90-immunophilin complex reveals cochaperone recognition of the client maturation state. *Mol. Cell* **81**, 3496-3508.e5 (2021).
27. Anckar, J. & Sistonen, L. Regulation of HSF1 Function in the Heat Stress Response: Implications in Aging and Disease. *Annu. Rev. Biochem.* **80**, 1089–1115 (2011).
28. Sarge, K. D., Murphy, S. P. & Morimoto, R. I. Activation of heat shock gene transcription by heat shock factor 1 involves oligomerization, acquisition of DNA-binding activity, and nuclear localization and can occur in the absence of stress. *Mol. Cell. Biol.* **13**, 1392–1407 (1993).
29. Zuo, J., Baler, R., Dahl, G. & Voellmy, R. Activation of the DNA-binding ability of human heat shock transcription factor 1 may involve the transition from an intramolecular to an intermolecular triple-stranded coiled-coil structure. *Mol. Cell Biol.* **14**, 7557–7568 (1994).
30. Westwoodt, J. T. & Wu, C. Activation of Drosophila heat shock factor: conformational change associated with a monomer-to-trimer transition. *Mol. Cell Biol.* **13**, 3481–3486 (1993).
31. Zhang, H. *et al.* Reversible phase separation of HSF1 is required for an acute transcriptional response during heat shock. *Nat. Cell Biol.* **24**, 340–352 (2022).
32. Banani, S. F., Lee, H. O., Hyman, A. A. & Rosen, M. K. Biomolecular condensates: Organizers of cellular biochemistry. *Nat. Rev. Mol. Cell Biol.* **18** 285–298 (2017).
33. Yoshizawa, T., Nozawa, R. S., Jia, T. Z., Saio, T. & Mori, E. Biological phase separation: cell biology meets biophysics. *Biophys. Rev.* **12** 519–539 (2020).
34. Jolly, C. *et al.* In vivo binding of active heat shock transcription factor 1 to human chromosome 9 heterochromatin during stress. *J. Cell Biol.* **156**, 775–781 (2002).
35. Biamonti, G. & Vourc'h, C. Nuclear Stress Bodies. *Cold Spring Harb. Perspect. Biol.* **2**, a000695 (2010).
36. Biamonti, G. Nuclear stress bodies: A heterochromatin affair? *Nat. Rev. Mol. Cell Biol.* **5** 493–498 (2004).
37. Ninomiya, K. *et al.* LncRNA-dependent nuclear stress bodies promote intron retention through SR protein phosphorylation. *EMBO J.* **39**, e102729 (2020).
38. Ninomiya, K. *et al.* m6A modification of HSATIII lncRNAs regulates temperature-dependent splicing. *EMBO J.* **40**, e107976 (2021).
39. Goenka, A. *et al.* Human satellite-III non-coding RNAs modulate heat-shock-induced transcriptional repression. *J. Cell Sci.* **129**, 3541–3552 (2016).
40. Jolly, C., Usson, Y. & Morimoto, R. I. Rapid and reversible relocalization of heat shock factor 1 within seconds to nuclear stress granules. *Proc. Natl. Acad. Sci. U S A* **96**, 6769–6774 (1999).
41. Mähl, P., Lutz, Y., Puvion, E. & Fuchs, J.-P. Rapid Effect of Heat Shock on Two Heterogeneous Nuclear Ribonucleoprotein-associated Antigens in HeLa Cells. *J. Cell. Biol.* **109**, 1921–35 (1989).
42. Gaglia, G. *et al.* HSF1 phase transition mediates stress adaptation and cell fate decisions. *Nat. Cell Biol.* **22** 151–158 (2020).
43. Xanthoudakis, S. & Nicholson, D. W. Heat-shock proteins as death determinants. *Nat. Cell Biol.* **2**, e163–e165 (2000).
44. Jumper, J. *et al.* Highly accurate protein structure prediction with AlphaFold. *Nature* **596**, 583–589 (2021).
45. Weitzel, G., Pilatus, U. & Rensing, L. Similar dose response of heat shock protein synthesis and intracellular pH change in yeast. *Exp. Cell Res.* **159**, 252–256 (1985).
46. Díaz, F. E. *et al.* Fever-range hyperthermia improves the anti-apoptotic effect induced by

low pH on human neutrophils promoting a proangiogenic profile. *Cell Death & Disease* **7**, e2437–e2437 (2016).

47. Triandafillou, C. G., Katanski, C. D., Dinner, A. R. & Allan Drummond, D. Transient intracellular acidification regulates the core transcriptional heat shock response. *Elife* **9**, 1–30 (2020).

CHAPTER II

Structural Insight into Proline *cis/trans* Isomerization of Unfolded Proteins Catalyzed by Trigger Factor Chaperone

Abstract

Molecular chaperones, which act as foldase, often possess peptidyl-prolyl *cis/trans* isomerase (PPIase) domain (PPD). PPIase catalyzes the proline cis/trans isomerization that often be the rate-limiting step for protein folding. A bacterial chaperone Trigger Factor (TF), which has PPD, acts as a highly efficient catalyst in the folding process limited by peptidyl-prolyl isomerization. In this chapter, to elucidate the mechanism of PPIase, which plays a major role in foldase activity, I investigated the mechanism through which TF recognizes the proline residue in the unfolded client protein during the *cis/trans* isomerization process. The solution structure of TF in complex with the client protein showed that TF recognizes the proline-aromatic motif located in the hydrophobic stretch of the unfolded client protein through its conserved hydrophobic cleft. Molecular dynamics simulation revealed that TF exploits the backbone amide group of I195 to form an intermolecular hydrogen bond with the carbonyl oxygen of the amino acid residue preceding the proline residue at the transition state, which presumably stabilizes the transition state and thus accelerates the isomerization. The importance of such intermolecular hydrogen bond formation during the catalysis was further corroborated by the activity assay and NMR relaxation analysis. In conclusion, TF^{PPD} catalyzes the proline *cis/trans* isomerization by the formation of intramolecular hydrogen bond through I195, and it is suggested that Foldase such as TF chaperone preferentially accelerates the isomerization of the peptidyl-prolyl bond that is eventually folded into the core of the protein in its native fold.

2.1. Introduction

As described in General Introductions, the folding assistance by chaperone is one of the important reactions in the Hsf1-chaperone system. Here, I focused on the catalytic function of proline *cis/trans* isomerization (PPIase) to elucidate the foldase mechanism of molecular chaperone. The transition between *cis* and *trans* forms of peptidyl-prolyl bond, in which the ω dihedral angle is approximately 0° or 180°, respectively, occurs very slowly in the absence of PPIases owing to the high energy barrier imposed by the partial double bond character of the peptide bond. Even though the *trans* form is usually more populated than *cis* form in the unfolded proteins, the protein folding may require either of the two forms to fit in the native fold. Thus, several chaperones have PPIase domain for assisting substrate protein folding.

I used a bacterial chaperone Trigger Factor (TF) as model PPIase to investigate the PPIase mechanism. TF has an FK506 binding protein (FKBP)-type PPIase domain (PPD) along with the other two domains, the ribosome-binding domain (RBD) and the substrate-binding domain (SBD)[1]. TF acts as a highly efficient catalyst in the folding process limited by peptidyl-prolyl isomerization[2,3]. It is suggested that the PPD plays a key role in the foldase activity of TF, but the mechanism through which TF^{PPD} catalyzes the peptidyl-prolyl *cis/trans* isomerization, as well as the mechanism for the other members of the FKBP-type PPIase family, still remain unclear. The lack of a comprehensive structural study that can track the entire *cis/trans* isomerization process has hindered the elucidation of the mechanism. Further insight into the structure of the PPIase in complex with the client protein both at the ground state and at the transition state is required.

In this chapter, I conducted an integrated study on TF^{PPD} exploiting solution NMR, molecular dynamics (MD) simulation, and activity assay to elucidate the mechanism of PPIase. The solution structure of TF^{PPD} in complex with a proline-containing fragment of maltose-binding protein (MBP), has unveiled the mechanism by which the proline residue

is recognized by TF^{PPD}, and MD simulation has shed light on the complex at the transition state. These results show that the conserved hydrophobic cleft of TF^{PPD} recognizes the *trans* form of the proline-aromatic motif in the client protein and that an intermolecular hydrogen bond between the backbone amide group of I195 in TF^{PPD} and the carbonyl oxygen of the amino acid residue preceding the proline residue in MBP is formed at the transition state. These results suggest that the hydrophobic environment around the peptidyl-prolyl bond and the intermolecular hydrogen bond at the transition state play major roles in the proline *cis/trans* isomerization.

2.2. Materials and Methods

Expression and purification of protein samples

TF from *E. coli* was cloned into the pCold vector (Takara Bio). The following TF expression constructs were prepared: TF^{SBD} (residues 113–432Δ150–246) was cloned into pET16b vector (Novagen) and fused to His_6-MBP and a tobacco etch virus (TEV) protease cleavage site at the N-terminus. TF^{PPD} (residues 148 to 249) and $TF^{PPD\text{-}SBD}$ (residues 113 to 246) were cloned into pCold vector (Takara Bio) and fused to His_6-tag. TF mutants were constructed by site-directed mutagenesis using PrimeSTAR Mutagenesis Basal Kit (Takara Bio). The constructs of TF^{PPD}, $TF^{PPD\text{-}SBD}$, and TF having mutations of R193P, M194P, M194A, I195P, I195L, or H222A, were prepared. A fusion protein MBP238-266-$(GS)^5$-TF^{PPD} was cloned into pET-16b vector containing a His_6-MBP and a TEV protease cleavage site at the N terminus. The length of the GS linker was designed from the following consideration. The crystal structure of TF (PDB ID: 1w26) shows that the N-terminus of TF^{PPD} is located ~25 Å away from the substrate-binding site. More specifically, the distance between Cα atoms of Q148 (N-terminus of TF^{PPD}) and I195, which is located at the center of the expected binding site, is 26 Å. Given the fact that the length of the fully extended 10 amino acid polypeptide chain is estimated as 35 Å, the five repeats of Gly-Ser should provide sufficient length to preserve the interaction between the two isolated proteins.

All of the expression constructs were transformed into BL21(DE3) cells. The following MBP fragments were prepared in this study: MBP29-99, MBP97-164, MBP160–201, MBP198–265, MBP260-336, MBP331-396. The MBP fragments were cloned into the pET-16b vector containing a His_6-MBP and a TEV protease cleavage site at the N terminus. For the unlabeled samples, cells were grown in Luria-Bertani (LB) medium at 37°C in the presence of ampicillin (100 μg ml^{-1}). Protein expression was induced by the addition of 0.2 to 0.5 mM isopropyl-β-D-1-thiogalactopyranoside (IPTG) at OD_{600} ~0.6, followed by 12 to 16 hours of incubation at 18°C. Cells were harvested at

OD_{600} ~2.0 and resuspended in lysis buffer containing 50 mM tris-HCl (pH 8.0), 500 mM NaCl. Isotopically labeled samples for NMR studies were prepared by growing the cells in minimal (M9) medium. Cells were harvested at OD_{600} ~1.0. U-[^{13}C,^{15}N]–labeled samples were prepared by supplementing the medium with $^{15}NH_4Cl$ (1 g L^{-1}) and $^{13}C_6$-glucose (2 g L^{-1}). Cells were disrupted by sonicator and centrifuged at 18,000 rpm for 45 min. Proteins were purified using Ni Sepharose 6 Fast Flow resin (GE Healthcare), followed by tag removal by TEV protease at 4°C (incubation for 16 hours) and gel filtration using Superdex 75 16/60 (GE Healthcare). Protein concentration was determined spectrophotometrically at 280 nm using the corresponding extinction coefficient.

NMR spectroscopy

NMR samples are prepared in 20 mM KPi (pH 7.0), 100 mM KCl, 4 mM βME, 0.5 mM EDTA, 0.05% NaN_3, and 7% D_2O. Protein concentration was 0.1 to 0.8 mM. NMR experiments were performed on Agilent UNITY Inova 800 and 600 MHz NMR spectrometers as well as Bruker Avance III 800 and 600 MHz NMR spectrometers. The experiments were performed at 10°C for isolated MBP fragments, and at 22°C for the other samples. Spectra were processed using the NMRPipe program[4], and data analysis was performed with Olivia (fermi.pharm.hokudai.ac.jp/olivia). The chemical shift changes of the amide moiety were normalized according to the following equation.

$$\Delta\delta = \sqrt{\left(\Delta\delta\left(^{1}\mathrm{H}\right)\right)^{2} + \left(\Delta\delta\left(^{15}\mathrm{N}\right)/5\right)^{2}} \qquad (2-1)$$

Structure determination

In order to increase the population of the bound state and thus to obtain sufficient number of intermolecular NOEs for high resolution structure determination, a fusion protein[5], in which the peptide containing the binding site (MBP238-266) was fused to the N-terminus of TF^{PPD} with a linker consisting of 5 repeat units of Gly-Ser, was constructed and used in the NOE observation. 2D and 3D NMR experiments were carried out using

Agilent UNITY Inova 800 and 600 MHz NMR spectrometers for the NMR sample containing 1.0 mM $^{13}C/^{15}N$-labeled MBP238-266-$(GS)^5$-TF^{PPD} in 20 mM KPi (pH 7.0), 100 mM KCl, 4 mM 2-mercaptoethanol, 0.5 mM EDTA, 0.05% NaN_3, and 7% D_2O. The ^1H, ^{13}C and ^{15}N resonance assignments were carried out using the following set of the spectra measured at 22 °C, ^1H-^{15}N HSQC, ^1H-^{13}C HSQC, HNCO, HNCA, HN(CO)CA, HNCACB, CBCA(CO)NH, HNCAHA, HBHACONH, CCH-TOCSY, HC(C)H-TOCSY, HBCBCGCDHD and HBCBCGCDCEHE. The ^1H, ^{13}C, ^{15}N chemical shifts were referred to DSS according to the IUPAC recommendation. Inter-proton distance restraints for structural calculations were obtained from ^{13}C-edited NOESY-HSQC and ^{15}N-edited NOESY-HSQC spectra with a 150 ms mixing time at 22 °C.

The structure was calculated using the CYANA software package[6], on the basis of the inter-proton distance restraints from the NOESY spectra. The NOE restraints were further corroborated by the dihedral angle restraints from the TALOS+ program[7] and hydrogen bond restraints for the regions forming secondary structures. One hundred structures were calculated individually using 10,000 steps of simulated annealing, and a final ensemble of 20 structures was selected based on CYANA target function values. The 20 lowest-energy structures resulted from CYANA calculation were refined by restrained molecular dynamics in explicit water with CNS[8]. The atomic coordinates and structural restraints of MBP238-266-$(GS)^5$-TF^{PPD} have been deposited in the Protein Data Bank (PDB ID: 5ZR0).

^{15}N relaxation dispersion experiment

An ^{15}N-Carr-Purcell-Meiboom-Gill (CPMG) pulse sequence[9] was used to examine the chemical exchange derived from *cis/trans* isomerization of P255 in MBP238-266-$(GS)^5$-TF^{PPD} or MBP238-266-$(GS)^5$-$TF^{PPD,\ I195P}$. Two-dimensional data sets were acquired as 240 × 2048 complex points in the t1 × t2 time-domain dimensions with a constant relaxation delay of 50 ms. The experiments were performed on Bruker

Avance III 800 MHz NMR spectrometers at 35°C. The exchange rate constant for the two conformers, kex, was extracted using NESSY[10] with the Meiboom equation[11] as below,

$$R_2^{eff} = R_2^0 + \frac{\Phi}{k_{ex}}\left[1 - \frac{4\nu_{CPMG}}{k_{ex}} tanh\left(\frac{k_{ex}}{4\nu_{CPMG}}\right)\right] \quad (2-2)$$

$$\phi = p_a * p_b * \delta\omega^2 \quad (2-3)$$

which was applied to the fast exchange processes between the two states, where R_2^{eff} is the effective transverse relaxation rate, R_2^0 is the effective transverse relaxation rate at infinite ν_{CPMG}, p_a and p_b are the populations of the two state models ($p_a + p_b = 1$), k_{ex} is the chemical/conformational exchange ($k_{ex} = k_{a\text{-}b} + k_{b\text{-}a}$) constant and δ_ω is the chemical shift difference between states. With this equation, only R_2^0, kex and Φ can be extracted, as p_a, p_b, and δ_ω cannot be uniquely determined. Note that the fast exchange regime was judged on the basis of the comparison between the expected δ_ω and the observed k_{ex}. For example, the ^{1}H-^{15}N HSQC spectrum for ^{15}N MBP 198-265 shows the two sets of the resonance for Gly254, corresponding to the *trans* and *cis* conformations of Pro255 (Figure 2.9C). The ^{15}N chemical shift difference between the two resonances, ~0.8 ppm and thus ~61 Hz on 800 MHz NMR instrument, which corresponds to δ_ω in the relaxation dispersion experiment, is much smaller than the kex value (740 s^{-1}).

Molecular dynamics simulations

The molecular simulations were carried out using the AMBER14 molecular dynamics package and the ff14SB force field parameters. The initial structure for the simulations was prepared from the NMR structure. The simulation systems were solvated in a cubic periodic box with TIP3P water molecules. The systems were subjected to 5,000 steps of energy minimization, and were equilibrated for 3 ns in an isothermal-isovolumetric (NVT) condition with the solute atoms constrained with the force constant of 1 kcal/mol·Å^{-2}. Several initial structures were obtained during the constrained MD runs. After the equilibration, the production simulations with constrained were carried out in an isothermal-isobarometric (NPT) condition at 1 atm and 300 K. Simulations were

performed using a 2 fs time step, periodic boundary conditions, particle mesh Ewald electrostatics, and constraints of hydrogen-containing bonds using the SHAKE algorithm[12]. The position restraints with the force constants of 50 kcal/mol·rad^2 was applied to the dihedral angle varying the center of the angle every 0.2° from initial angle (-174°) to 0° with clockwise and counterclockwise, respectively. For each position, the simulations were carried out for 2 ps, resulting in 1.74 ns and 1.86 ns trajectories for clockwise and counterclockwise rotations, respectively. Although the peptidyl-prolyl *cis/trans* isomerization is a slow process that occurs in millisecond timescale, this slow process is due to the low probability of the transition and a single transition only takes a few nanoseconds that corresponds to the trajectories in this simulation.

ITC experiment

Calorimetric titrations were carried out on an iTC200 microcalorimeter (GE Healthcare) at 22°C. All protein samples were purified in ITC buffer containing 20 mM potassium phosphate (pH 7.0), 100 mM KCl, and 0.05% NaN_3 by gel filtration. The 200 μL sample cell was filled with 350 μM MBP198-265, and the 40 μL injection syringe was filled with 3.5 mM solution of $TF^{PPD\text{-}SBD}$. The titrations were carried out with a preliminary 0.2 μL injection, followed by 9 injections of 4.2 μL each with time intervals of 5 min. The solution was stirred at 1000 rpm. Data for the preliminary injection, which are affected by diffusion of the solution from and into the injection syringe during the initial equilibration period, were discarded. Binding isotherms were generated by plotting heats of reaction normalized by the modes of injectant versus the ratio of total injectant to total protein per injection. The data were fitted with Origin 7.0 (OriginLab Corporation).

RNase T1 refolding assay

RNase T1 from Aspergillus oryzae (Sigma, R-1003) was denatured, reduced, and carboxymethylated using dithiothreitol as the reducing agent according to the previous

report[13]. Refolding of reduced and carboxymethylated RNase T1 (RCM-RNase T1) in 0.1 M Tris-HCl (pH 8.0), 0.4 M NaCl was initiated by 4-fold rapid dilution into the buffer containing 0.1 M Tris-HCl (pH 8.0), 2.0 M NaCl. The final concentration of RCM-RNase T1 was 1 μM. The refolding process of RCM-RNase T1 in the absence and presence of TF or its variants at the concentration of 0.2 μM was monitored by an increase in tryptophan fluorescence intensity. Fluorescence intensity was measured using a spectrofluorometer (FP-8500, JASCO Corporation). The excitation and emission wavelengths were set at 268 nm (band width 5 nm) and 320 nm (band width 10 nm), respectively. All measurements were performed at 15°C.

2.3. Results

2.3.1 TF^{PPD} Recognizes Proline Residue in the Hydrophobic Region

Interaction between TF (Figure 2.1A) and an unfolded substrate protein was first investigated by NMR. MBP was used as an unfolded substrate protein. To ensure the solubility and stability in the unfolded state, MBP was divided into short fragments and six fragments of MBP[14], MBP29-99, MBP97-164, MBP160-201, MBP198-265, MBP260-336, and MBP331-396 were prepared. All of the MBP fragments exhibited narrow chemical shift dispersion in the $^{1}H^{15}N$-HSQC spectra, which is characteristic to unfolded proteins (Figure 2.1B). MBP consists of 396 amino acids and contains 21 proline residues. To identify the interaction sites on the unfolded MBP, the tandem domain $TF^{PPD-SBD}$, which possesses all of the five substrate-binding sites[15], was titrated into isotopically labeled MBP fragments and the perturbation of each resonance from the MBP fragments was monitored (Figure 2.1B). The addition of $TF^{PPD-SBD}$ induced a significant reduction in the intensity of the resonances due to the size of the protein and the binding kinetics. Differential line broadening analysis showed that a total of 12 regions of MBP are recognized by TF (Figure 2.2A, 2.3A). The continuous stretch consisting of more than four amino acid residues with significant intensity reduction upon the addition of $TF^{PPD-SBD}$ was defined as a binding site. These TF-recognition sites contain highly hydrophobic regions (Figure 2.2A) and are located on the core of MBP in its native fold (Figure 2.3B). The regions recognized by TF are enriched with hydrophobic amino acids including aromatic residues, such as tryptophan and phenylalanine, as well as bulky hydrophobic aliphatic amino acids such as leucine and valine (Figure 2.3C, D). This binding preference of TF toward hydrophobic and aromatic amino acid residues is consistent with the results obtained in the previous studies that used other unfolded protein substrates[15,16]. Thermodynamics parameters of the interaction between $TF^{PPD-SBD}$ and MBP198-265 estimated by isothermal titration calorimetry (ITC) experiment (Figure 4), ΔG -5.8 ± 0.1 kcal/mol, ΔH -5.9 ± 0.4 kcal/mol, and $-T\Delta S$ -0.1 ± 0.5 kcal/mol, indicated that the binding

is enthalpy-driven. The dissociation constant K_d was calculated as 47 ± 9 μM, indicating the binding between TF and MBP is relatively weak. Among the 21 proline residues in the MBP sequence, four residues are located in the hydrophobic regions and are recognized by TF (Figure 2.3A, D). The proline residues in the hydrophilic regions did not interact with TF, which is in accord with the previous report showing that TF has no specificity toward proline residue[16].

To further investigate the recognition of the proline-containing hydrophobic stretches of MBP by TF, the two fragments of MBP containing proline residues in the hydrophobic stretches, MBP160-201 and MBP198-265, were subjected to titration experiments with isolated domains of TF, TF^{PPD} and TF^{SBD}. Both domains were titrated into isotopically labeled MBP160-201 and MBP198-265, and the interaction was monitored by NMR (Figure 2.5A). Several resonances on the HSQC spectra were specifically affected by the addition of TF^{PPD} or TF^{SBD}. A significant line broadening, with a consequent intensity reduction, was observed by the addition of TF^{SBD}, whereas both line broadening and chemical shift perturbation were observed upon the addition of TF^{PPD} (Figure 2.5A), reflecting the difference between the domains with regard to binding kinetics and molecular weight. For clarity, intensity changes were evaluated and compared in the analysis. As seen in the titration of $TF^{PPD-SBD}$, the addition of TF^{SBD} and TF^{PPD} induced a significant intensity reduction for specific resonances of the MBP160-201 and MBP198-265 (Figure 2.2B, 2.5A). These resonances are from the following MBP regions: F175-I187, Y193-Y197, L218-N227, A239-K245, and T251-S259. All of these five binding sites are affected by the addition of isolated domains of TF^{PPD} and TF^{SBD}. However, the extent of peak intensity change varies among the binding sites: In the titration experiments for isotopically labeled MBP198-265, the most significant peak intensity reductions were observed for the resonances attributed to the MBP stretch T251-S259 upon the addition of TF^{PPD}, whereas the addition of TF^{SBD} caused the most significant effects on the resonances from the MBP stretch L218-N227 (Figure 2.2B).

Given the relatively weak affinity between the MBP fragment and TF as expected from ITC data (Figure 2.4) and the fact that the peak intensity change was monitored by the addition of a substoichimetric amount of TF proteins, more significant intensity reduction, thus more significant line broadening, is attributed to slower binding kinetics, which tends to occur in stronger interaction[17], and/or higher population of the bound form. In either case, the extent of the peak broadening can be interpreted as an indication of the binding preference. Thus, the data suggests that the MBP stretches L218-N227 and T251-S259 are preferred by TF^{SBD} and TF^{PPD}, respectively. Note that the plots of chemical shift change by the addition of TF^{PPD} showed the same trend (Figure 2.5B), further supporting the preference of TF^{PPD}. Interestingly, the hydrophobic stretch of T251-S259 contains two tryptophan residues and one proline residue, whereas the other two stretches in MBP198-265 are devoid of the pair of tryptophan and proline residues. This result suggests that TF^{PPD} possesses a preference toward aromatic and proline residues located in the hydrophobic regions.

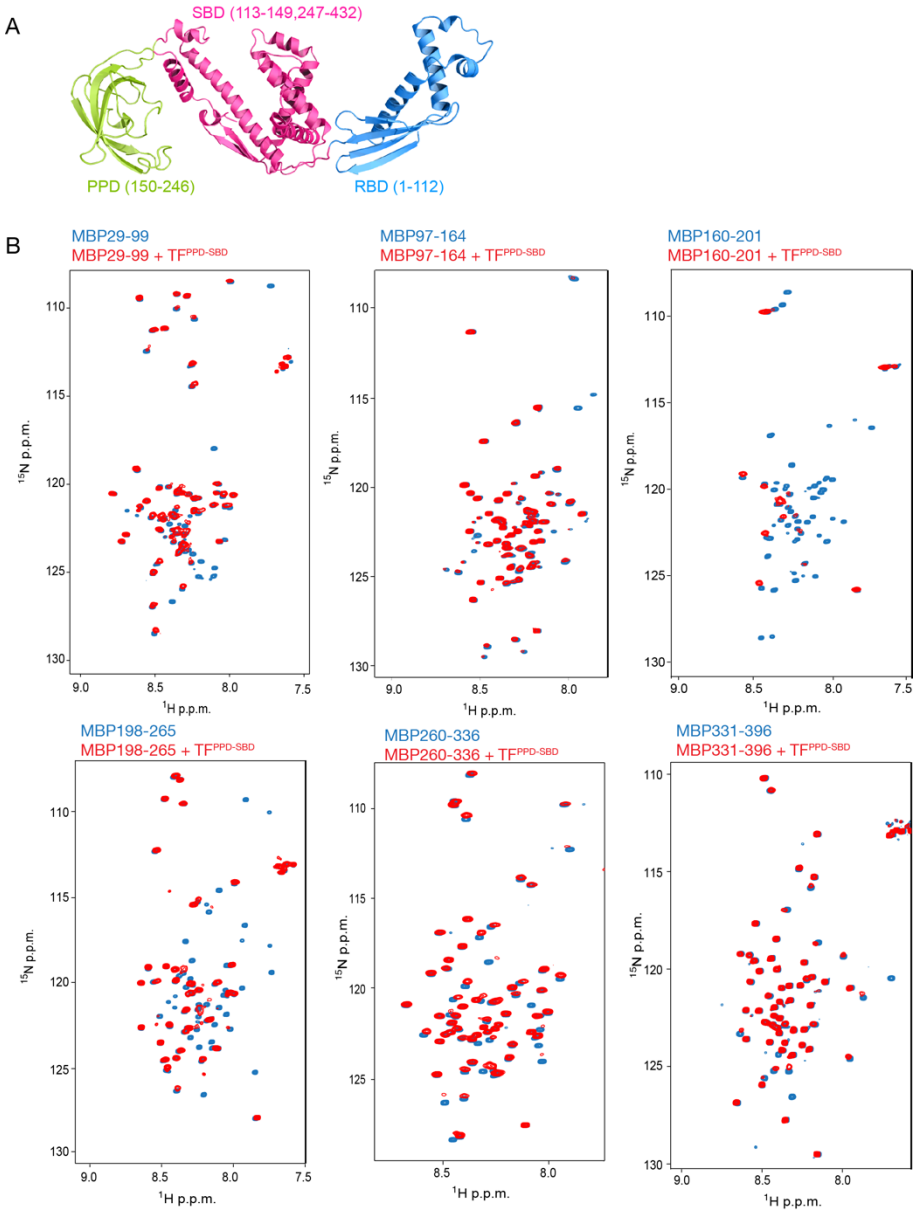

Figure 2.1 Identification of TF-binding sites in MBP by NMR
(A) Structure of *E. coli* TF (PDB ID: 1W26). PPD, SBD, and RBD are shown in green, pink, and blue, respectively. The residue boundaries for each one of the three domains are shown in parentheses. SBD is discontinuous and is formed primarily by the C-terminal domain. (B) ^{1}H-^{15}N HSQC spectra of MBP fragments in the absence (blue) and presence (red) of TF$^{PPD-SBD}$, having all of the five substrate-binding sites of TF. The fragments of MBP cover the entire region of MBP except the signal sequence. The spectra were recorded for several titration points, MBP:TF 1:0.1, 1:0.2, 1:0.3, 1:0.5, 1:0.7, 1:1, and 1:2, but only the spectra for the ratio of 1:1 were shown here. Concentration of the isotopically labeled MBP fragment was 0.2 mM. The addition of TF$^{PPD-SBD}$ induced significant intensity reduction.

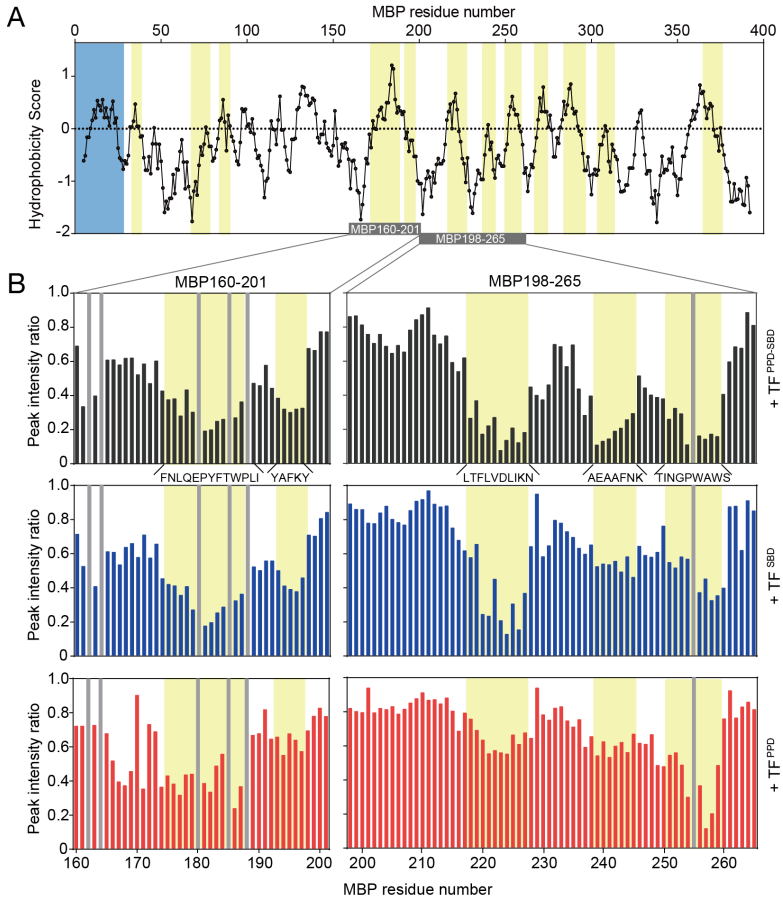

Figure 2.2 Recognition of unfolded MBP by TF.

(A) Plot of the hydrophobicity score (Roseman algorithm, window = 9) of MBP as a function of its primary sequence. A hydrophobicity score higher than zero denotes increased hydrophobicity. The regions recognized by TF as identified by NMR titration experiments are highlighted in yellow. The signal sequence is highlighted in blue. The MBP segments depicted in the panel B are indicated as a gray bar. (B) Plots of peak intensity change of MBP160-201 (left panels) and MBP198-265 (right panels) by the addition of $TF^{PPD-SBD}$ at a ratio of MBP:$TF^{PPD-SBD}$ 1:0.1 (top panels), TF^{SBD} at a ratio of MBP:TF^{SBD} 1:0.2 (middle panels), and TF^{PPD} at a ratio of MBP:TF^{PPD} 1:0.5 (bottom panels), as a function of the primary sequences of the MBP peptides. The regions recognized by TF are highlighted in yellow and labeled with the primary sequences. The proline residue and unassigned residue are indicated by gray bar.

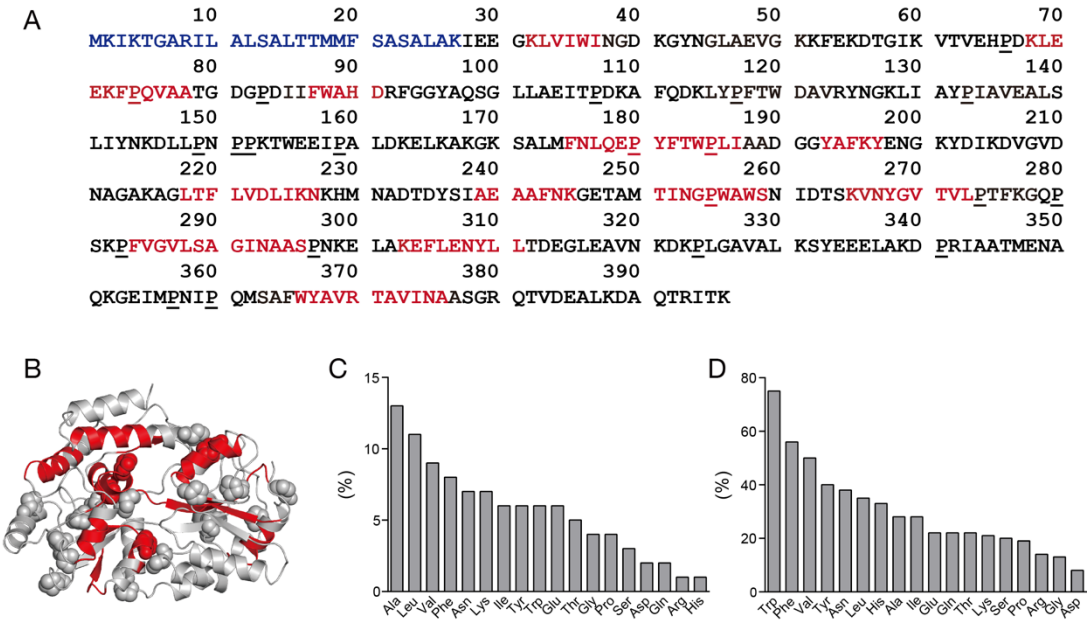

Figure 2.3 Amino acid composition of TF-binding sites in MBP
(A) Primary sequence of MBP with the TF-binding sites colored red. The signal sequence is colored blue. Proline residues are indicated by underlines. (B) Structure of MBP (PDB ID: 1ANF) with proline residues represented as sphere model. The regions recognized by TF as determined by NMR titration experiments are colored red. (C) Percentage values of the MBP amino acids that interact with TF. (D) Percentage values of the MBP amino acids that interact with TF normalized against the total number of each one of amino acids in the MBP sequence.

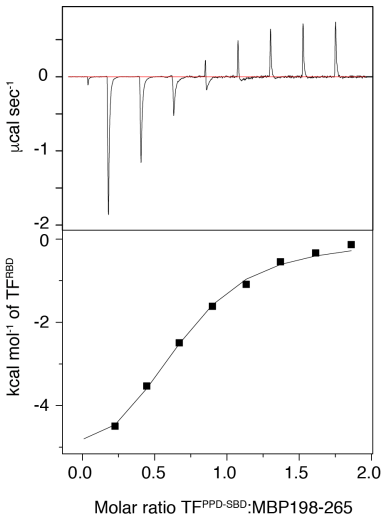

Figure 2.4 Thermodynamic characterization of the interaction between TF and MBP
ITC traces of the titration of $TF^{PPD\text{-}SBD}$ to MBP198-265 performed at 22 °C, showing that $TF^{PPD\text{-}SBD}$ binds to MBP198-265 with K_d of 47 ± 9 µM and formation of the complex is enthalpy driven.

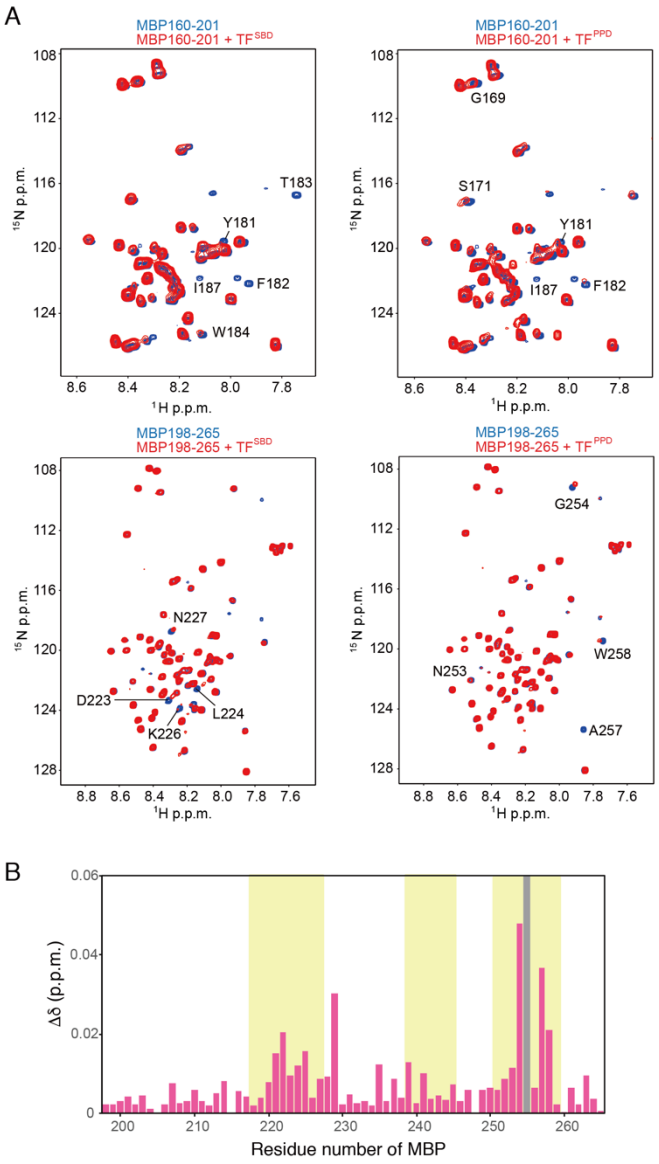

Figure 2.5 Investigation of the interaction between MBP and TF^{SBD} or TF^{PPD} by NMR
(A) ^{15}N labeled MBP160-201 and MBP198-265 were titrated with unlabeled TF^{SBD} or TF^{PPD}. The ^{1}H-^{15}N HSQC spectra of MBP160-201 and MBP198-265 are shown in the absence (blue) and presence (red) of TF^{SBD} or TF^{PPD}. The spectra were recorded for several titration points, MBP:TF 1:0.1, 1:0.2, 1:0.3, 1:0.5, 1:0.7, 1:1, and 1:2, but only the spectra for the ratio of MBP:TF^{SBD} 1:0.2 and MBP:TF^{PPD} 1:0.5 were shown here. Concentration of the isotopically labeled MBP fragment was 0.2 mM. (B) Plots of chemical shift change of MBP198-265 by the addition of TF^{PPD} at a ratio of MBP:TF^{PPD} 1:0.5. The proline residue, P255, showing no backbone amide resonance on the spectra is indicated by gray bar.

To identify the interaction site on TF^{PPD}, I further investigated the interaction by NMR titration experiments observing the resonances from TF^{PPD}. MBP160-201 or MBP198-265 was titrated into isotopically labeled TF^{PPD} (Figure 6A). Addition of the

MBP fragment induced significant chemical shift perturbations for the resonances of TF^{PPD} (Figure 6B, C). The chemical shift perturbation mapping shows that majority of the perturbed resonances are from the conserved hydrophobic surface of TF^{PPD} (Figure 6B-E). These chemical shift changes are in the fast exchange regime (Figure 6A), which indicates a highly dynamic binding mode between TF^{PPD} and unfolded MBP, and Relatively small chemical shift perturbations indicate the moderate affinity between the isolated TF^{PPD} and MBP.

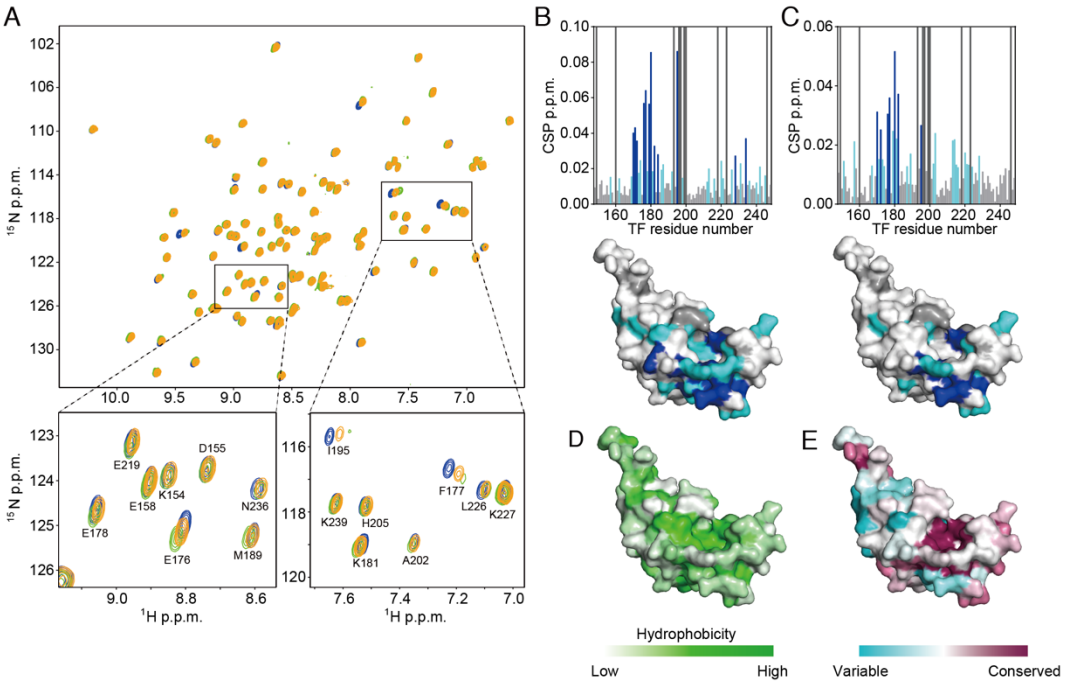

Figure 2.6 The substrate-binding sites on TF^{PPD}
(A) ^{1}H-^{15}N HSQC spectra of TF^{PPD} in the absence (blue) and presence of MBP160-201 (orange) or MBP198-265 (green). The spectra were recorded with several titration points, TF^{PPD}:MBP 1:0.1, 1:0.2, 1:0.5, 1:1, and 1:2, but only the spectra at 1:1 ratio are shown for clarity. The regions indicated by a box in the top panel are expanded in the bottom panels with resonance assignments. Chemical shift perturbations of amide moieties of TF^{PPD} upon binding to MBP160-201 (B) or MBP198-265 (C), plotted as a function of the residue number of TF^{PPD}. Proline and unassigned residues are indicated by a bar colored dark gray. Lower panels show chemical shift perturbation mapping on the structure of TF^{PPD} (PDB ID: 1W26). The residues with perturbations larger than the threshold values of 0.015 and 0.025 ppm are colored light blue and dark blue, respectively. Proline and unassigned residues are colored dark gray. (D) Mapping of the hydrophobicity on the structure of TF^{PPD}. (E) TF^{PPD} sequence conservation mapped on the structure of TF^{PPD}.

2.3.2 Structural Basis for the Recognition of Proline Residue in the Substrate Protein

To gain a better insight into the recognition of the MBP stretch containing proline and aromatic residues by TF^{PPD}, I conducted a structural analysis of TF^{PPD} in complex with unfolded MBP, focusing on the MBP stretch T251-S259 that contains both proline and aromatic residues. Since the relatively low affinity between TF^{PPD} and MBP results in a low population of the complex when the two proteins are mixed in solution, a fusion protein was designed to increase the population of the bound state, which would increase the number of intermolecular NOEs for high-resolution structure determination. To this aim, the peptide containing the binding site (MBP238-266) was fused to the N-terminus of TF^{PPD} with a linker consisting of five repeat units of Gly-Ser. The directions of the chemical shift perturbations caused by the fusion of the MBP peptide coincided with those resulting from the addition of the isolated MBP fragment (Figure 2.7), indicating that the interaction between TF^{PPD} and MBP238-266 is preserved in the fusion protein. Moreover, much more significant chemical shift perturbations were observed for the fusion protein, which indicates that a much higher population of the MBP peptide is bound to TF^{PPD} in the fusion. The solution structure of MBP- TF^{PPD} complex was determined on the basis of 1205 NOE-derived inter-proton distance restraints, 128 dihedral angle restraints, and 20 hydrogen bond restraints (Table 2.1). A total of 100 structures were calculated, among which the 20 lowest energy structures were selected (Figure 2.8A).

The structure showed that TF^{PPD} recognizes the hydrophobic stretch of MBP, P255-W258, using the broad hydrophobic surface (Figure 2.8B) that is also used for the recognition of the other unfolded substrate proteins including PhoA and OmpA[15]. The indole ring of MBP W256 inserts into the hydrophobic pocket of TF^{PPD} formed by F168, F177, I195, F198, F217, Y221, and F233 (Figure 2.8C, 2.9A). MBP P255, which is located next to the tryptophan residue, is captured by the hydrophobic cleft formed by I195, P196, F217, P218, Y221, and H222. The amino acid residues of TF^{PPD} that are involved in the recognition of the sequence MBP P255-W256 are highly conserved

(Figure 2.8D). Interestingly the proline-aromatic amino acid sequence is also found in the other peptide sequence recognized by TF^{PPD}. For example, MBP P180, which is located next to tyrosine residue (Y181), was found to be recognized by TF^{PPD} from NMR titration experiments (Figure 2.2B, 2.8B), and RNase T1 P39 and P55, whose cis/trans isomerization is known to be catalyzed by TF^{PPD} [18], are located next to tyrosine or histidine residues (Figure 2.8B). Taking these observations into consideration, I propose the proline-aromatic motif as the target for the recognition and *cis/trans* isomerization by TF^{PPD}. In addition to MBP P255-W256, another tryptophan residue in the hydrophobic stretch, W258, is recognized by TF^{PPD} through the interaction with the hydrophobic cleft formed by F177, Y221, A223, and L226 (Figure 2.8C). In addition to the hydrophobic interactions, a hydrogen bond between TF^{PPD} H222 $N^{\varepsilon 2}$ and the backbone carbonyl oxygen of MBP P255 is found in the complex. All these interactions contribute to holding tightly the MBP stretch P255-W258. On the other hand, MBP G254, which is located at the N-terminus of P255, is positioned at the edge of TF^{PPD} and no significant contact with TF^{PPD} was observed. It is worth noting that in the structure of the MBP-TF^{PPD} complex, in which P255 is in the *trans* form, the backbone carbonyl oxygen of MBP G254 is located nearby the backbone amide proton of TF^{PPD} I195, but not close enough to form a hydrogen bond (Figure 2.8C).

Although MBP P255 in the unbound MBP198-265 is in slow exchange between trans and cis forms as represented by the two sets of the NMR signals (Figure 2.9C), MBP P255 in complex with TF^{PPD} was found to adopt the *trans* form, as can be deduced from the single set of the resonances whose chemical shifts are in the range expected for trans form[19] (Figure 2.9D). This observation was consistent with the results of the titration experiments in which the resonances from MBP were monitored (Figure 2.9E). When TF^{PPD} was titrated into isotopically labeled MBP160-201 or MBP198-265, the resonances corresponding to the *trans* form showed more significant peak intensity reduction (Figure 2.9E, lower panels), implying stronger interaction between TF^{PPD} and the trans form of

the substrate protein. On the other hand, this trend was not observed upon the addition of TF^{SBD} (Figure 2.9E, upper panels). These results indicate the binding preference of TF^{PPD} toward proline residue in the *trans* form.

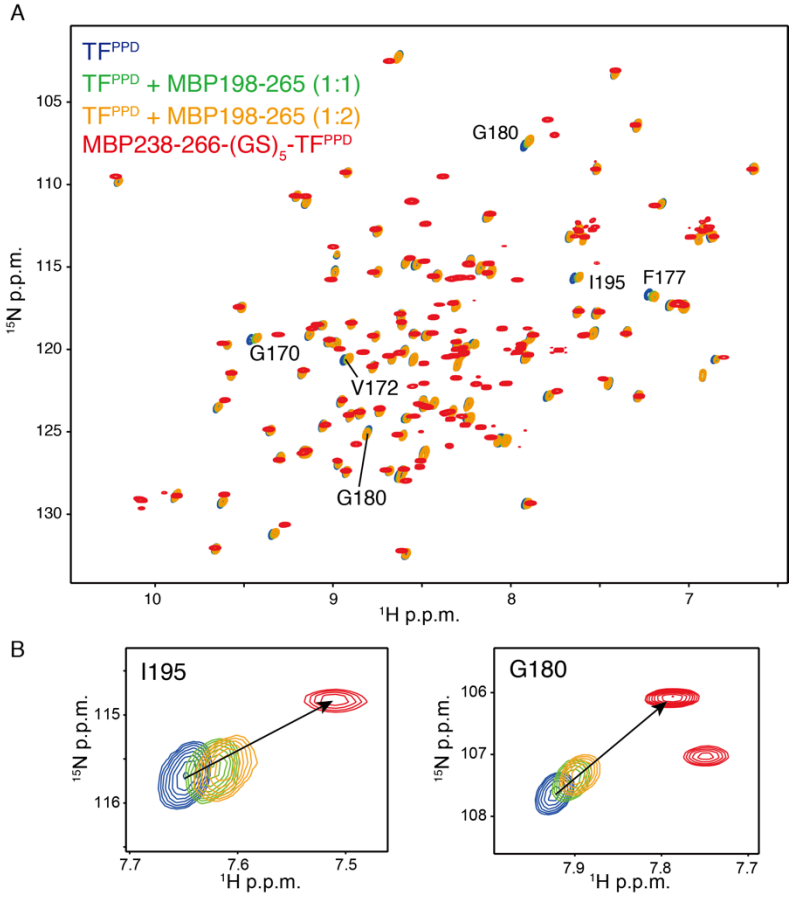

Figure 2.7 Evaluation of MBP238-266-$(GS)_5$-TF^{PPD} fusion by NMR
(A) ^{1}H-^{15}N HSQC spectra of ^{15}N-labeled TF^{PPD} in the absence (blue) and presence of MBP198-265 at TF^{PPD}:MBP 1:1 (green) or 1:2 (orange) ratios superimposed with the spectrum of ^{15}N-labeled MBP238-266-$(GS)_5$-TF^{PPD} fusion (red). The assignments are indicated for representative perturbed resonances. (B) The expanded views of the selected regions of the spectra showing the resonances from I195 (left panel) and G180 (right panel). The directions of the chemical shift change of the resonances from TF^{PPD} upon the fusion of MBP238-266 coincide with those observed by the addition of MBP198-265, indicating that the binding mode between the MBP fragment and TF in the isolated forms is preserved in the fusion protein of MBP238-266-$(GS)_5$-TF^{PPD}. The direction of the chemical shift change is indicated by an arrow.

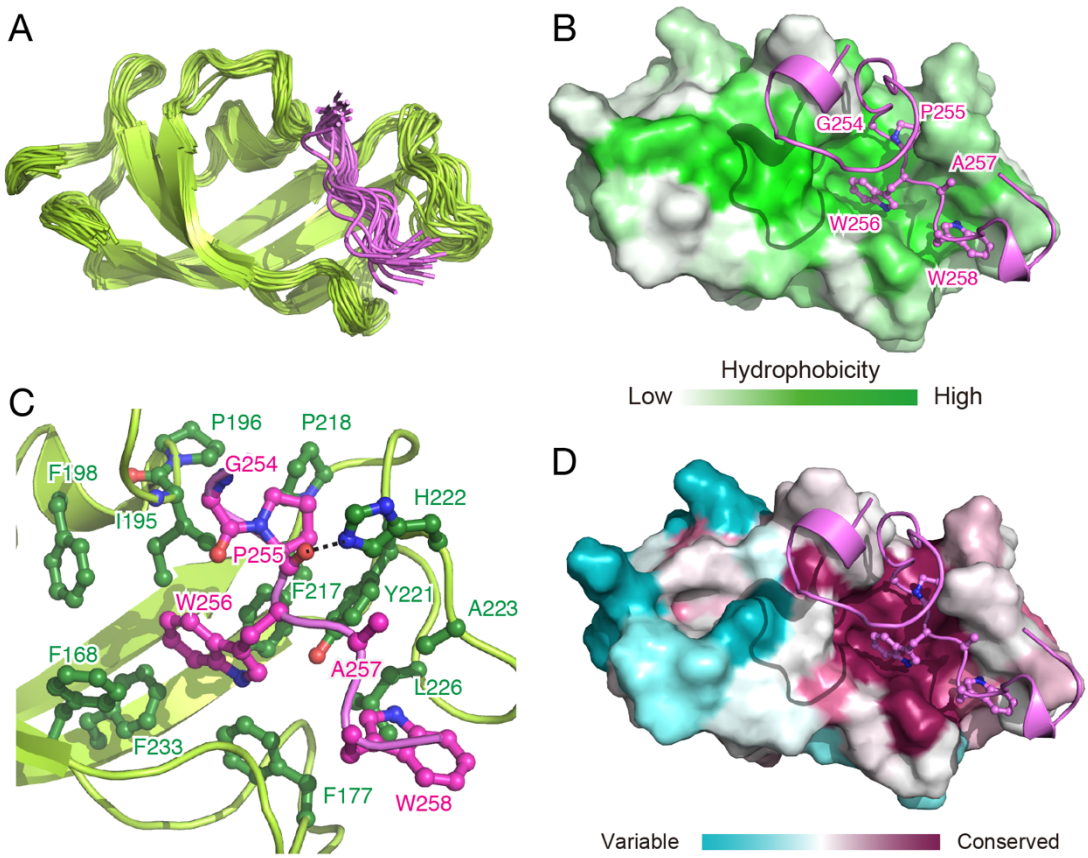

Figure 2.8 NMR structure of TF^{PPD} in complex with MBP.
(A) Superimposition of 20 structures of TF^{PPD} in complex with MBP 238-266. For MBP, only converged region, N253-S259, is shown for clarity. TF^{PPD} and MBP are shown in green and pink ribbons, respectively. (B and D) The lowest-energy structure of MBP-TF^{PPD} complex. TF^{PPD} is shown as a solvent-exposed surface to which the hydrophobicity (B) or the conservation of the amino acid residues (D) is mapped. MBP is shown as pink ribbon. The MBP residues that directly interact with TF^{PPD} are drawn in a ball-and-stick representation. (C) Close-up view of the lowest-energy structure of MBP-TF^{PPD} complex. TF^{PPD} and MBP are shown as green and pink ribbons, respectively. The residues of TF^{PPD} and MBP involved in the interaction are drawn in a ball-and-stick representation and colored green and pink, respectively.

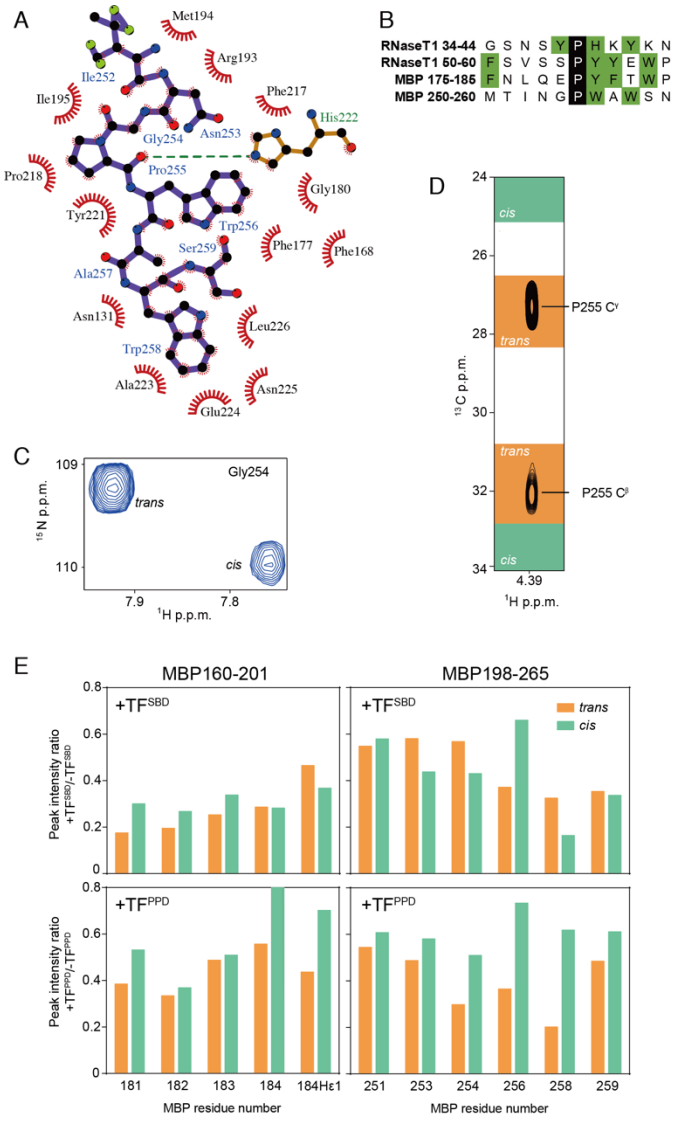

Figure 2.9 Recognition of MBP by TF^{PPD}

(A) Schematic representation of the intermolecular contacts between TF^{PPD} and MBP generated by Ligplot (http://www.ebi.ac.uk/thornton-srv/software/LIGPLOT/). MBP residues are shown in ball-and-stick representation with purple sticks, and the positions of the residues of TF^{PPD} responsible for the hydrophobic contacts with MBP are indicated by red spoked arcs. The hydrogen bond between TF^{PPD} H222, represented by balls and orange sticks, and MBP P255 is indicated by a green dotted line. (B) Amino acid sequences of the selected regions of RNase T1 and MBP that are recognized by TF^{PPD}. Proline residues and aromatic residues are highlighted in black and green, respectively. (C) The expanded view of the ^{1}H-^{15}N HSQC spectrum of ^{15}N MBP198-265 showing a set of the resonances from G254 in *trans* and *cis* forms. (D) (H)CCH-TOCSY strip showing the cross peaks for MBP Pro255 C$^{\beta}$ and C$^{\gamma}$ atoms in the MBP238-266-(GS)$_5$-TF^{PPD} fusion. The ranges of ^{13}C shifts for *trans* and *cis* isomers (24) are highlighted in orange and green, respectively. (E) Intensity ratio for the resonances from MBP160-201 (left panels) and MBP198-265 (right panels) in the absence and presence of TF^{SBD} (top panels) and TF^{PPD} (bottom panels). The ratios are plotted only for the amino acid residues giving two sets of the resonances corresponding to *cis* and *trans* forms. In both of the MBP fragments, the resonances from *trans* conformation exhibited more significant intensity reduction by the addition of TF^{PPD}, while the trend was not observed by the addition of TF^{SBD}.

Table 2.1. Structural and NMR statistics of TF^{PPD}-MBP complex.

Distance restraints	
NOEs	
Short range (intra-residue and sequential)	598
Medium range ($1 < \mid i-j \mid < 5$)	151
Long range ($\mid i-j \mid \geqq 5$)	434
Intermolecular	22
Hydrogen bonds	20
Dihedral angle restraints(ϕ and ψ)	128
Violations (mean and SD)	
Distance restraints(Å)	0.0032 ± 0.01960
Dihedral angle restraints(°)	0.68 ± 1.20
Structural coordinates rmsd[a]	
Backbone atoms	0.76 Å
All heavy atoms	1.21 Å
Ramachandran plot	
Most-favored regions	88.7%
Additionally allowed regions	11.2%
Generously allowed regions	0.1%
Disallowed regions	0.0%

[a]Analysis applied to the residues except the MBP238-266, GS-linker, and the flexible loops.

2.3.3 An Intermolecular Hydrogen Bond is Formed at the Transition State in the *cis/trans* Isomerization

To investigate the recognition of the substrate protein by TF^{PPD} during the *cis/trans* transition, I performed molecular dynamics (MD) simulation, using the lowest-energy structure of the MBP-TF^{PPD} complex determined by NMR as a starting point. Since proline *cis/trans* isomerization is slow compared to the timescale of MD simulation, a constrained MD simulation was performed in which a rotational angle constraint for the ω angle between MBP G254 and P255 was added and the ω angle was rotated from the initial angle (ω = -174°, trans) to the angle corresponding to *cis* form (ω = 0°) with clockwise or counterclockwise direction, as seen from the N-terminal to the C-terminal direction along the C-N bond, at a rate of 0.2 degree per 2 picosecond (Figure 2.10A). The simulation identified that the distance between the H^N atom of TF^{PPD} I195 and the carbonyl oxygen of MBP G254 (H^N-O distance) decreased as the ω angle rotates in clockwise direction. At ~0.8 ns, the ω angle reached approximately to -90° (*syn* state) and the distance became within the range of the formation of a strong hydrogen bond (< 2.5 Å) (Figure 2.10B). For example, at 0.200 ns of the clockwise rotation, where the ω angle was -160° (*trans* state), the H^N-O distance was 4.3 Å and the angle between the N and H^N atoms of TF^{PPD} I195 and the carbonyl oxygen of MBP G254 (N-H^N-O angle) was 134° (Figure 2.10C). Thus, no formation of the intermolecular hydrogen bond between TF^{PPD} I195 and MBP G254 was detected at the trans state. On the other hand, at 0.794 ns of the clockwise rotation, where the ω angle was -97° (*syn* state), the H^N-O distance was 2.1 Å and the N-H^N-O angle was 152° (Figure 2.10D). Both the H^N-O distance and the N-H^N-O angle at the syn state are in the range expected for a strong hydrogen bond formation[20]. It is worth mentioning that the rotation of the peptide bond in the other direction resulted no shortening of the H^N-O distance (Figure 2.10B), thereby no formation of the intermolecular hydrogen bond.

The simulation also indicated that the intermolecular hydrogen bond formed at the *syn* state tethers MBP P255 to the hydrophobic cleft of TF^{PPD}, and consequently, MBP

P255 and the peptide bond between MBP G254 and P255 are closely packed in the hydrophobic cleft (Figure 2.10D). When the ω angle rotated beyond the syn state, the backbone carbonyl oxygen atom of MBP G254 moves away from the backbone amide group of TF^{PPD} I195, resulting in the deformation of the intermolecular hydrogen bond and the subsequent release of the close hydrophobic packing between the peptidyl-prolyl bond and TF^{PPD} (Figure 2.10B). As expected from the structure of TF^{PPD} in complex with MBP (Figure 2.8C), the C-terminal segment of the MBP (P255-W258) was tightly held by TF^{PPD} during the ω angle rotation, and consequently the N-terminal segment preceding MBP P255 rotates in concurrence with the rotation of the ω angle. As seen in Figure 2.10C and D, the position and orientation of MBP G254 against TF^{PPD} change as the ω angle rotates.

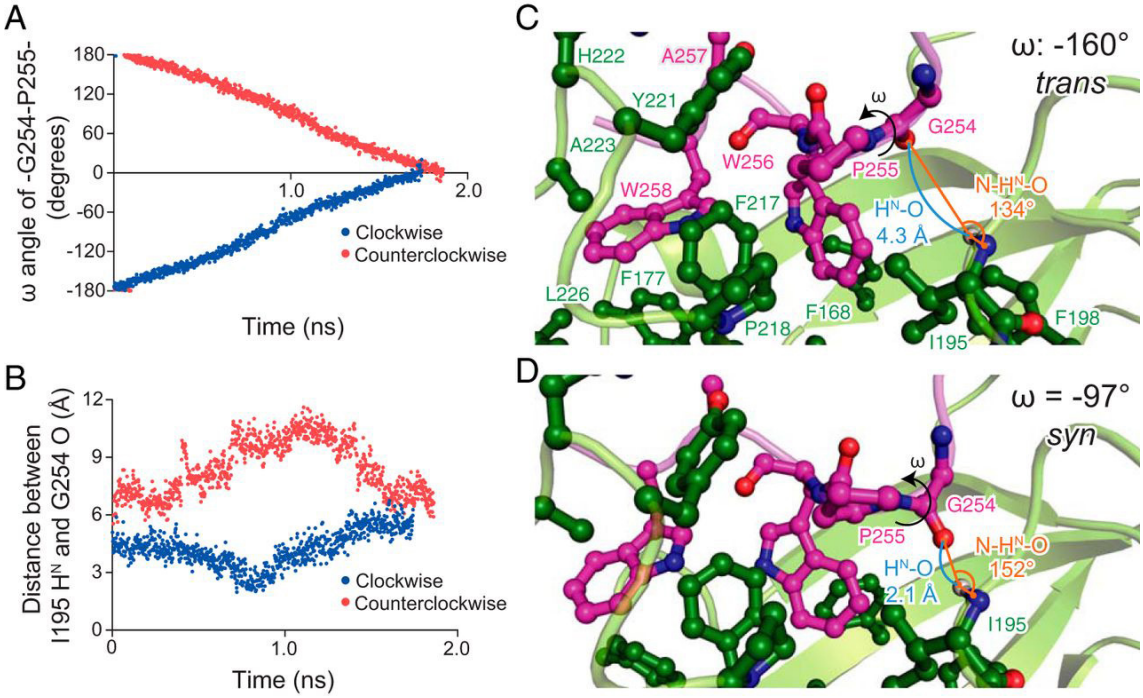

Figure 2.10 Molecular dynamics simulation of cis/trans isomerization by TF^{PPD}.
(A) Plots of the ω dihedral angle for the peptidyl-prolyl bond between MBP G254 and P255. The simulation was started from the NMR structure of MBP-TF^{PPD} complex in which the ω angle for the peptidyl-prolyl bond between MBP G254 and P255 is -174° (*trans* state). Due to the ω angle constraint at a rate of 0.2 degree per 2 picosecond, the ω angle changed linearly as a function of time. (B) Plots of the distance between the H^N atom of TF I195 and the carbonyl oxygen of MBP G254 as a function of time when the ω angle was rotated in clockwise (blue) or counterclockwise (red) direction. When the ω angle was rotated in clockwise direction, the two atoms approached to each other and the distance became shorter than 2.5 Å at ~0.8 ns. As seen in the panel A, the ω dihedral angle at 0.8 ns was around -90° (*syn* state). Snap shots of the *cis/trans* isomerization at the *trans* state (0.200 ns) (C) and the *syn* state (0.794 ns) (D). The intermolecular hydrogen bond between backbone amide group of TF^{PPD} I195 and the backbone carbonyl oxygen of MBP G254 is formed at the *syn* state, which tethers the peptidyl-prolyl bond closer onto the hydrophobic cleft formed by TF^{PPD} I195, F217, and P218.

2.3.4 The Intermolecular Hydrogen Bond between TF^{PPD} I195 and MBP G254 at the Transition State is Critical for the PPIase Activity

The role of the intermolecular hydrogen bond between the H^N atom of TF^{PPD} I195 and the carbonyl oxygen of MBP G254 in the *cis/trans* isomerization was evaluated by the activity assays performed using TF mutants, for which mutations of I195P, R193P, and M194P were designed. TF I195P is devoid of the H^N atom at the position of 195, and R193P and M194P were designed to perturb the position of the H^N atom of TF^{PPD} I195 as a result of the restricted backbone dihedral angle of the proline residue. In order to

monitor the PPIase activity of the TF mutants, I performed an RNase T1 refolding assay[18], in which the refolding of the reduced and carboxymethylated RNase T1 (RCM-RNase T1) was monitored by the increase of the intrinsic tryptophan fluorescence intensity (Figure 2.11A). Refolding of RCM-RNase T1 is limited by the slow *trans*-to-*cis* isomerization of peptidyl-prolyl bonds at P39 and P55[18]. Although the refolding of RCM-RNase T1 in the absence of TF was slow, it was significantly accelerated by the addition of TF (Figure 2.11A). However, no enhancement of the refolding was observed in the presence of $TF^{\Delta PPD}$, which confirmed that the PPIase activity dominates the foldase activity of TF in the refolding of RCM-RNase T1. The mutants TF I195P, TF M194P, and TF R193P exhibited significantly reduced activity (Figure 2.11A). The foldase activity of TF in the refolding of RCM-RNase T1 was more significantly affected when the proline substitution was closer to TF I195. On the other hand, the mutations of M194A or I195L induced smaller effect in the refolding of RCM-RNase T1 (Figure 2.12), supporting the idea that the backbone H^N atom of TF^{PPD} I195 plays an important role in the cis/trans isomerization. A mutation introduced at H222, which forms a hydrogen bond with backbone carbonyl oxygen of MBP P255, moderately reduced the refolding rate of RCM-RNase T1 (Figure 2.12), which suggests that the hydrogen bond mediated by H222 is also important in holding the substrate.

High sequence conservation of I195 and H222 in the TF family also supports the importance of the two amino acid residues for PPIase activity (Figure 2.13A). The comparison of the structures of TF^{PPD} and FKBP12 revealed that TF I195 and H222 are also structurally conserved in FKBP, which suggests a shared isomerization mechanism between these two proteins (Figure 2.13B).

Note that all of the TF mutants were expressed and purified in a soluble form. Furthermore, ^{1}H-^{15}N HSQC spectra of $TF^{PPD\text{-}SBD,\ M194P}$ and $TF^{PPD\text{-}SBD,\ I195P}$ clearly showed the native fold of $TF^{PPD\text{-}SBD}$ is preserved even after the introduction of these mutations (Figure 2.14A and B). The NMR spectra of ^{15}N $TF^{PPD\text{-}SBD,\ I195P}$ in the presence of MBP

198-265 indicated the same binding site on TF^{PPD} is used for the recognition of MBP, which supports the preservation of the interaction between TF^{PPD} and MBP in the TF I195P mutant (Figure 2.14C). Thus TF I195P binds to the substrate protein, but is inactive in the *cis/trans* isomerization due to the lack of the ability to form the intermolecular hydrogen bond at the transition state.

The effect of the mutation of I195P was also evaluated by NMR relaxation experiments. I performed ^{15}N relaxation dispersion experiment[21,22] on the fusion proteins: MBP238-266-$(GS)^5$-TF^{PPD} and MBP238-266-$(GS)^5$-$TF^{PPD,I195P}$ (Figure 2.11B). The backbone amide resonance from MBP G254 exhibited significant dispersion curve with an exchange rate constant, kex, of 740 s^{-1} at 35°C (Figure 2.11B, left panel), whereas the chemical exchange was disappeared by the introduction of the I195P mutation to TF^{PPD} (Figure 2.11B, right panel). Combined with the fact that the MBP G254 bound to TF^{PPD} indicated only a single set of the resonances whose chemical shifts are in the range expected for *trans* form (Figure 2.9D), the data indicate that the relaxation dispersion curve seen from the resonance of MBP G254 reflects the exchange between *trans* and *cis* forms of MBP P255 as major and minor states, respectively. Note that the exchange for binding and release of MBP is expected to be much faster, given the fact that the binding and release of unfolded PhoA gives rise to kex of ~1300 s^{-1} at 22°C[15]. The exchange rate indicates that the cis/trans isomerization of MBP P255 on TF^{PPD} is quite fast compared to the uncatalyzed isomerization (~0.01 s^{-1} at 35°C)[23]. Suppression of the chemical exchange by the introduction of the I195P mutation further corroborates the idea that I195 H^N is a catalytic center for the peptidyl-prolyl *cis/trans* isomerization by TF^{PPD}.

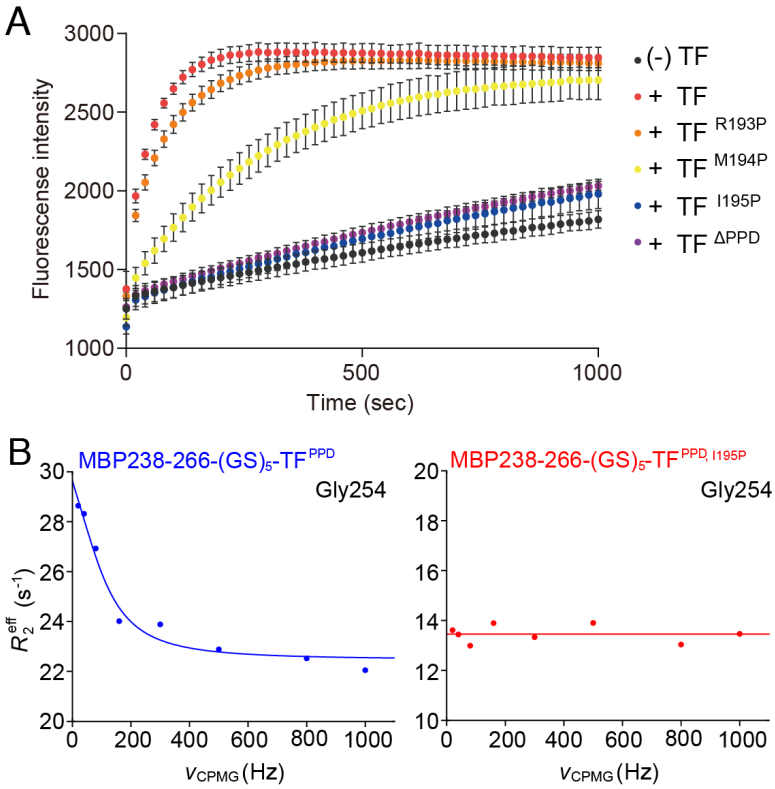

Figure 2.11 PPIase activity of TF and TF mutants.
(A) Evaluation of PPIase activity of TF and TF variants by refolding assay of RCM-RNase T1. Refolding of RCM-RNase T1 in the absence and presence of TF or TF mutants was monitored by increase of intrinsic tryptophan fluorescence at 320 nm after excitation at 268 nm. The experiments were performed at 15°C. Due to the complex process of the refolding of RCM-RNase T1 (37), refolding rates were not extracted. (B) Evaluation of PPIase activity of TF and TF variants by NMR relaxation dispersion experiments. The chemical exchange in MBP G254 coupled with *cis/trans* isomerization of peptidyl-prolyl bond between MBP G254 and P255 in complex with TF^{PPD} (left panel) or $TF^{PPD, I195P}$ (right panel) were monitored.

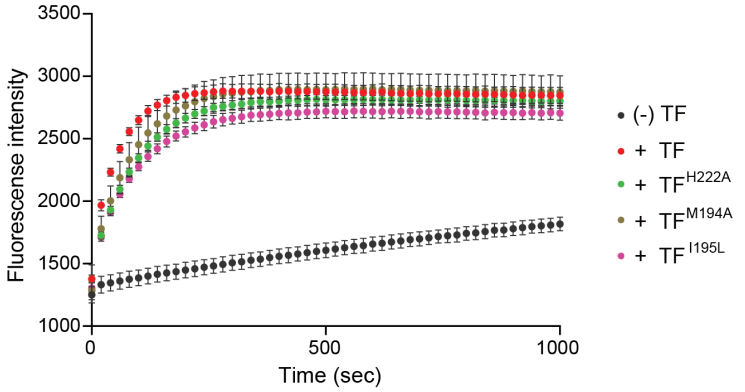

Figure 2.12 Evaluation of the PPIase activity of TF and TF mutants.
Refolding of RCM-RNase T1 in the absence and presence of TF variants. Refolding of RCM-RNase T1 was monitored by increase of intrinsic tryptophan fluorescence at 320 nm after excitation at 268 nm. The experiments were performed at 15°C.

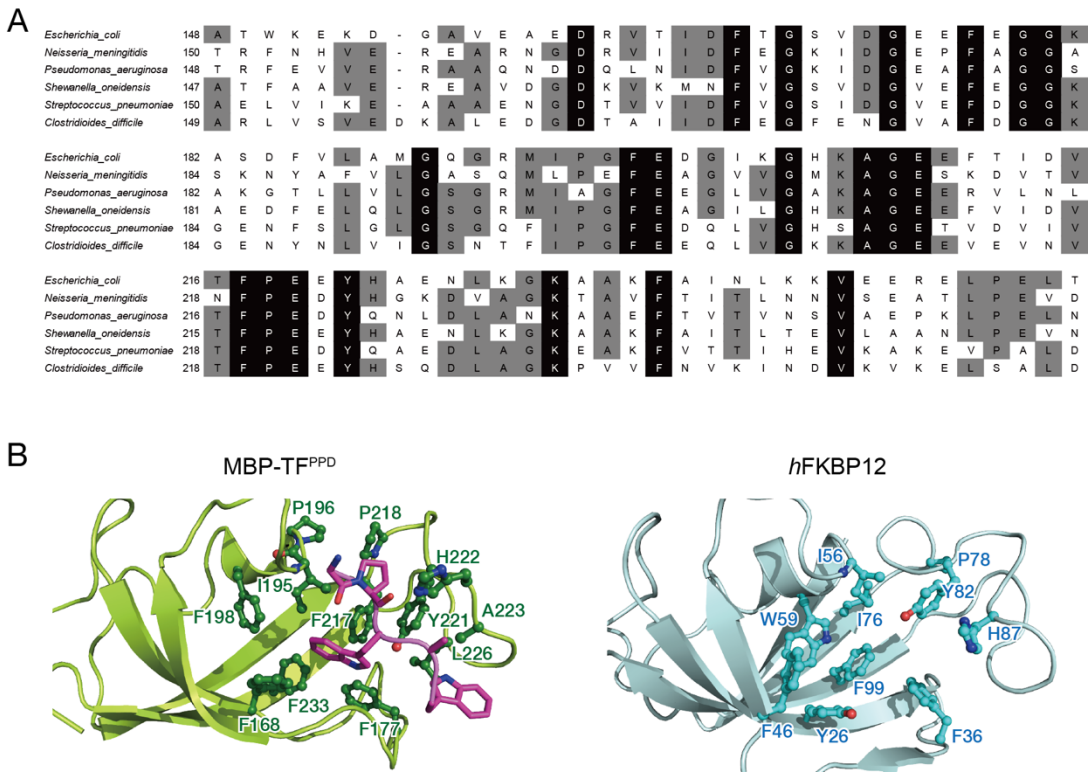

Figure 2.13 Conservation of the amino acid residues of TF^{PPD} involved in the *cis/trans* isomerization

(A) Multiple sequence alignment for TF^{PPD} from a variety of organisms. The conserved residues are highlighted. (B) Comparison of the structure of TF^{PPD} in complex with MBP (left panel) with that of human FKBP12 (PDB ID: 1FKF) (right panel). TF^{PPD}, MBP, and FKBP12 are colored green, magenta, and cyan, respectively. The residues in the MBP-TF^{PPD} complex that mediates the interaction and the corresponding amino acid residues in FKBP12 are shown in ball-and-stick representation.

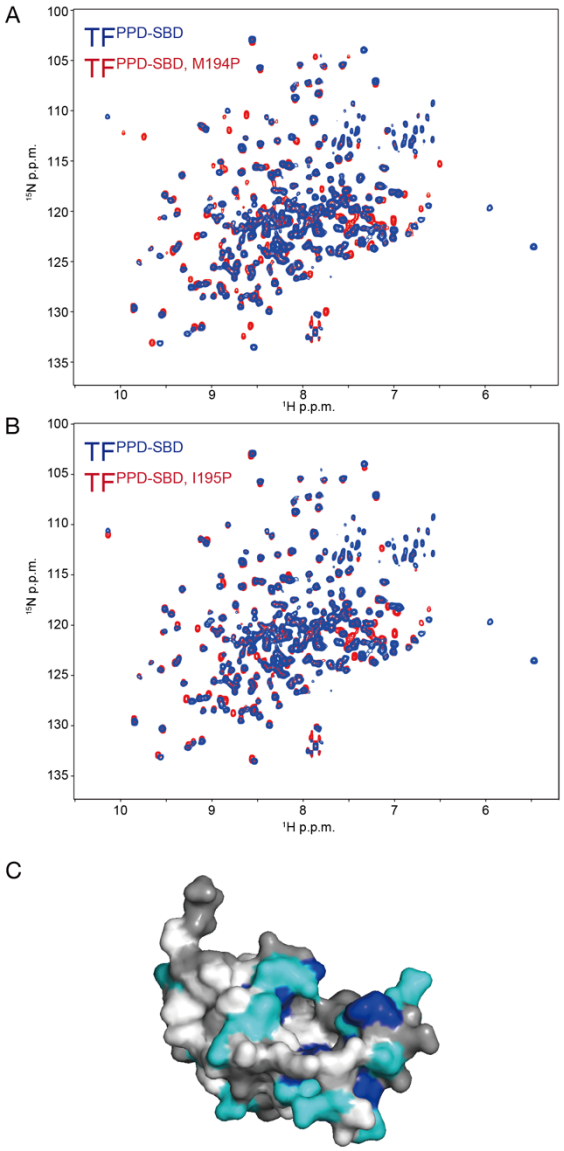

Figure 2.14 Mutants of $TF^{PPD\text{-}SBD}$ characterized by NMR
Overlay of the ^{1}H-^{15}N HSQC spectra of wild type (blue) and mutants (red) of $TF^{PPD\text{-}SBD}$. The spectra of $TF^{PPD\text{-}SBD,\ M194P}$ (A) and $TF^{PPD\text{-}SBD,\ I195P}$ (B) are overlaid with that of wild type $TF^{PPD\text{-}SBD}$. The spectra clearly show that $TF^{PPD\text{-}SBD,\ M194P}$ and $TF^{PPD\text{-}SBD,\ I195P}$ maintain the native fold. (C) Mapping of the chemical shift perturbations of $TF^{PPD\text{-}SBD,\ I195P}$ upon the addition of MBP198-265 at 1:1 ratio. The residues with perturbations larger than the threshold values of 0.015 and 0.025 ppm are colored light blue and dark blue, respectively. Proline and unassigned residues are colored gray.

2.4. Discussion

In this chapter, I focused on the PPIase to elucidate the foldase activity of chaperone in the Hsf1-chaperone system. To elucidate the PPIase mechanism of TF chaperone, I conducted the NMR structural analysis, molecular dynamics simulation, and mutational studies. These results led us to propose a mechanistic model of proline *cis/trans* isomerization by TF as follows (Figure 2.15). As seen in the structure of TF^{PPD} in complex with the unfolded MBP, TF^{PPD} recognizes the proline-aromatic motif located in the hydrophobic stretch of the substrate protein. TF^{PPD} captures the proline-containing peptide in *trans* conformation, using its conserved hydrophobic cleft as decollated by TF H222 forming a hydrogen bond with the backbone carbonyl oxygen of the proline residue in the substrate protein (Figure 2.8, 2.9B). Consequently, the proline residue and the C-terminal stretch of the substrate protein are tightly held on TF^{PPD}, while the residue preceding the proline has no significant contact with TF^{PPD} (Figure 2.8C). However, the MD simulation has revealed that as the peptidyl-prolyl bond rotates, the backbone carbonyl oxygen atom of the amino acid residue preceding the proline residue in the substrate protein moves toward the TF I195 backbone amide group, which eventually results in the formation of the intermolecular hydrogen bond at the intermediate syn state with an ω angle of approximately -90° (Figure 2.10D). Thus, the energy barrier of *cis/trans* isomerization (~20 kcal/mol) is expected to be partially compensated by the formation of the intermolecular hydrogen bond with a bond energy of ~5 kcal/mol[24]. Note that the N-terminal stretch of the substrate protein rotates during the isomerization, while the proline residue and the C-terminal stretch stay on TF^{PPD} (Figure 2.10). The important role of the intermolecular hydrogen bond was further supported by NMR relaxation studies and activity assays in which the perturbations to the backbone amide group of TF I195 by mutagenesis significantly reduced the PPIase activity of TF (Figure 2.11). Furthermore, our structural study has also revealed the hydrophobic environment around the peptidyl-prolyl bond. The proline residue in the substrate protein is lodged in the

hydrophobic cleft of TF^{PPD} at the ground state (Figure 2.8B, C), and the formation of the intermolecular hydrogen bond at the transition state tethers the peptidyl-prolyl bond even closer to the hydrophobic surface of the cleft (Figure 2.10D). Given the fact that the hydrophobic environment promotes *cis/trans* isomerization as shown by previous mutational studies[25,26], our observation suggests that the hydrophobic environment around the peptidyl-prolyl bond at the syn state contributes to the isomerase activity of TF^{PPD}. Thus, the combination of the intermolecular hydrogen bond mediated by TF^{PPD} I195 H^N and the hydrophobic environment around the peptidyl-prolyl bond during the transition is important for eliminating the energy barrier, thereby accelerating the *cis/trans* isomerization.

In this study, I used the TF chaperone as a model for PPIase. FKBP-type PPIase as TF exists in eukaryotes such as FKBP12, FKBP51, FKBP52, and FKBP51 and 52 are known to form a complex with Hsp90 chaperone to assist in substrate protein folding[27]. The comparison of the structures of TF^{PPD} and FKBP12 revealed that the structures of FKBP-type PPIase are highly conserved (Figure 2.13B), which suggests a shared isomerization mechanism in FKBP-type PPIases. This study has identified that TF^{PPD} possesses the moderate specificity toward the proline-aromatic motif in the hydrophobic stretches of the substrate protein (Figure 2.2, 2.9B), suggesting that PPIase, which act as catalytic domain of chaperone, preferentially accelerates the proline *cis/trans* isomerization of the peptidyl-prolyl bond in the hydrophobic stretch of the substrate protein that is eventually folded into the core of the protein in its native fold.

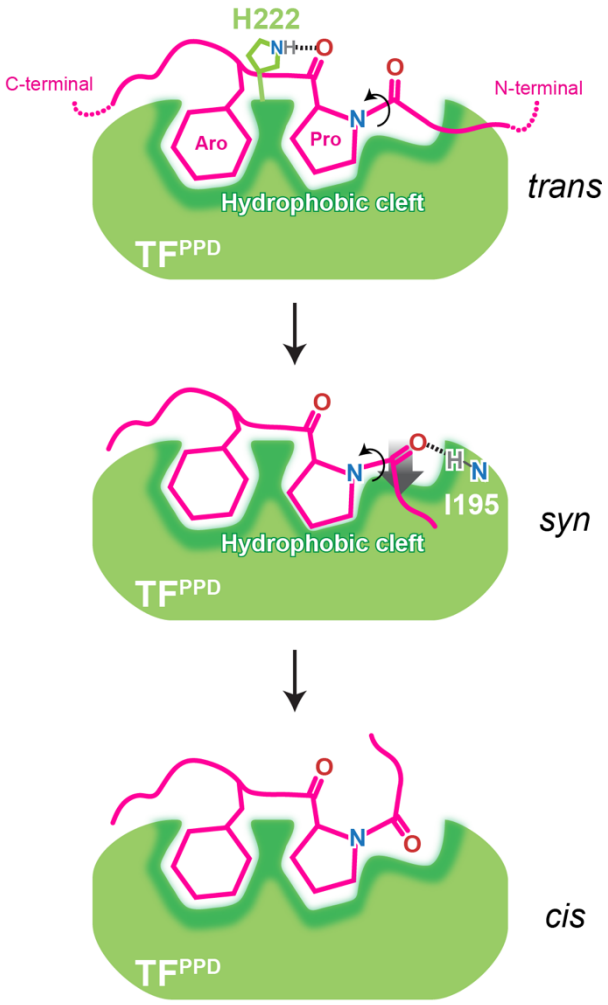

Figure 2.15 Schematic representation of peptidyl-prolyl *cis/trans* isomerization by TF^{PPD}. TF^{PPD} and the substrate protein are show in green and magenta, respectively. TF^{PPD} captures the proline-aromatic motif in the *trans* form located in the hydrophobic stretches of the substrate protein. The interaction is mainly mediated by hydrophobic interactions with the conserved hydrophobic cleft of TF^{PPD} that is decollated by TF H222 forming a hydrogen bond with the backbone carbonyl oxygen of the proline residue in the substrate. When the peptidyl-prolyl bond rotates to *syn* form, the carbonyl oxygen of the amino acid residue preceding the proline residue forms an intermolecular hydrogen bond with backbone amide group of TF^{PPD} I195, which tethers the peptidyl-prolyl bond onto the hydrophobic surface of the TF^{PPD}. Both the intermolecular hydrogen bond and the hydrophobic environment are important for efficient *cis/trans* isomerization. When the peptidyl-prolyl bond rotates to *cis* form, the intermolecular hydrogen bond and consequently the close hydrophobic contact are released.

References

1. Ferbitz, L., Maier, T., Patzelt, H., Bukau, B., Deuerling, E., Ban, N. Trigger Factor in Complex with the Ribosome Forms a Molecular Cradle for Nascent Proteins. *Nature* **431**, 590–596 (2004).
2. Hesterkamp, T., Bukau, B. Identification of the Prolyl Isomerase Domain of *Escherichia Coli* Trigger Factor. *FEBS Lett* **385**, 67–71(1996).
3. Stoller, G., Rücknagel, K. P., Nierhaus, K. H., Schmid, F. X., Fischer, G., Rahfeld, J. U. A Ribosome-Associated Peptidyl-Prolyl Cis/Trans Isomerase Identified as the Trigger Factor. *EMBO J.* **14**, 4939–4948 (1995).
4. Delaglio, F., Grzesiek, S., Vuister, G. W., Zhu, G., Pfeifer, J., Bax, A. NMRPipe: A Multidimensional Spectral Processing System Based on UNIX Pipes. *J. Biomol. NMR* **6**, 277–293 (1995).
5. Kuriyan, J., Eisenberg, D. The Origin of Protein Interactions and Allostery in Colocalization. *Nature* **450**, 983–990 (2007).
6. Herrmann, T., Güntert, P., Wüthrich, K. Protein NMR Structure Determination with Automated NOE Assignment Using the New Software CANDID and the Torsion Angle Dynamics Algorithm DYANA. *J. Mol. Biol.* **319**, 209–227 (2002).
7. Shen, Y., Delaglio, F., Cornilescu, G., Bax, A. TALOS+: A Hybrid Method for Predicting Protein Backbone Torsion Angles from NMR Chemical Shifts. *J. Biomol. NMR* **44**, 213–223 (2009).
8. Brunger, A. T. Version 1.2 of the Crystallography and NMR System. *Nat. Protoc.* **2**, 2728–2733 (2007).
9. Loria, J. P., Rance, M., Palmer, III, A. G. A TROSY CPMG Sequence for Characterizing Chemical Exchange in Large Proteins. *J. Biomol. NMR* **15**, 151–155. (1999).
10. Bieri, M., Gooley, P. R. Automated NMR Relaxation Dispersion Data Analysis Using NESSY. *BMC. Bioinformatics* **12**, 421 (2011).
11. Luz, Z., Meiboom, S. Nuclear Magnetic Resonance Study of the Protolysis of Trimethylammonium Ion in Aqueous Solution—Order of the Reaction with Respect to Solvent. *J. Chem. Phys.* **39**, 366. (2004).
12. Ryckaert, J.-P., Ciccotti, G., Berendsen, H. J. C. Numerical Integration of the Cartesian Equations of Motion of a System with Constraints: Molecular Dynamics of n-Alkanes. *J. Comput. Phys.* **23**, 327–341. (1997).
13. Mücke, M., Schmid, F. X. Enzymatic Catalysis of Prolyl Isomerization in an Unfolding Protein. *Biochemistry* **31**, 7848–7854 (1992).
14. Huang, C., Rossi, P., Saio, T., Kalodimos, C. G. Structural Basis for the Antifolding Activity of a Molecular Chaperone. *Nature* **537**, 202–206 (2016).
15. Saio, T., Guan, X., Rossi, P., Economou, A., Kalodimos, C. G. Structural Basis for Protein Antiaggregation Activity of the Trigger Factor Chaperone. *Science* **344**, 1250494 (2014).
16. Patzelt, H., Rüdiger, S., Brehmer, D., Kramer, G., Vorderwülbecke, S., Schaffitzel, E., Waitz, A., Hesterkamp, T., Dong, L., Schneider-Mergener, J., Bukau, B., Deuerling, E. Binding Specificity of Escherichia Coli Trigger Factor. *Proc. Natl. Acad. Sci. U S A* **98**, 14244-9 (2001).
17. Teilum, K., Kunze, M. B. A., Erlendsson, S., Kragelund, B. B. (S)Pinning down Protein Interactions by NMR. *Protein Sci.* **26**, 436–451 (2017).
18. Kramer, G., Patzelt, H., Rauch, T., Kurz, T. A., Vorderwülbecke, S., Bukau, B., Deuerling, E. Trigger Factor Peptidyl-Prolyl Cis/Trans Isomerase Activity Is Not Essential for the Folding of Cytosolic Proteins in Escherichia Coli. *J. Biol. Chem.* **279**, 14165-70 (2004).
19. Schubert, M., Labudde, D., Oschkinat, H., Schmieder, P. A Software Tool for the Prediction of Xaa-Pro Peptide Bond Conformations in Proteins Based on 13 C Chemical Shift Statistics. *J. Biomol. NMR* **24**, 149–154 (2002).
20. Torshin, I. Y., Weber, I. T., Harrison, R. W. Geometric Criteria of Hydrogen Bonds in

Proteins and Identification of `bifurcated' Hydrogen Bonds. *Protein Eng, Des. and Sel.* **15**, 359–363 (2002).
21. Mittermaier, A., Kay, L. E. New Tools Provide New Insights in NMR Studies of Protein Dynamics. *Science* **312**, 224–228 (2006).
22. NMR Characterization of the Dynamics of Biomacromolecules. *Chem. Rev.* **104**, 3623–3640 (2004).
23. Brandts, J. F., Halvorson, H. R., Brennan, M. Consideration of the Possibility That the Slow Step in Protein Denaturation Reactions Is Due to Cis-Trans Isomerism of Proline Residues. *Biochemistry* **14**, 4953–4963 (1975).
24. Sheu, S.-Y., Yang, D.-Y., Selzle, H. L., Schlag, E. W. Energetics of Hydrogen Bonds in Peptides. *Proc. Natl. Acad. Sci. U S A* **100**, 12683–12687 (2003).
25. Ikura, T., Kinoshita, K., Ito, N. A Cavity with an Appropriate Size Is the Basis of the PPIase Activity. *Protein Eng. Des. and Sel.* **21**, 83–89 (2008).
26. Ikura, T., Ito, N. Requirements for Peptidyl-Prolyl Isomerization Activity: A Comprehensive Mutational Analysis of the Substrate-Binding Cavity of FK506-Binding Protein 12. *Protein Sci.* **16**, 2618–2625. (2007).
27. Storer, C. L., Dickey, C. A., Galigniana, M. D., Rein, T., Cox, M. B. FKBP51 and FKBP52 in Signaling and Disease. *Trends in Endocrinol. Metab.* **22**, 481–490 (2011).

CHAPTER III

Heat-induced Conformational Transition Mechanism of Heat Shock Factor 1 Investigated by Tryptophan probe

Abstract

Molecular chaperones express foldase function via PPIase activity to assist in the recovery of unfolded protein folding. The expression of these chaperones is quantitatively regulated through the assembly state changes of their transcriptional factor, Hsf1, to counter stress-induced protein denaturation and aggregation. Within this assembly event, oligomerization is its first step. Hsf1 exists in monomeric state under normal conditions, and becomes oligomer formed by intermolecular interaction between its leucine zipper domain (LZ1-3) upon elevation of temperature from 37°C to 42°C in the cell. Although this heat-induced oligomerization is the first step in the series of transcriptional regulation of Hsf1, the lack of information about Hsf1 monomer structure in the resting state, as well as the structural change via oligomerization at heat response, impeded the understanding of the oligomerization mechanism.

In this chapter, I aimed to uncover the heat-induced oligomerization mechanism of Hsf1. First, the monomeric structure of Hsf1 was estimated using the structure prediction program AlphaFold2 and molecular dynamics (MD) simulation, and it was shown that the monomer forms closed state, which LZ1-3 and a short leucine zipper domain (LZ4) interacts intramolecularly. To trace the oligomerization process, I performed Trp and ANS fluorescence experiments, and the results showed that Hsf1 does not just undergo a simple monomer/oligomer change, but also oligomerizes via “open” conformational intermediate, where the intramolecular LZ interaction is dissolved, as the temperature increases. Furthermore, circular dichroism spectroscopy and MD simulation showed that this conformational change to “open” state is coupled with the unfolding of LZ4. Therefore, the dissociation of LZ4 from LZ1-3 coupling with heat-induced LZ4 unfolding was considered to cause intermolecular interactions between LZ1-3 and their association with each other, leading to the oligomerization of Hsf1.

3.1. Introduction

In Chapter II, I analyzed the mechanism of PPIase, which plays a major role in the foldase activity of molecular chaperones. Since the amount of misfolded protein increases during stress, the Hsf1-chaperone system takes a countermeasure by upregulating the amount of chaperones having foldase function to prevent the accumulation of misfolded protein in the cell. In all eukaryotic cells, Hsf1 is responsible for transcriptional regulation of the molecular chaperones. The transcriptional activity is regulated by the assembly state changes.

Oligomerization of Hsf1 is the first step in its assemblystate changes. Hsf1 is mostly composed of intrinsically disordered regions (IDR) consisting of a regulatory domain (RegD) and C-terminal transactivation domain (CTAD), and has a DNA-binding domain (DBD) and the leucine-zipper domains (LZ1-3, LZ4) as structural domains (Figure 3.1A)[1]. Under normal conditions, Hsf1 exists in a monomeric state in the cytosol[2–5]. It was proposed that Hsf1 itself has the ability to regulate its own oligomeric state and maintain its monomeric state through intramolecular interactions between LZ1-3 and LZ4[6]. Purified Hsf1 oligomerizes in response to elevated temperatures, indicating that Hsf1 itself can function as a thermosensor[2,7,8]. The Hsf1 oligomer binds to the HSE DNA located in the promoter region upstream of the gene encoding chaperones and promotes transcription[9-11]. Thus, the monomer-oligomer transition of Hsf1 is critical for transcriptional regulation in Hsf1-chaperone system.

Several structural studies have been conducted to elucidate the molecular mechanism of Hsf1-mediated Hsf1-chaperone system. A model structure of the human Hsf1 trimer was obtained using the crystal structure of *Chaetomium thermophilum* Skn7 (160-209) that is homologous to the LZ1-3 domain of Hsf1, suggesting that LZ1-3 forms a trimer[12]. Moreover, the HSE DNA recognition mechanism was clarified using the crystal structures of the DBD-HSE complex[12–14]. These structural studies highlighted the detailed mechanisms by which Hsf1 oligomer recognizes HSE. On the other hand, the

mechanism by which Hsf1 alters its oligomeric state in response to heat is poorly understood. Several biochemical studies have implied that Hsf1 acts as a thermosensor by controlling temperature-dependent LZ1-3 and LZ4 interactions[6,7,10,15,16]. It has been reported that Hsf1 forms oligomers by deletion or substitution of LZ4, which disrupts the intramolecular interaction between LZ4 and LZ1-3 [6,15,16], leading to the hypothesis that the Hsf1 monomer is maintained by the intramolecular interaction between LZ1-3 and LZ4 under normal conditions, but under stress, this interaction is dissolved to allow intermolecular interaction among LZ1-3[6,10]. However, the transition mechanism from monomer to oligomer due to a change in the interaction between LZ1-3 and LZ4 has not been fully examined.

In this chapter, I aimed to uncover the mechanism of the Hsf1 heat response by investigating the temperature-dependent conformational transition of Hsf1 using solution biophysical methods. To obtain structural information on the Hsf1 monomer, the predicted structure was refined by molecular dynamics (MD) simulations. Next, the fluorescence derived from Trp169 located at LZ1-3 (Figure 3.1A, B) was monitored to track the temperature-dependent conformational changes and oligomerization of Hsf1. Moreover, in combination with its model fitting analysis, 8-anilino-1-naphtalene sulfonic acid (ANS) fluorescence, nuclear magnetic resonance (NMR), and circular dichroism (CD) spectroscopy, I found that the oligomer, the active form of Hsf1, is formed via the monomer of the open conformation, in which LZ1-3 dissociates from LZ4 at elevated temperatures. Furthermore, this conformational change to the open state is coupled with unfolding of the helix structure. This study revealed the existence of a monomeric open conformation of Hsf1 prior to oligomerization. This open/closed conformational change can be a key reaction for the regulation of its oligomeric state, as well as interactions with other regulators, such as molecular chaperones.

3.2. Materials and Methods

Expression and purification of protein samples

The human Hsf1, Hsf1 DBD, and Hsf1 W23F/W37F expression constructs were cloned into a pET21b vector (Cat. No. 69741-3CN, Novagen, Madison, Wisconsin, USA) and fused to GB1-His^6 tags at the HRV3C N-terminus of the protease cleavage site. Hsf1 DBD (1-120) and Hsf1 W23F/W37F were constructed through site-directed mutagenesis using the PrimeSTAR Mutagenesis Basal Kit (Cat. No. R046A, Takara Bio, Shiga, Japan). All the expression constructs were transformed into BL21(DE3) cells. The cells were grown in Luria-Bertani medium at 37°C, in the presence of ampicillin (50 μg ml^{-1}). Subsequently, protein expression was induced by adding 0.5 mM isopropyl-β-D-1-thiogalactopyranoside (IPTG) at OD_{600} ~0.6, followed by a 12 h to 16 h incubation at 18°C. Then, the cells were harvested at OD_{600} ~3.0, resuspended in a lysis buffer containing 50 mM Tris-HCl (pH 8.0) and 500 mM NaCl, disrupted by a sonicator, and centrifuged at 18,000 rpm for 30 min. The supernatant fraction containing Hsf1 was purified using an Ni-NTA Sepharose column (Cat. no. 30210, QIAGEN, Hilden, Germany). Additionally, the GB1-His^6 tag was removed using a HRV3C protease at 4 °C (incubation for 16 h), post which the cleaved Hsf1 was applied onto a HiTrap Q HP anion exchange column (Cat. No. 17115401, Cytiva, Tokyo, Japan), pre-equilibrated with 25 mM HEPES/NaOH (pH 7.5), 5 mM $MgCl_2$, 10% glycerol, 20 mM NaCl, and eluted with a linear gradient of 20–500 mM NaCl. Hsf1 oligomers and Hsf1 monomers were eluted separately through anion-exchange purification. Hsf1 oligomers were further purified by gel filtration using a Superdex 200 pg 16/600 column (Cat. No. 28989335, Cytiva) equilibrated with a solution containing 25 mM HEPES/KOH (pH 7.2) and 150 mM KCl. Finally, protein concentrations were determined spectrophotometrically at 280 nm using the corresponding extinction coefficient.

Fluorescence spectroscopy

Fluorescence measurements were performed using a JASCO FP-8300 spectrofluorometer and using solutions prepared in 25 mM HEPES/KOH (pH 7.2) and 150 mM KCl. Concentration of Hsf1 was 3.0 μM. The unpolarized emission spectra of tryptophan were recorded between 300 and 450 nm using an excitation wavelength of 295 nm and scan speed of 200 nm/min. Emission spectra of ANS (Sigma-Aldrich, St Louis, USA) were recorded between 400 and 700 nm using a 375 nm excitation wavelength and a scan speed of 200 nm/min. Concentration of ANS was 50 μM. FRET spectra were recorded between 300 and 700 nm using an excitation wavelength of 295 nm and scan speed of 200 nm/min. The excitation and emission slit widths were both set to 5 nm. Each spectrum represents an integration of three consecutive scans.

Fitting procedure of fluorescence spectra

The fluorescence spectral data were analyzed using a mathematical model and a global fitting algorithm. The oligomeric number of Hsf1 was formulated as a trimer, based on its crystal structure[12–14]. The mathematical model assumes a three-state transition ($3M \leftrightarrow 3I \leftrightarrow O$), written as:

$$K_{\mathrm{MI}}[M] = [I], \tag{3-1}$$

$$K_{\mathrm{IO}}[I]^3 = [O], \tag{3-2}$$

where K_{MI} and K_{IO} are the association constants for the reactions $M \leftrightarrow I$ and $I \leftrightarrow O$, respectively. $[\cdots]$ denotes that the concentration of Hsf1 in each state is normalized by the total concentration of Hsf1 in the sample. The temperature dependence of the association constants is written as:

$$K_{\mathrm{MI}} = \exp\left(-\frac{\Delta H_{\mathrm{MI}}}{RT}\left(1 - \frac{T}{T_{\mathrm{m,MI}}}\right)\right), \tag{3-3}$$

$$K_{\mathrm{IO}} = \exp\left(-\frac{\Delta H_{\mathrm{IO}}}{RT}\left(1 - \frac{T}{T_{\mathrm{m,IO}}}\right)\right), \tag{3-4}$$

where R is the gas constant, $T_{\mathrm{m,MI}}$ and $T_{\mathrm{m,IO}}$ are the midpoint temperatures of the reactions $M \leftrightarrow I$ and $I \leftrightarrow O$, respectively, and ΔH_{MI} and ΔH_{IO} are the molar enthalpy changes of the transition at $T_{\mathrm{m,MI}}$ and $T_{\mathrm{m,IO}}$, respectively. Combining equations (3-1)–(3-2) with the mass conservation law in the monomer unit yields the following equation:

$$3K_{\mathrm{IO}}K_{\mathrm{MI}}^{3}[M]^{3} + (K_{\mathrm{MI}} + 1)[M] = 1. \qquad (3-5)$$

The analytical solution for the equation (3-5) was obtained using Mathematica.

To fit the mathematical model to the fluorescence data, the thermodynamic parameters ΔH_{MI}, ΔH_{IO} $T_{\mathrm{m,MI}}$, and $T_{\mathrm{m,IO}}$ were numerically solved using an iterative method. Their initial values were set, $[M]$, $[I]$, and $[O]$ were calculated at each temperature according to equations (3-1)–(3-5), and the matrix of the population fraction C was the output. The matrix of the pure component spectra S of Hsf1 in the M, I, and O states was calculated using the classical least-squares method[17]:

$$S = (C^{T}C)^{-1}CD, \qquad (3-6)$$

where D is the matrix of the measured fluorescence data. The 2-norm of the error $E = |CS - D|_2$ was minimized by repeating the calculation with different initial parameter values, and the solutions obtained for the parameters were used to compare the experimental data.

SEC-MALS experiments

Size-exclusion chromatography with multi-angle light scattering (SEC-MALS) was performed using DAWN HELEOS8+ (Wyatt Technology Corporation, Santa Barbara, CA, USA), a high-performance liquid chromatography pump LC-20AD (Shimadzu, Kyoto, Japan), a refractive index detector RID-20A (Shimadzu), and a UV-vis detector SPD-20A (Shimadzu), which were located downstream of the Shimadzu liquid chromatography system connected to a PROTEIN KW-803 gel filtration column (Cat. No. F6989103, Shodex, Tokyo, Japan). Differential RI (Shimadzu) downstream of MALS was used to determine the protein concentrations. The running buffer used

contained 25 mM HEPES/KOH (pH 7.2) and 150 mM KCl. Approximately, 100 µL of the sample was injected at a flow rate of 1.0 mL min^{-1}. Data was then analyzed using ASTRA version 7.0.1 (Wyatt Technology Corporation). Molar mass analysis was also performed over half of the width of the UV peak top height. After 30 min incubation at 12℃, 27℃, and 42℃, 100 µL of 50 µM Hsf1 monomer sample was injected.

NMR Spectroscopy

NMR samples were prepared in 25 mM potassium phosphate buffer (pH 7.2), 150 mM KCl, 0.05% NaN_3, and 7% D_2O for 1D ^{19}F-NMR experiments or 20 mM MES (pH6.5), 100 mM NaCl, 5 mM $CaCl_2$, 0.02% NaN_3, 7% D_2O for 1D ^{1}H-NMR experiments. Concentration of Hsf1 was 100 µM, and concentrations of Hsf1 DBD and Hsf1 ΔDBD were 50 µM. The ^{19}F-NMR experiments were performed at 12°C. ^{19}F-NMR spectra and ^{1}H-NMR spectra were obtained with a Bruker AVANCE NEO 800 MHz spectrometer (Bruker, Billerica, MA) using a CPTCI ^{1}H/^{19}F- ^{13}C/^{15}N proton-optimized triple resonance cryoprobe. The 1D ^{19}F-NMR experiments were recorded with a data size of 131,072 complex points, an acquisition time of 367 ms, and 32,768 scans per experiment. The 1D ^{1}H-NMR experiments were recorded with a data size of 32,768 complex points, an acquisition time of 1,310 ms, and 128 scans per experiment. The spectra were processed using Bruker TOPSPIN version 3.6.2.

CD spectroscopy

The CD spectra were recorded using a JASCO J-1500 CD spectrometer (Tokyo, Japan) with 1 mm path length cuvettes at 22℃ in 10 mM potassium phosphate buffer (pH 7.2). Each spectrum represents an integration of three consecutive scans from 190 to 260 nm at 1.0 nm intervals, with a scan speed of 20 nm/ min. Concentration of Hsf1 was 1.5 µM. The helix content was predicted using BeStSel[20].

Simulations

All-atom MD simulations were performed with the CHARMM36m force field[21] using LAMMPS software[20]. In order to investigate the interaction between LZ1-3 (residues: 121-207) and LZ4 (residues: 379-410), the isolated models of Hsf1 LZ1-3 and LZ4 were constructed, in which only LZ1-3 and LZ4 domains were considered in the system and other domains including the disordered regions were excluded. The molecular structures of Hsf1 were estimated by AlphaFold 2 (AF2) [21], and then the estimated structures of the LZ1-3 and LZ4 regions were extracted and used as the initial configurations for the isolated models of Hsf1 LZ1-3 and LZ4. For the LZ4 domain, WT and M391K/L395P/L398R mutant (LZ4m) models of Hsf1 were employed. The isolated models of LZ1-3 and LZ4 were placed in a periodic simulation box and solvated by adding water. The salt concentration was set to 150 mM KCl, and the corresponding numbers of K^+ and Cl^- ions were added. After the steepest-descent energy minimization, the systems were relaxed for 100 ps at a temperature of 285 K and a pressure of 1 atm. Production runs were then performed for 100 ns in the NPT ensemble at 285 K and 1 atm, and the trajectory data was collected every 10 ps. In addition, given an open conformation of Hsf1 at high temperatures, production runs for two independent systems of (i) LZ1-3 only and (ii) LZ4 only were also performed for 150 ns at a temperature of 355 K. The temperature was maintained using a Nosé–Hoover thermostat[22,23] and the pressure was controlled using a Parrinello–Rahman barostat[24,25]. The non-bonded interactions were calculated with a cutoff distance of 1.2 nm, and the particle-particle particle-mesh (PPPM) method[26] was used to calculate long-range electrostatic interactions. The equations of motion were integrated using the Verlet algorithm[27] with a time step of 2 fs, along with the SHAKE algorithm[28], to constrain the bond lengths to hydrogen. For analyses, the distance between the Trp169 and Leu402 residues and the root mean square fluctuations (RMSFs) for each residue were measured for both WT and LZ4m models. The distance between the Cη2 atom of Trp169 and the Cδ1 atom of Leu402 was

calculated for each system using the MD simulation trajectories over 100 ns. The RMSFs of Cα atoms for each residue were calculated with respect to the average structure obtained from the last 20 ns of the trajectories. The root mean square deviations (RMSDs) for Cα atoms were calculated with respect to the starting structure for each system using the MD simulation trajectories over 150 ns. The secondary structure of the protein structures was determined by DSSP[29] to probe the conformational transition over time.

DLS experiments

Dynamic light scattering (DLS) was performed using a Zetasizer Nano ZS (ZEN3600, Malvern Instrument, UK) equipped with a 633 nm red laser and 173° scattering angle. "Size" and "Protein" were selected as the measurement type and the material type, respectively. For each sample, the measurement was repeated 3 times. After the diffusion of a particle moving under Brownian motion was measured, the Zetasizer software version 8.02 converted the diffusion to a size and generated size-intensity distributions using Stokes-Einstein relationship with a refractive index of 1.45 nD and dynamic viscosity of 0.6262 cP. Gaussian fitting was then used to extract the size mean. The analysis was performed with the lower and upper size limits set to 0.4 nm and 10,000 nm, respectively. Hsf1 monomer were prepared in 25 mM HEPES/KOH (pH 7.2) and 150 mM KCl and its concentration was 5 μM. Data were acquired after 30 min incubation at 12℃, 25℃, and 42℃ in the cuvette.

3.3. Results

3.3.1 LZ1-3 and LZ4 in Hsf1 Monomer Forms a Closed Conformation

The three-dimensional structure of Hsf1 has not been determined experimentally, so I first attempted to obtain structural information about the Hsf1 monomer using AlphaFold2 (AF2) and MD simulation[21]. The AF2-predicted structure of the Hsf1 monomer showed that Hsf1 forms "closed" conformation in which LZ1-3 and LZ4 are associated with each other (Figure 3.1B). To evaluate the stability of this predicted structure in closed conformation, we performed MD simulations at 285 K. To assess changes in the interaction between LZ1-3 and LZ4, MD simulations were performed for isolated LZ1-3 (residues: 121-207) and LZ4 (residues: 379-410) whose initial coordinates and positions were estimated by AF2 model (Figure 3.1B). The trajectory of the pair distance between Trp169 Cη2 and Leu402 Cδ1, one of the pairs that are in close proximity in the closed conformation, showed that the distance was stabilized below ~11 Å after ~30 ns of simulation, indicating that LZ1-3 and LZ4 interact with each other to maintain Hsf1 in a closed conformation (Figure 3.1C, E). Next, MD simulations were performed with the M391K/L395P/L398R mutant (LZ4m), a mutant in which oligomerization is promoted by disrupting the hydrophobic interaction between LZ1-3 and LZ4[6,15,16], to predict conformational changes to "open" state during oligomerization. In the simulation for LZ1-3 + LZ4m, the distance between Trp169 Cη2 and Leu402 Cδ1 increased over time and was stabilized at a larger value of ~35 Å after ~40 ns of simulation, resulting in an open conformation (Figure 3.1D, E). Given the previous biochemical studies showing that the M391K/L395P/L398R mutant at LZ4 forms oligomers even at low temperatures[9,17,18], our data from MD simulation suggests that the formation of an open conformation in which LZ1-3 is released from LZ4 can be a key step toward oligomerization. The simulation also showed that fluctuations for each residue were higher in LZ1-3 + LZ4m than in LZ1-3 + LZ4 (Figure 3.1F). Notably, Trp169, one of the

three tryptophan residues (Trp23, Trp37, and Trp169) present in Hsf1, showed a marked increase in fluctuations, suggesting that conformational changes of LZ1-3 and LZ4 can be probed by Trp169.

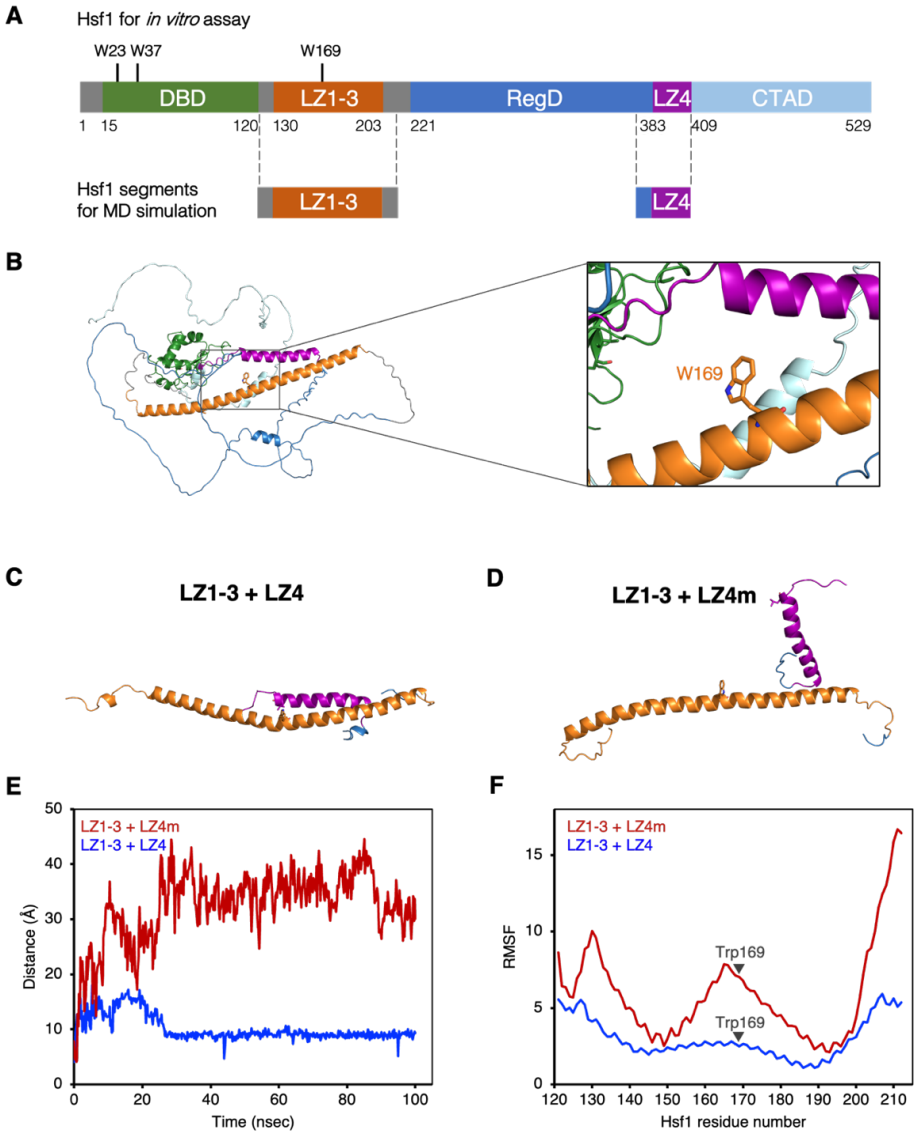

Figure 3.1 Predictive structure of Hsf1 and observation of conformational changes by MD simulation
(A) Domain organization and location of tryptophan residues in Hsf1. The abbreviations used are: DBD, DNA-binding domain, LZ1-3, leucine-zipper domain-1-3, RegD, regulatory domain, LZ4, leucine-zipper domain-4, CTAD, C-terminal transactivation domain. (B) The molecular structure of HSF1 estimated by the AlphaFold2 and closeup view of the structure around Trp169. (C) Structure of the leucine zipper of isolated LZ1-3 (residues: 121-207) and LZ4 (residues: 379-410) after 100 ns MD simulation at 285 K. LZ1-3 and LZ4 remain in the closed conformation facing each other. (D) Structure of the leucine zipper of LZ1-3 + LZ4m after 100 ns MD simulation at 285 K. LZ1-3 and LZ4 changed to open conformation away from each other. (E) The trajectory of the distance between the side chain Cη2 of Trp169 and the side chain Cδ1 of Leu402. (F) Root-mean-square fluctuation (RMSF) of each amino acid of Hsf1 in MD simulation.

3.3.2 Tracking Temperature-dependent Conformational Changes and Oligomerization of Hsf1 by Trp-fluorescence Spectroscopy

To track the conformational transition from monomer to oligomer, I monitored the temperature dependence of tryptophan fluorescence in the monomer of Hsf1 full length (residues: 1-529) (Figure 3.1A). Hsf1 was separated into monomer and oligomer fractions by purification with size-exclusion chromatography, and the monomer fraction was used for fluorescence measurement. Both the wavelength and intensity of the fluorescence peak showed significant changes with temperature change (Figure 3.2A, B). Plot of the peak top wavelength with respect to the temperature showed that the peak top stayed around 327 nm in the temperature range from 12℃ to 27℃, and gradually red-shifted toward 337 nm in the temperature range from 27℃ to 42℃. The fluorescence spectra of Hsf1 monomer and oligomer showed that the maximum wavelength of the oligomer was red-shifted from that of the monomer (Figure 3.2C). The wavelength of the oligomer fraction was 338.5 nm which is close to the fluorescence maximum wavelength at 42–57℃ (Figure 3.2A, B), implying that the red-shift coincides with Hsf1 oligomerization. The red shift of the fluorescence peak generally reflects an environmental change toward hydrophilic conditions[30]. This is consistent with the AF2 predicted structure, in which Trp169 of Hsf1 forms a hydrophobic cavity in the monomer while it is exposed to the solvent in the oligomer (Figure 3.2D, E). The oligomeric state of Hsf1 at each temperature was evaluated by SEC-MALS, dynamic light scattering (DLS) and 1D ^{1}H-NMR experiments (Figure 3A-D). SEC-MALS showed that Hsf1 stays mostly monomer at room temperature and up to 27℃, whereas forms oligomers after heat shock at 42℃ (Figure 3.3A, B). In the DLS experiments, the radius of Hsf1 was estimated to be 12~13 nm at 12℃ and 25℃, while the radius increased to 26 nm at 42℃, indicating the formation of oligomers at the elevated temperature (Figure 3.3C). Formation of Hsf1 oligomers at 42℃ was further corroborated by 1D ^{1}H-NMR experiments in which the intensity of Hsf1 resonances decreased as the temperature increased (Figure 3.3D).

Decreased resonance intensity at higher temperature can be explained by line broadening owing to oligomerization that causes slower tumbling. Collectively, these results showed that Hsf1 exists as mostly monomer at 12℃ and 25℃, and forms oligomer at 42℃, which is consistent with previous studies showing that Hsf1 oligomerizes around 42℃[2,7,8]. Therefore, I concluded that the red-shifted Trp fluorescence at higher temperature reflects Hsf1 oligomerization.

Next, temperature-dependent changes in the Trp fluorescence intensity at maxima were evaluated to track the conformational changes of Hsf1 (Figure 3.2B). Note that the fluorescence intensity reflects the local mobility of the Trp residues. The fluorescence intensity decreased from 12℃ to 27℃, and increased from 27℃ to 52℃ (Figure 3.2A, B). Considering the intensity of the fluorescence maxima was higher for the oligomer than for the monomer (Figure 3.2C), an increase in the fluorescence intensity in the spectrum above 27℃ can be attributed to oligomerization. On the contrary, the fluorescence intensity decreased as the temperature increased from 12℃ to 27℃ (Figure 3.2A, B). Such biphasic changes in the fluorescence intensity are characteristic of state changes through intermediates and indicates the existence of intermediates in response to heat. Note that this biphasic transition of Trp fluorescence was not seen in the control experiment using the immunoglobulin binding domain of protein G (GB1) that is known to be stable even at high temperatures and has one Trp residue fixed in the core of the protein (Figure 3.4A). Although the fluorescence intensity of GB1 slightly decreased as the temperature increased, the intensity change in GB1 spectra was much less significant than in Hsf1 spectra (Figure 3.4B, C). Furthermore, the peak top wavelength of GB1 Trp fluorescence spectra remained almost unchanged even at high temperature (Figure 3.4B, D).

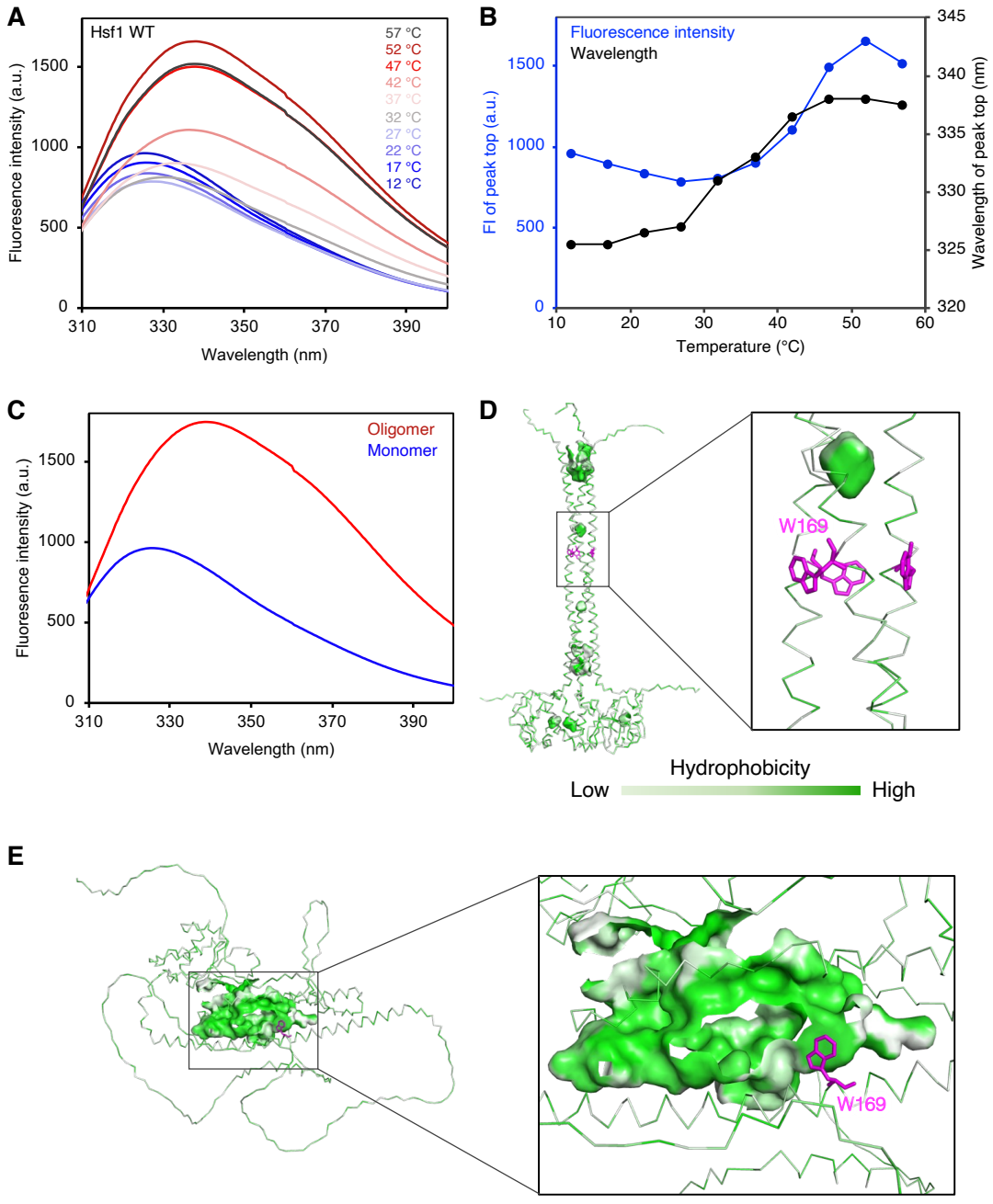

Figure 3.2 Monitoring conformational changes and oligomerization of Hsf1 by observing Trp fluorescence

(A) Trp fluorescence spectra of Hsf1 monomer at varying temperatures from 12℃ to 57℃. (B) Transition of fluorescence intensity (FI) and wavelength at the peak top in the temperature change measurement. (C) Fluorescence spectra of Hsf1 monomer (blue) and oligomer (red) at 12℃. (D-E) Hydrophobic cavities of Hsf1 trimer (D) and monomer (E) and its closeup view around Trp169. The structure of Hsf1 is the AlphaFold2 predictive structure, and only DBD - LZ1-3 is shown for the trimers. Hydrophobic cavities estimated by pymol are shown as green surfaces.

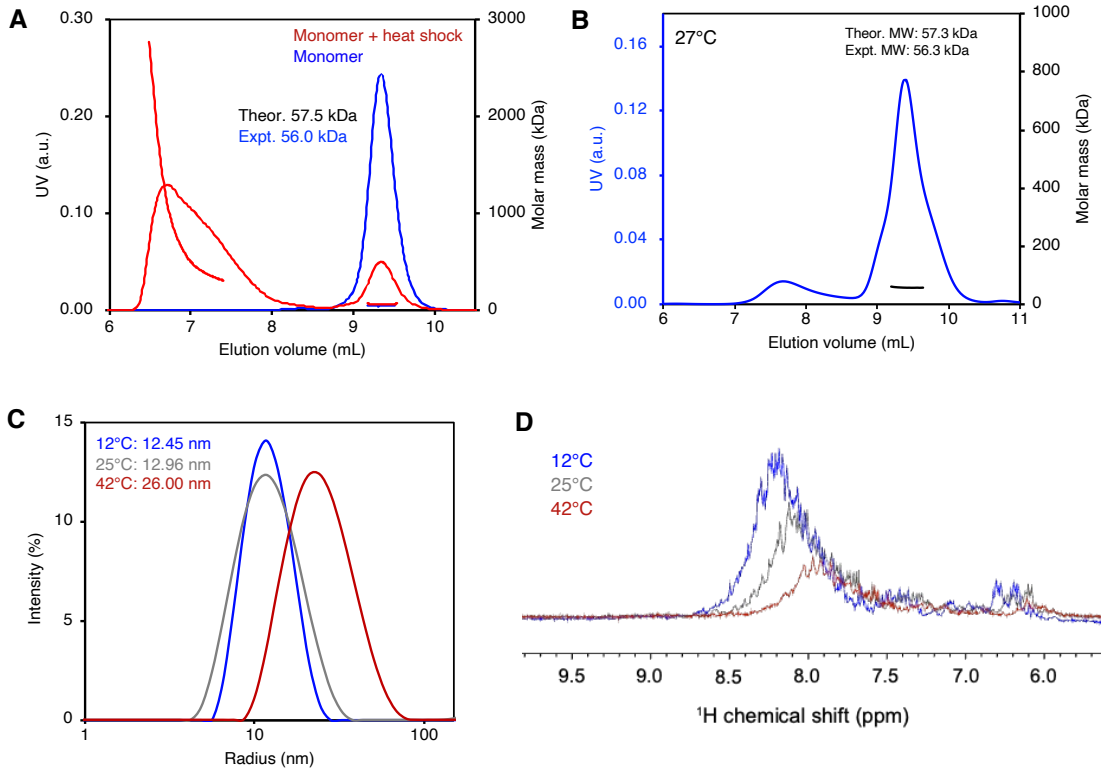

Figure 3.3 Heat-induced oligomerization of Hsf1
(A) SEC-MALS of Hsf1 monomer at 12°C (blue) and after heat shock at 42°C (red). (B) SEC-MALS of Hsf1 monomer at 27°C (blue) and after heat shock at 42°C (red). (C) DLS analysis of Hsf1 monomer at 12°C (blue), 25°C (gray), and 42°C (red). (D) ^{1}H NMR spectra of Hsf1 monomer at 12°C (blue), 25°C (gray), and 42°C (red).

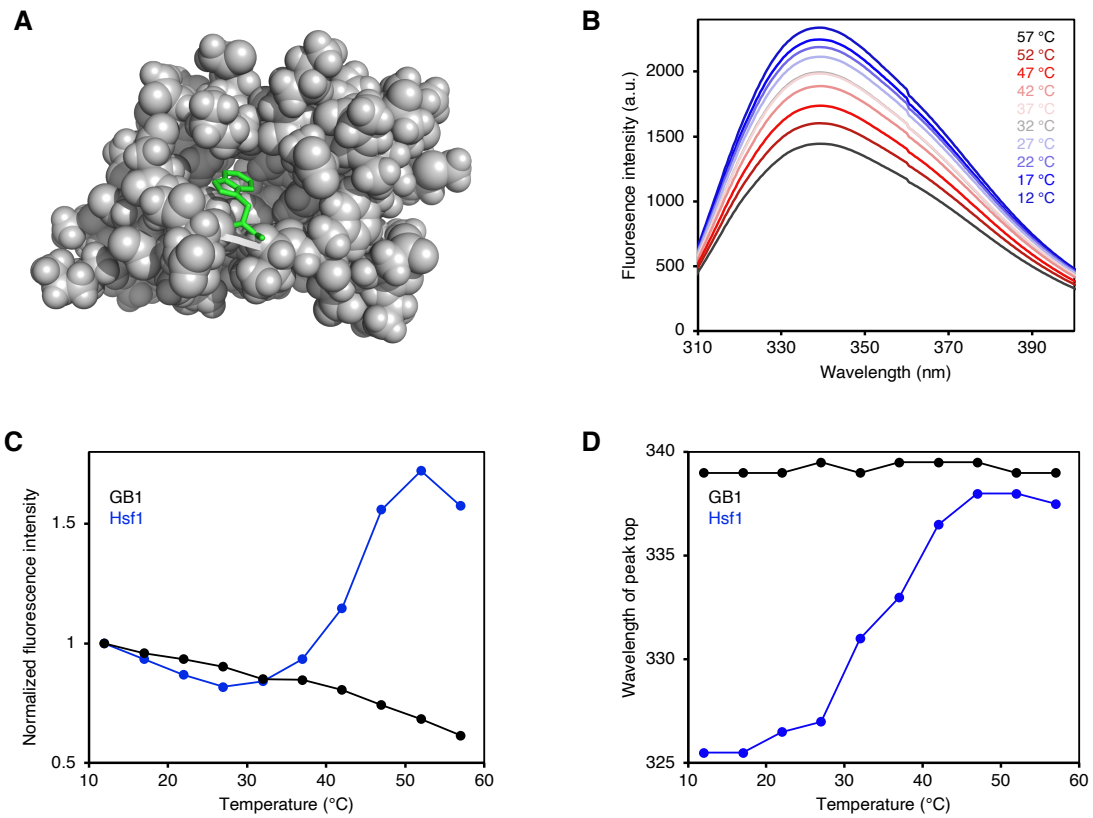

Figure 3.4 Temperature-dependent changes of Trp fluorescence of GB1
(A) The structure of GB1 (PDB ID: 1GB1). Trp residue is represented as green sticks, and other residues are represented as gray spheres. (B) Trp fluorescence spectra of GB1 at varying temperatures from 12℃ to 57℃. (C) Normalized fluorescence intensity of GB1 and Hsf1 at various temperatures. The intensity change of Hsf1 is more significant than that of GB1, indicating the temperature-dependent structural change around tryptophans of Hsf1. (D) The wavelength at the peak top of GB1 and Hsf1 in the temperature change measurement.

3.3.3 Characterization of Intermediate Monomeric State by Model Fitting Analysis

To investigate the transition mechanism from the monomeric closed state to the oligomeric state, I structurally characterized the intermediate state of Hsf1 by analyzing the fluorescence spectral data using a mathematical model and global fitting simulation. Singular value decomposition analysis of the fluorescence spectra suggested that at least three components were present (Figure 3.5A, B). The mathematical model assumes that Hsf1 has three states: the initial monomeric state (M), monomeric intermediate state (I), and oligomeric state (O). This model can be written as

$$M \leftrightarrow I \leftrightarrow O$$

Figure 3.5C shows the experimental plot and fitting curve of the temperature dependence of fluorescence peak intensity. The fitting curve reproduced the experimental results well, indicating that the three-state model explained the experimental data well. The fitting analysis provided the population fractions of the three states and revealed that the major population fractions of Hsf1 transitioned from the M state to the I state around 20℃ and from the I state to the O state around 40℃ (Figure 3.5D). This is consistent with the results from SEC-MALS and DLS showing that a majority of Hsf1 became oligomeric at 42ºC (Figure 3.3A, B), and also suggests that the I state can be a major conformation at approximately 37℃, the normal intracellular temperature. To obtain structural information on the intermediate state, we computed the component spectra of Hsf1 in the three states (Figure 3.5E). The computed spectra of Hsf1 in the M and O states exhibited a peak fluorescence at 324.5 and 338.5 nm, respectively. These computed fluorescence spectra corresponded well with those obtained experimentally for the monomer and oligomer Hsf1 (Figure 3.5E). Interestingly, Hsf1 in the I state showed a peak fluorescence at 331.5 nm, indicating that the peak position of the fluorescence spectrum in the I state was red-shifted from that in the M state. Furthermore, the peak intensity in the I state was weaker than that in the M state. The peak red-shift and intensity reduction in the tryptophan fluorescence spectrum of the I state can be interpreted as solvent exposure and increased mobility of tryptophan residues, respectively[30].

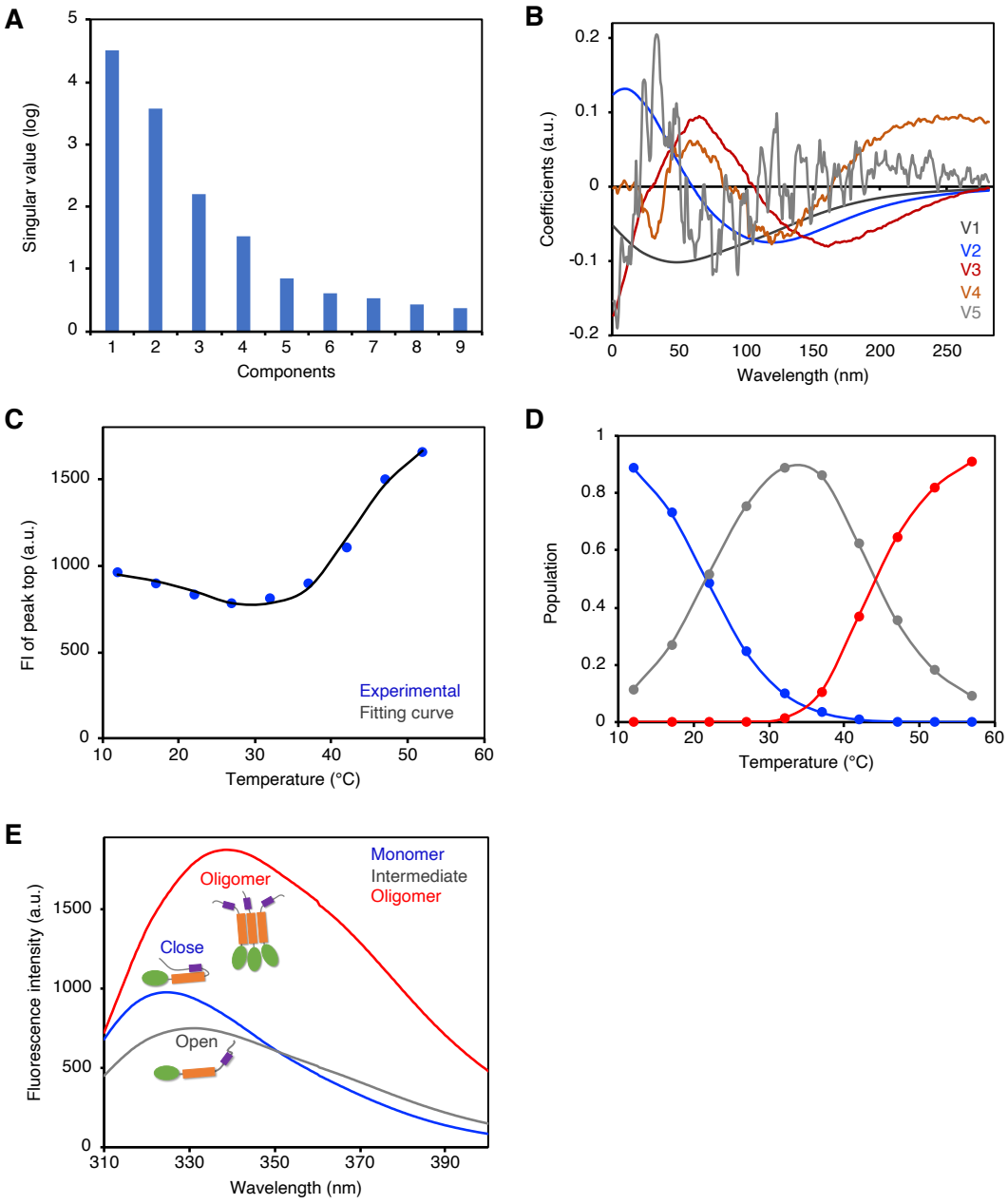

Figure 3.5 Model fitting analysis of Trp fluorescence measurement
(A) Singular values by the SVD analysis. The data matrix D is decomposed into three matrices as follows: D = USVT, where U and V are the orthogonal matrices and S is the diagonal matrix containing the singular values on its diagonal. (B) The first five rows by the SVD analysis. The fifth row of the U matrix showed a random spectrum. These data suggest that at least three components are necessary to construct the fluorescence spectral dataset within a noise level. (C) The experimental plot and fitting curve of the temperature dependence of fluorescence peak intensity. (D) The populational fractions of the three states from the fitting analysis. (E) The computed component spectra of Hsf1 in the three states.

Model fitting analysis showed that the tryptophan residues in the I state have increased mobility compared to those in the M state. Given that MD simulation showed that the fluctuation of Trp169 increased when the interaction between LZ1-3 and LZ4 was resolved to an open conformation (Figure 3.1F), it is suggested that Hsf1 in the I state can form an open conformation. To confirm whether the I state reflects the open conformation of LZ1-3 and LZ4, I selectively observed fluorescence from Trp169 in LZ1-3 by substitution of Trp23 and Trp37 with phenylalanine in the DNA-binding domain. As a result, the fluorescence intensity became minimal at 27°C, which coincided with the intensity change of Hsf1 WT (Figure 3.6A, B). Therefore, the decrease in fluorescence intensity was due to the increased mobility of Trp169 located in LZ1-3. Focusing on the wavelength of the fluorescence maxima of the Hsf1 W23F/W37F mutant, a red-shift was observed in the region from 12°C to 27°C (Figure 3.6A, B). Because LZ4 is an amphiphilic helix and its hydrophobic side faces LZ1-3 in the structural prediction of LZ4 by Netwheels and AF2[21,31] (Figure 3.6C, D), it is suggested that this red-shift reflects a weakening of the hydrophobic interaction between LZ1-3 and LZ4. Note that SEC-MALS and DLS results showed Hsf1 was mostly present as a monomer around 27°C (Figure 3.3A, B), suggesting that the intermediate should be in a monomeric state. Therefore, Trp fluorescence measurements and model fitting analysis demonstrated that the monomeric intermediate has an open conformation in which the interaction between LZ1-3 and LZ4 is dissolved.

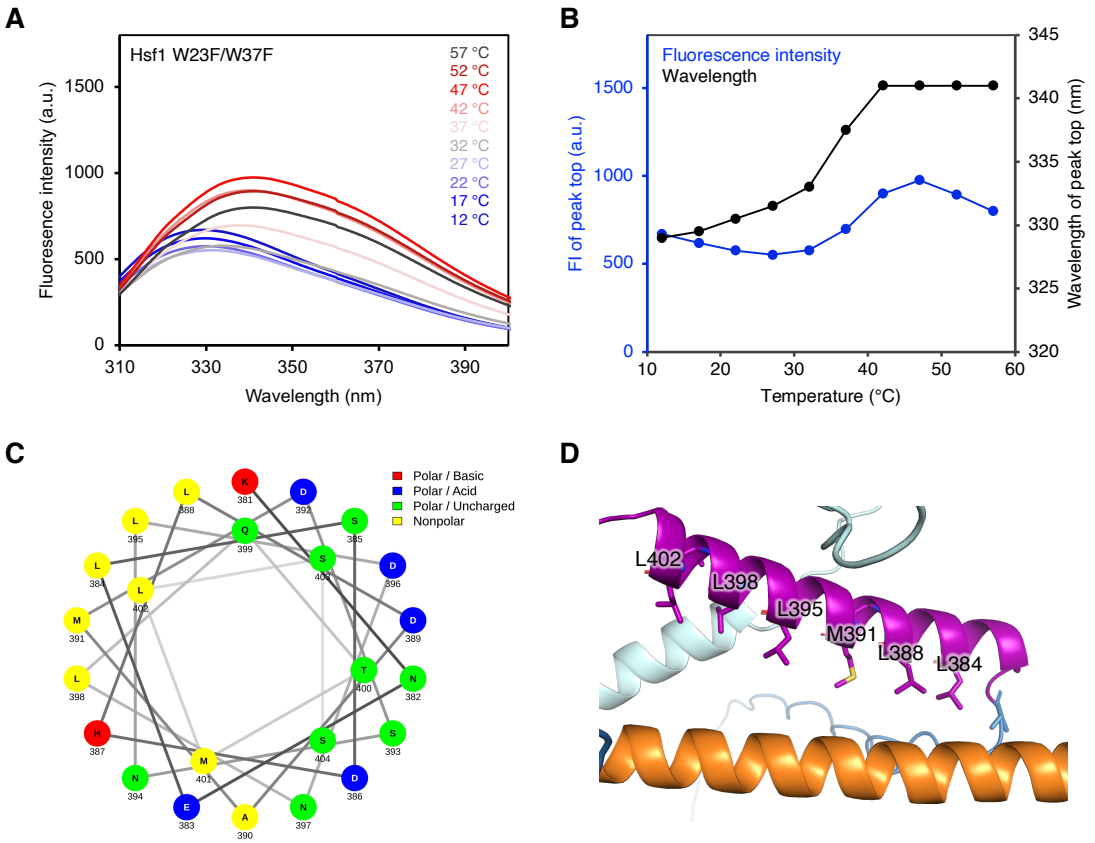

Figure 3.6 Monitoring the Trp169 fluorescence of Hsf1
(A) Trp fluorescence spectra of Hsf1 W23F/W37F at varying temperatures from 12°C to 57°C. (B) Transition of fluorescence intensity and wavelength at the peak top in the temperature change measurement. (C) Helical wheel and net projections created using NetWheels. (D) The closeup view of the structure around LZ1-3 (orange) and LZ4 (magenta) estimated by the AlphaFold2.

3.3.4 Tracking the Temperature-dependent Dissolution of the Hydrophobic Cavity of Hsf1

To confirm the open conformation between LZ1-3 and LZ4 in Hsf1 at elevated temperatures, the hydrophobic cavity formed between LZ1-3 and LZ4 was evaluated by fluorescence measurements of ANS, a compound whose fluorescence maxima increased significantly and its wavelength blue-shifted under hydrophobic conditions compared to that in aqueous solution[32]. Trp fluorescence measurements suggested that at lower temperatures, the interaction between LZ1-3 and LZ4 in the closed conformation forms a hydrophobic cavity (Figure 3.2, 3.4, and 3.5), whereas at higher temperatures, the

transition toward the open conformation disrupts the hydrophobic cavity and is thus expected to alter ANS fluorescence properties. ANS was added to the Hsf1 monomer and temperature-dependent changes in ANS fluorescence were monitored. Because the affinity between ANS and the target protein decreased in a temperature-dependent manner[33], it was difficult to evaluate the conformational change of Hsf1 with the disruption of hydrophobic cavities from the linear decrease in ANS-derived fluorescence intensity in the temperature range from 12℃ to 37℃ (Figure 3.7A, B). On the contrary, change in the fluorescence maximum wavelength showed a biphasic profile in which the fluorescence maxima red-shifted in the temperature region from 12℃ to 27℃, but blue shifted in the temperature region from 27℃ to 52℃ (Figure 3.7A, B), suggesting that ANS fluorescence wavelength reflects information about the intermediate. Note that the inflection point around 27℃ roughly coincides with that observed in the Trp fluorescence analysis (Figure 3.2B). The red-shift of ANS fluorescence suggested that the environment of the ANS binding site on Hsf1 became gradually hydrophilic, suggesting that the hydrophobic cavity, most probably the cavity formed between LZ1-3 and LZ4, of Hsf1 was disrupted at 27℃. In the temperature region from 27℃ to 52℃, the fluorescence maximum wavelength was blue-shifted (Figure 3.7A, B). Thus, changes in the high-temperature region may be due to the binding of ANS to the newly formed hydrophobic cavities by oligomerization (Figure 3.2D). Notably, ANS-derived fluorescence at 12℃ was 145 a.u. at 470.5 nm for Hsf1 full length and 9 a.u. at 491.5 nm for the isolated Hsf1 DBD (Figure 3.8A, B), suggesting that ANS barely interacts with DBD. This indicates that the changes in ANS fluorescence reflect the conformational changes in the C-terminal region, including LZ1-3 and LZ4 in full-length Hsf1.

To determine whether the temperature-dependent changes in ANS-derived fluorescence reflect the conformational change between LZ1-3 and LZ4, we investigated the binding site of ANS for Hsf1 by ^{19}F NMR for [5-^{19}F-Trp] Hsf1, in which three Trp residues (Trp23, Trp37, and Trp169) were substituted by 5-^{19}F-Trp. Three ^{19}F NMR

signals were observed, indicating that each of the three tryptophan residues in Hsf1 (Trp23, Trp37, and Trp169) exhibited a single signal (Figure 3.7C). To assign the resonances, ^{19}F NMR was performed for Hsf1 DBD containing Trp23, Trp37, and Hsf1 ΔDBD containing Trp169. Two ^{19}F NMR signals for Hsf1 DBD were observed at -123.2 ppm and -124.6 ppm, and only one ^{19}F NMR signal for Hsf1 ΔDBD was observed at -125.3 ppm (Figure 3.7C). Therefore, the ^{19}F NMR signal at -125.3 ppm was assigned to the Trp169-derived signal located in the LZ1-3 region. This ^{19}F NMR signal of Trp169 showed chemical shift perturbation by the addition of 1 equivalent of ANS (Figure 3.7C), showing that ANS interacts with Trp169 located in the hydrophobic cavity.

To further support ANS binding to the hydrophobic cavity, Trp-ANS fluorescence resonance energy transfer (FRET) was performed. When a mixed sample of Hsf1 and ANS was excited at 295 nm, near the Trp excitation wavelength at 12°C, ANS fluorescence was observed, indicating ANS binding around the Trp of Hsf1 (Figure 3.7D). Trp-ANS FRET was not observed in the mixed samples of DBD and ANS (Figure 3.7D, 3.8). These ^{19}F-Trp NMR and FRET analyses showed that ANS binds to the hydrophobic cavity formed between LZ1-3 and LZ4 in a closed conformation. Thus, monitoring the dissolution of the hydrophobic cavity by ANS fluorescence also supports that the Hsf1 intermediate is in an open conformation in which LZ1-3 and LZ4 are dissociated.

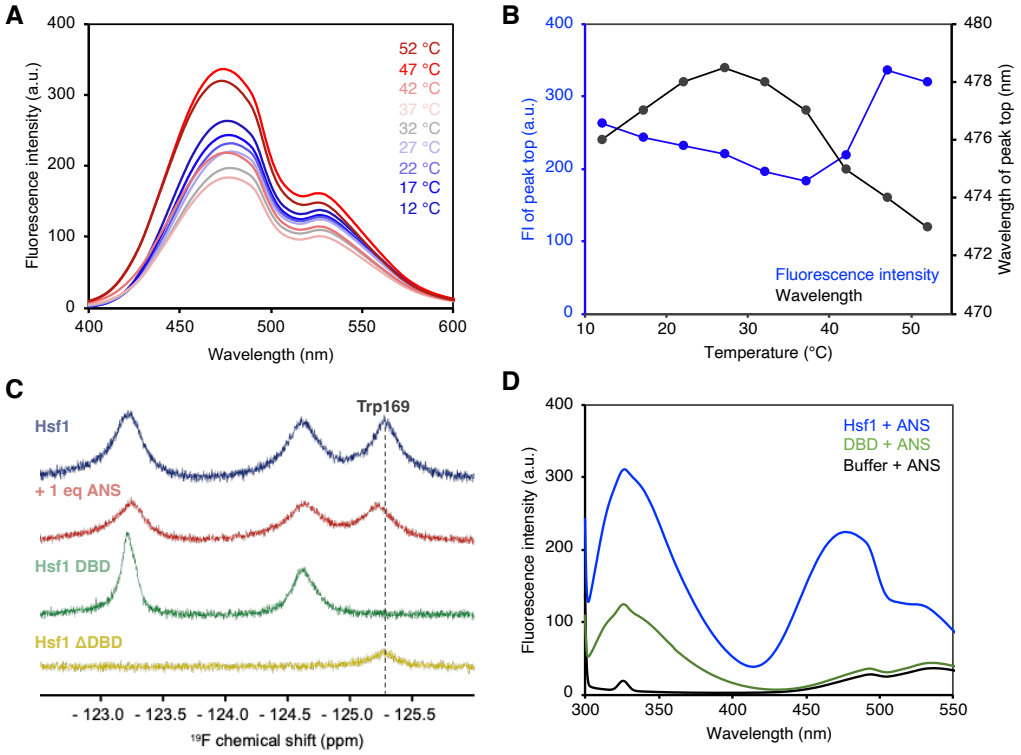

Figure 3.7 Tracking the collapse of the hydrophobic cavity of Hsf1 by ANS fluorescence measurements

(A) ANS fluorescence spectra mixed with Hsf1 at varying temperatures from 12°C to 52°C. (B) Transition of fluorescence intensity and wavelength at the peak top in the temperature change measurement. (C) 19F NMR spectra of 5-19F-Trp labelled Hsf1 monomer (blue), Hsf1 monomer + 1 equivalent ANS (red), Hsf1 DBD (green), and Hsf1 deltaDBD (ΔDBD) (yellow) at 12°C. The signal from Trp169 was assigned from comparison of spectra of Hsf1, Hsf1 DBD, and Hsf1 ΔDBD. (D) Upon tryptophan excitation at 295 nm, FRET between ANS and Hsf1 is characterized by the apparition of a signal at 475 nm (blue). Spectra of mixed samples of Hsf1 DBD and ANS under the same conditions (green). Emission spectra of ANS alone are colored in black. Since FRET was observed only in Hsf1, it was indicated that ANS binds to the hydrophobic cavity formed between LZ1-3 and LZ4 in Hsf1.

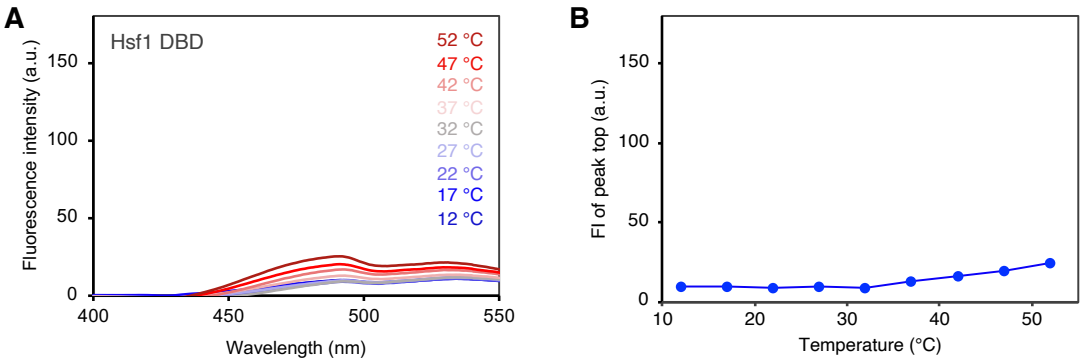

Figure 3.8 ANS fluorescence with DBD

(A) ANS fluorescence spectra mixed with DBD at varying temperatures from 12°C to 52°C. (B) The transition of fluorescence intensity at the peak top in the temperature change measurement.

3.3.5 Secondary Structure in the Formation of the Intermediate

Our results show that Hsf1 forms a monomeric open state in which LZ1-3 and LZ4 are dissociated at higher temperature and thus suggest that the helical structures of leucine zippers can be destabilized in the open conformation. To investigate the secondary structure of Hsf1 in the monomeric open conformation, we measured CD spectroscopy at varying temperatures. Measurements of CD spectra of Hsf1 at 12ºC showed a minimum ellipticity at 207 nm, characteristic of a protein with a high α-helical content (Figure 3.9A). The α-helical content calculated from this CD spectrum using the BeStSel program[18] was 27.2%, which was in good agreement with the α-helical content of 28.4% calculated from the AF2 predictive structure (Figure 3.9A, C, E). The negative ellipticity in the region from 205 to 230 nm decreased and α-helical contents were perturbed from 27.2% at 12ºC to 19.6% at 52ºC as temperature increased (Figure 3.9A-C, E), indicating the unfolding of the helical structure at elevated temperatures. The CD spectra of LZ4 alone showed a minimum ellipticity at 201 nm and the α-helical content calculated to be only 1.1 % (Figure 3.9D, E), showing the isolated LZ4 is mostly unfolded. The data indicate that the helical structures of LZ1-3 and LZ4 are stabilized at closed conformation, but LZ4 unfolds without support from LZ1-3 at open conformation and oligomeric state.

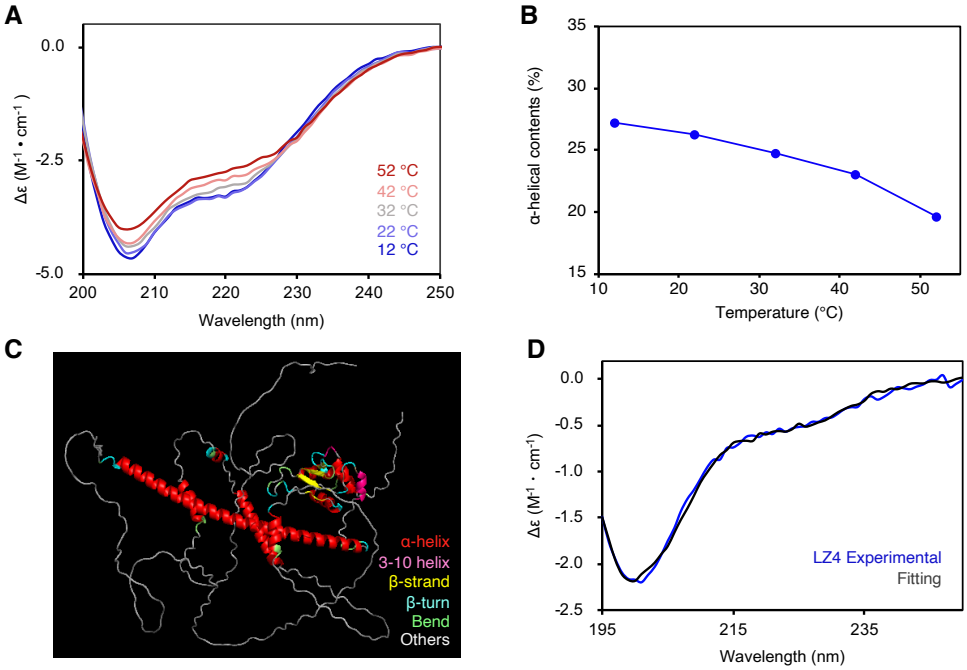

E

	12 °C	22 °C	32 °C	42 °C	52 °C	AF2	LZ4
α-Helix (%)	27.2	26.3	24.7	23.0	19.6	28.4	1.1
β-strand (%)	12.5	16.4	15.2	17.7	19.5	2.7	34.3
Turn (%)	13.1	12.3	13.5	14.3	14.2	4.0	17.6
Others (%)	47.2	45.0	46.5	45.0	46.7	65.0	47.0

Figure 3.9 Temperature-dependent secondary structural change
(A) CD spectra of Hsf1 at varying temperatures from 12°C to 52°C. (B) The α-helical contents (%) calculated using BeStSel dependence on temperature change. (C) Secondary structure mapping to the molecular structure of Hsf1 estimated by AlphaFold2. (D) CD spectra of Hsf1 LZ4 at 12°C. (E) The result of the secondary structure estimation.

Given the temperature-dependent structural changes of the leucine zipper domains as shown by Trp fluorescence (Figure 3.2), the temperature-dependent secondary structure change of Hsf1 can be attributed to the LZ1-3 and LZ4. To investigate the structural change of LZ1-3 and LZ4 in the open conformation, MD simulations were performed for each of the isolated LZ1-3 and LZ4 at 355 K. The trajectory of RMSD from the initial structure showed that the RMSD of LZ1-3 was around 1 ~ 2 nm (Figure 3.10A, E), and that of LZ4 linearly increased (Figure 3.11A, C). On the other hand, in MD simulations for LZ1-3 + LZ4 at 285 K, in which LZ1-3 and LZ4 existed in the closed conformation, both LZ1-3 and LZ4 showed smaller RMSD, indicating that LZ1-3 and LZ4 are stabilized in the closed form. Tracking of the helix contents showed that the helix content in the isolated LZ1-3 and LZ4 gradually decreased over time (Figure 3.10B, 3.11B, D). Thus, the data from MD simulations support the idea that LZ1-3 and LZ4 are destabilized and undergo unfolding in the open conformation at higher temperature. Note that LZ4 can be more prone to unfolding, as suggested by the more significant decrease in the helix contents (Figure 3.11). Therefore, CD measurements and MD simulation showed that the intermediate in the transition from the Hsf1 monomer to the oligomer at elevated temperature is coupled with the unfolding of the LZ1-3 and LZ4 helices and the weakening of the intramolecular interactions.

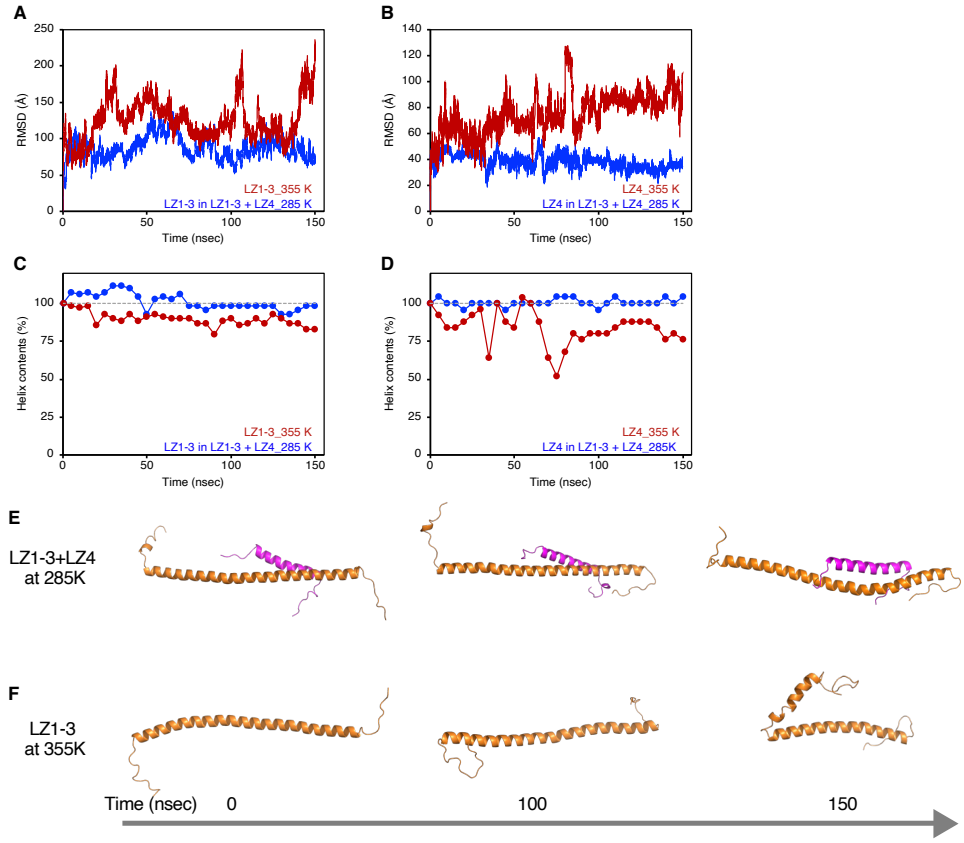

Figure 3.10 LZ unfolding tracked by MD simulation
(A, B) Root-mean-square deviation (RMSD) between the initial structure and the structure at each time in MD simulation of LZ1-3 (A) and LZ4 (B). (C, D) Helix contents at each time in MD simulation of LZ1-3 (C) and LZ4 (D). (E, F) Snapshots structure of LZ1-3+LZ4 at 285 K (E) and LZ1-3 at 355 K (F) in MD simulation.

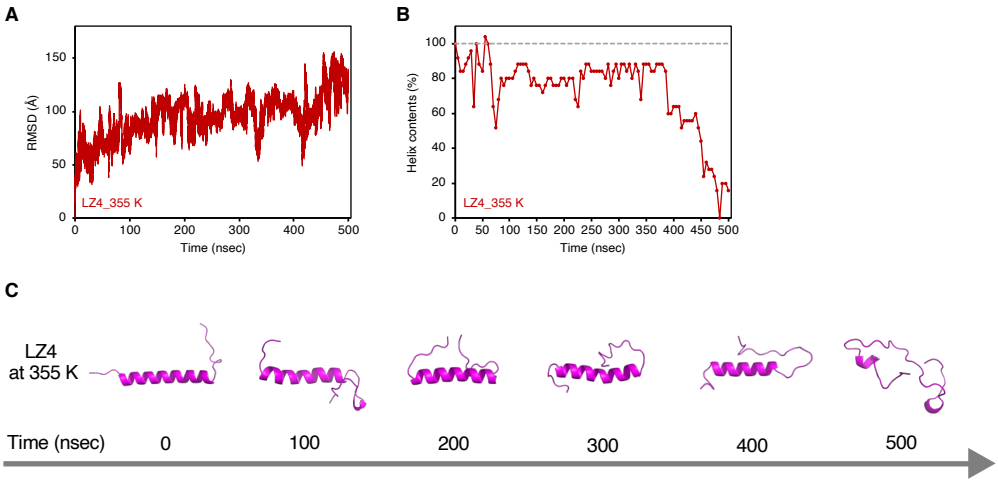

Figure 3.11 LZ4 unfolding tracked by MD simulation
(A) Root-mean-square deviation (RMSD) between the initial structure and the structure at each time in MD simulation of LZ4. (B) Helix contents at each time in MD simulation of LZ4. Snapshots of the structure of LZ4 at 355 K in MD simulation. (C) Snapshots structure of LZ4 at 355 K in MD simulation.

3.4. Discussion

Hsf1 oligomerization is a key event during stress response, however, insight into how Hsf1 transitions from monomer to oligomer is limited because of the lack of studies monitoring the three-dimensional conformational changes of Hsf1. In this study, I aimed to elucidate the mechanism of the heat-induced conformational transition and oligomerization of Hsf1. Trp fluorescence measurements revealed that Hsf1 oligomerizes through an intermediate (Figure 3.2A, B, 3.6A, B), and its model fitting, ANS fluorescence measurements, SEC-MALS, DLS, and MD simulations revealed that the intermediate is a monomeric open conformation in which the interaction between LZ1-3 and LZ4 was resolved (Figure 3.1C-E, 3.3A, B, 3.4, and 3.7A, B). Furthermore, the CD experiments and MD simulations showed that the weakening of the interaction between LZ1-3 and LZ4 was coupled with the unfolding of the helical structure (Figure 3.9, 3.10, and 3.11). Especially, LZ4 was found to be prone to unfolding (Figure 3.11). These data are consistent with the previous study using hydrogen/deuterium-exchange mass spectrometry showing destabilization of LZ4 at elevated temperatures[7]. Therefore, the data suggest that heat-induced unfolding of LZ4 occurs in conjunction with the tertiary structural change from the closed to open conformation of Hsf1 (Figure 3.12).

Trp and ANS fluorescence at different temperatures showed that Hsf1 exists in an open conformational intermediate at the temperature range between 30℃ and 40℃ (Figure 3.4 and 3.7). Although intracellular crowding environment and other regulatory factors may have an influence[34], the monomeric open conformation may be the major conformation at normal cell temperature[37]. Such an open conformation of the Hsf1 monomer, which exposes the sites involved in oligomerization, may allow the rapid formation of the active oligomer under stress5 Hsf1 is known to form a complex with several molecular chaperones[2–5], and the proposed sites for interaction with Hsp70, Hsp90, and TRiC are located in regions LZ1-3 and RegD[2,5,36]. Moreover, it is also suggested that the nuclear localization signal, which is recognized by nuclear transporters, is located

immediately after LZ1-3 (residues:203-230)[16]. The locations of chaperone-binding sites and nuclear-localization signals around LZ1-3 imply the importance of the open-close conformational change of Hsf1 mediated by the contact between LZ1-3 and LZ4 for the regulation of interaction with other molecules (Figure 3.12). Interestingly, the previous cell-based study showed that Hsf1 mutant disrupting the interaction between LZ1-3 and LZ4 accumulates in the nucleus [6], highlighting the possible relationship between Hsf1 open-close conformational state and recognition by the regulators. Thus, the conformational regulation of Hsf1 by molecular chaperones, in addition to the intramolecular leucine zipper interactions to maintain the open monomeric state as the major fraction, can be advantageous in stress responses such as oligomerization and nuclear transport when cells are under stress. Our findings show that Hsf1 oligomerizes through a monomeric open intermediate. Furthermore, this monomeric open state is not just an intermediate in oligomerization but can be a major conformational state in the intracellular environment and a key to understanding the regulation of Hsf1-mediated stress response through interactions with multiple cellular components.

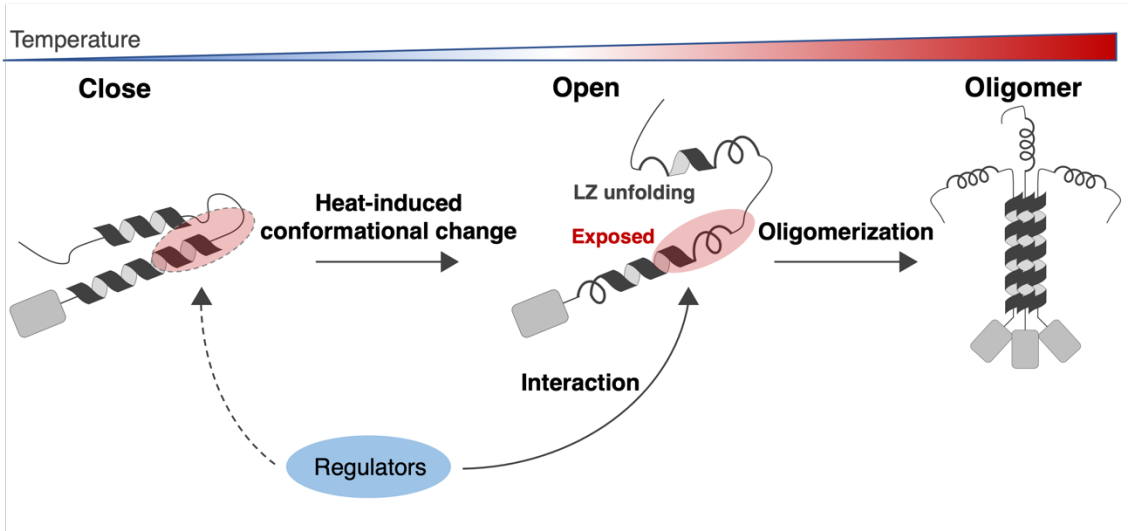

Figure 3.12 Proposed model of the Hsf1 open/close conformational change
Hsf1 oligomerizes through a monomeric open state by sensing heat. The conformational change from close to open state occurs in conjunction with the unfolding of LZ4. The proposed interaction with Hsp70, Hsp90 and TRiC and nuclear localization signal sequence are located in the regions LZ1-3 and RegD (red circle). The interaction of Hsf1 with these regulators may be modulated by the close and open conformational changes of Hsf1, and it is speculated that they selectively interact with Hsf1 in open conformation where their recognition sites are exposed.

References

1. Anckar, J., Sistonen, L. Regulation of HSF1 Function in the Heat Stress Response: Implications in Aging and Disease. *Annu. Rev. Biochem.* **80**, 1089–1115. (2011).
2. Kmiecik, S. W., le Breton, L., Mayer, M. P. Feedback Regulation of Heat Shock Factor 1 (Hsf1) Activity by Hsp70-mediated Trimer Unzipping and Dissociation from DNA. *EMBO J.* **39**, e104096 (2020).
3. Yanhong Shi, Dick D. Mosser, and R. I. M. *Molecularchaperones as HSF1-specific transcriptional repressors*. *Genes Dev.* **12**, 654-66(1998).
4. Zou, J., Guo, Y., Guettouche, T., Smith, D. F., Voellmy, R. Repression of Heat Shock Transcription Factor HSF1 Activation by HSP90 (HSP90 Complex) That Forms a Stress-Sensitive Complex with HSF1. *Cell* **94**, 471–480 (1998).
5. Neef, D. W., Jaeger, A. M., Gomez-Pastor, R., Willmund, F., Frydman, J., Thiele, D. J. A. Direct Regulatory Interaction between Chaperonin TRiC and Stress-Responsive Transcription Factor HSF1. *Cell Rep.* **9**, 955–966. (2014).
6. Rabindran, S. K., Haroun, R. I., Clos, J., Wisniewski, J., Wu, C. Regulation of Heat Shock Factor Trimer Formation: Role of a Conserved Leucine Zipper. *Science* **259**, 230–234 (1993).
7. Hentze, N., le Breton, L., Wiesner, J., Kempf, G., Mayer, M. P. Molecular Mechanism of Thermosensory Function of Human Heat Shock Transcription Factor Hsf1. *Elife* **5**, e11576 (2016).
8. Zhong, M., Orosz, A., Wu, C. Direct Sensing of Heat and Oxidation by Drosophila Heat Shock Transcription Factor. *Mol Cell* **2**, 101–108 (1998).
9. Sarge, K. D., Murphy, S. P., Morimoto, R. I. Activation of Heat Shock Gene Transcription by Heat Shock Factor 1 Involves Oligomerization, Acquisition of DNA-Binding Activity, and Nuclear Localization and Can Occur in the Absence of Stress. *Mol. Cell Biol.* **13**, 1392–1407. (1993).
10. Zuo, J., Baler, R., Dahl, G., Voellmy, R. Activation of the DNA-Binding Ability of Human Heat Shock Transcription Factor 1 May Involve the Transition from an Intramolecular to an Intermolecular Triple-Stranded Coiled-Coil Structure. *Mol. Cell Biol.* **14**, 7557–7568 (1994).
11. Westwoodt, J. T., Wu, C. Activation of Drosophila Heat Shock Factor: Conformational Change Associated with a Monomer-to-Trimer Transition. *Mol. Cell Biol.* **13**, 3481–3486 (1993).
12. Neudegger, T., Verghese, J., Hayer-Hartl, M., Hartl, F. U., Bracher, A. Structure of Human Heat-Shock Transcription Factor 1 in Complex with DNA. *Nat. Struct. Mol. Biol.* **23**, 140–146 (2016).
13. Feng, N., Feng, H., Wang, S., Punekar, A. S., Ladenstein, R., Wang, D. C., Zhang, Q., Ding, J., Liu, W. Structures of Heat Shock Factor Trimers Bound to DNA. *iScience* **24**, 102951 (2021).
14. Littlefield, O., Nelson, H. C. M. A New Use for the "wing" of the "Winged" Helix-Turn-Helix Motif in the HSF–DNA Cocrystal. *Nat. Struct. Biol.* **6**, 464–470 (1999).
15. Jaeger, A. M., Makley, L. N., Gestwicki, J. E., Thiele, D. J. Genomic Heat Shock Element Sequences Drive Cooperative Human Heat Shock Factor 1 DNA Binding and Selectivity. *J. Biol. Chem.* **289**, 30459–30469 (2014).
16. Neef, D. W., Jaeger, A. M., Thiele, D. J. Genetic Selection for Constitutively Trimerized Human Hsf1 Mutants Identifies a Role for Coiled-Coil Motifs in DNA Binding. *G3: Genes, Genomes, Genetics* **3**, 1315–1324 (2013).
17. Shashilov, V. A., Lednev, I. K. Advanced Statistical and Numerical Methods for Spectroscopic Characterization of Protein Structural Evolution. *Chem. Rev.* **110**, 5692–5713 (2010).
18. Micsonai, A., Wien, F., Kernya, L., Lee, Y. H., Goto, Y., Réfrégiers, M., Kardos, J.

Accurate Secondary Structure Prediction and Fold Recognition for Circular Dichroism Spectroscopy. *Proc. Natl. Acad. Sci. U S A* **112**, E3095–E3103 (2015).
19. Huang, J., Rauscher, S., Nawrocki, G., Ran, T., Feig, M., de Groot, B. L., Grubmüller, H., MacKerell, A. D. CHARMM36m: An Improved Force Field for Folded and Intrinsically Disordered Proteins. *Nat. Methods* **14**, 71–73 (2016).
20. Plimpton, S. Fast Parallel Algorithms for Short-Range Molecular Dynamics. *J. Comput. Phys.* **117**, 1–19 (1995).
21. Jumper, J. *et al*. Highly Accurate Protein Structure Prediction with AlphaFold. *Nature* **596**, 583–589 (2021).
22. Nosé, S. A Molecular Dynamics Method for Simulations in the Canonical Ensemble. *Mol. Phys.* **52**, 255–268 (2006).
23. Hoover, W. G. Constant-Pressure Equations of Motion. *Phys. Rev.* **34**, 2499 (1986).
24. Martyna, G. J., Tobias, D. J., Klein, M. L. Constant Pressure Molecular Dynamics Algorithms. *J. Chem. Phys.* **101**, 4177 (1998).
25. Parrinello, M., Rahman, A. Polymorphic Transitions in Single Crystals: A New Molecular Dynamics Method. *J. Appl. Phys.* **52**, 7182 (1998).
26. Hockney, R. W. & E. J. W. *Computer Simulation Using Particles.*, 1989.
27. Verlet, L. Computer "Experiments" on Classical Fluids. I. Thermodynamical Properties of Lennard-Jones Molecules. *Phys. Rev.* **159**, 98. (1967).
28. Ryckaert, J.-P., Ciccotti, G., Berendsen, H. J. C. Numerical Integration of the Cartesian Equations of Motion of a System with Constraints: Molecular Dynamics of n-Alkanes. *J. Comput. Phys.* **23**, 327–341 (1977).
29. Kabsch, W., Sander, C. Dictionary of Protein Secondary Structure: Pattern Recognition of Hydrogen-Bonded and Geometrical Features. *Biopolymers* **22**, 2577–2637 (1983).
30. Vivian, J. T., Callis, P. R. Mechanisms of Tryptophan Fluorescence Shifts in Proteins. *Biophys. J.* **80**, 2093–2109 (2001).
31. Mól, A. R., Castro, M. S., Fontes, W. NetWheels: A Web Application to Create High Quality Peptide Helical Wheel and Net Projections. *bioRxiv* 416347 (2018).
32. Gasymov, O. K., Glasgow, B. J. ANS Fluorescence: Potential to Augment the Identification of the External Binding Sites of Proteins. *BBA - Proteins and Proteom.* **1774**, 403–411 (2007).
33. Latypov, R. F., Liu, D., Gunasekaran, K., Harvey, T. S., Razinkov, V. I., Raibekas, A. A. Structural and Thermodynamic Effects of ANS Binding to Human Interleukin-1 Receptor Antagonist. *Protein Sci.* **17**, 652–663 (2008).
34. Ellis, R. J. Macromolecular Crowding: Obvious but Underappreciated. *Trends Biochem. Sci.* **26**, 597–604 (2001).
35. Okabe, K., Inada, N., Gota, C., Harada, Y., Funatsu, T., Uchiyama, S. Intracellular Temperature Mapping with a Fluorescent Polymeric Thermometer and Fluorescence Lifetime Imaging Microscopy. *Nat. Commun.* **3**, 1–9 (2012).
36. Kijima, T., Prince, T. L., Tigue, M. L., Yim, K. H., Schwartz, H., Beebe, K., Lee, S., Budzynski, M. A., Williams, H., Trepel, J. B., Sistonen, L., Calderwood, S., Neckers, L. HSP90 Inhibitors Disrupt a Transient HSP90-HSF1 Interaction and Identify a Noncanonical Model of HSP90-Mediated HSF1 Regulation. *Sci. Rep.* **8**, 1–13 (2018).

CHAPTER IV

Liquid-liquid Phase Separation of Heat Shock Factor 1 Driven by Secondary Structure Formation in Intrinsically Disordered Domain

Abstract

It is shown that Hsf1 undergoes heat induced conformational changes and oligomerization in Chapter III. Furthermore, Hsf1 oligomer forms condensates such as Hsf1 foci and nSBs under stressed condition, which upregulates the transcription of chaperones and protect several proteins such as splicing factor from damage. However, the environmental stresses and driving forces that proceeds Hsf1 assembly state changes from oligomer to liquid droplet are unknown.

In this chapter, I aimed to uncover the mechanism of stress-induced phase separation of Hsf1. Based on the knowledge that heat stress decreases intracellular pH, I observed Hsf1 solution at acidic pH, then found the formation of Hsf1 droplet. The acidification and heat effect synergistically to the formation of hydrophobic cluster coupling with secondary structural formation of Hsf1 IDR. This secondary structural formation is derived from LZ4 in IDR, and I found that the intermolecular interaction between LZ4 mediates the phase separation of Hsf1. From these results, I propose that the secondary structural change of LZ4 regulates the tertiary and quaternary conformational changes of close-monomer/open-monomer/multimer and the state change of oligomer/droplet.

4.1. Introduction

In the Chapter III, I revealed that Hsf1 changes to an open state, where the intramolecular LZ interaction is dissolved so that the LZs can form intermolecular contacts to form oligomers in the active form as the temperature increases. In the cell, Hsf1 oligomer forms the membrane-less organelle, the Hsf1 foci and nSBs, in the nucleus via liquid-liquid phase separation (LLPS). Recently, the structures of approximately 300 nm in diameter around HSE were observed by super-resolution microscopy in stressed condition cell and identified as Hsf1 foci formed by LLPS of Hsf1[1]. The Hsf1 foci is formed in a stress level-dependent manner, and the transcription of molecular chaperones are promoted in the Hsf1 foci[1]. Hsf1 also forms nSBs of approximately 1−3 μm in diameter on the satellite III (sat III) DNA repetitive sequences encoding non-coding sat III RNA[2–4]. Although the function of the nSBs has not been clear in many aspects, it is shown that several splicing factors and co-activator of transcriptional factors are assembled in nSBs to promote the expression of the proteins required in the recovery stage[5–7]. It has been proposed that nSBs not only protect these molecules from stress by isolating them internally, but also play a role in suppressing the production of non-heat shock protein transcripts to preferentially synthesize heat shock proteins under stress[7]. These liquid droplets are formed more in tumor cells than in normal cells. Therefore, Hsf1 droplet is supposed to be formed in a stress level-dependent manner and contribute to tumor cell growth and malignant transformation by promoting transcription of chaperones in cells.

LLPS of Hsf1 is a necessary reaction for transcriptional activation of Hsf1, however, the molecular mechanism of stress-induced phase separation of Hsf1 is not known. In several previous studies, heat stress was applied to cells to form Hsf1 droplets, but as shown in Chapter II, temperature changes caused Hsf1 to oligomerize, but no phase-separated droplets were formed *in vitro*, suggesting involvement of heat stress-induced intracellular environmental changes in phase separation for Hsf1 LLPS. The

elevated temperatures lead to a temporary drop in the pH of cells[8], and such stress-induced acidification is broadly conserved in eukaryotes including mammal[9]. In fact, experiments with yeast have shown that an elevated temperature causes a decrease in intracellular pH, which in turn induces expression of chaperones[10]. Notably, the formation of more nSBs in tumor cells than in normal cells, where the pH decreases due to an increase in the glycolysis system[11], suggests a possible relationship between the acidification and the phase separation of Hsf1[12].

In Chapter III, to uncover the mechanism of stress-induced phase separation of Hsf1, I evaluated the effect of acidification for Hsf1 LLPS and analyzed the conformational changes and interaction modes of Hsf1. I demonstrated that purified Hsf1 forms liquid droplets at acidic pH condition. The acidification and heat effect synergistically to the formation of hydrophobic cluster coupling with secondary structural formation of Hsf1 IDR. This secondary structural formation is derived from LZ4 in IDR, and I found that the intermolecular interaction between LZ4 mediates the phase separation of Hsf1.

4.2. Materials and Methods

Expression and purification of protein samples

The human Hsf1, Hsf1 IDR (209-529), and Hsf1 fragments (Hsf1 209-294, Hsf1 284-370, Hsf1 367- 446, Hsf1 437-529) expression constructs were cloned into a pET21b vector (Cat. No. 69741-3CN, Novagen, Madison, Wisconsin, USA) and fused to GB1-His^6 tags at the HRV3C N-terminus of the protease cleavage site. Hsf1 IDR and Hsf1 fragments were constructed through site-directed mutagenesis using the PrimeSTAR Mutagenesis Basal Kit (Cat. No. R046A, Takara Bio, Shiga, Japan). The expression and purification of Hsf1, Hsf1 IDR, and Hsf1 fragments are described in Chapter II.

NMR Spectroscopy

NMR samples were prepared in 20 mM MES (pH6.5), 100 mM NaCl, 5 mM $CaCl_2$, 0.02% NaN_3, 7% D_2O. Concentration of Hsf1 fragments were 100 μM. The experiments were performed at 25°C. NMR spectra were obtained with a Bruker AVANCE III 500 MHz spectrometer (Bruker, Billerica, MA) using a BBO probe. The 1D ^{1}H-NMR experiments were recorded with a data size of 32,768 complex points, an acquisition time of 1,310 ms, and 128 scans per experiment. The spectra were processed using Bruker TOPSPIN version 3.6.2.

CD spectroscopy

The CD spectra were recorded using a JASCO J-1500 CD spectrometer (Tokyo, Japan) with 1 mm path length cuvettes at 22℃ in 10 mM potassium phosphate buffer (pH 7.2) and 10 mM sodium acetate (pH 4.0). Each spectrum represents an integration of three consecutive scans from 190 to 260 nm at 1.0 nm intervals, with a scan speed of 20 nm/ min. Concentration of Hsf1 IDR was 3.0 μM.

Confocal microscopy

To prepare Hsf1 droplets, 35 μM Hsf1 and 5 μM Hsf1-GFP were incubated in the presence of 10 mM DTT. Fluorescence images of the Hsf1 droplets were obtained using a confocal microscope (FV1200, Olympus, Tokyo, Japan) equipped with a UPLSAPO 40X2 objective lens (NA 0.95).

Disorder predictions

Intrinsically disordered Hsf1 regions were predicted, using the "VSL2" algorithm of "Predictor of Natural Disordered Regions" (PONDR, http://www.pondr.com/).

Temperature dependent Hsf1 turbidity analysis

Absorbance at OD600 nm were measured with a JASCO V-730BIO from 5°C or 50°C. Concentration of Hsf1 IDR and Hsf1 IDR ΔLZ4 were all 10.0 μM, and these solutions prepared in 25 mM HEPES/KOH (pH 7.2) 150 mM KCl, 25 mM MES (pH 6.5, 6.0, 5.5) 150 mM KCl, and 25 mM sodium acetate (pH 4.0) 150 mM NaCl. Hsf1 solution in cuvettes were held at 5°C for 3 min then heated gradually at a rate of 1.0°C/min.

ANS Fluorescence spectroscopy

Fluorescence measurements were performed using a JASCO FP-8350 spectrofluorometer and using solutions prepared in 25 mM HEPES/KOH (pH 7.2) and 150 mM KCl, 25 mM MES (pH 6.5) 150 mM KCl, and 25 mM sodium acetate (pH 4.0, 4.5, 5.0) 150 mM NaCl. Concentration of Hsf1 IDR and Hsf1 IDR ΔLZ4 were all 3.0 μM. Emission spectra of ANS (Sigma-Aldrich, St Louis, USA) were recorded between 400 and 700 nm using a 350 nm excitation wavelength and a scan speed of 200 nm/min. Concentration of ANS was 50 μM. Each spectrum represents an integration of three consecutive scans.

4.3. Results

4.3.1 Droplet Formation of Hsf1 via Liquid–liquid Phase Separation

To verify whether Hsf1 forms liquid droplets, purified Hsf1 solutions at neutral and acidic pH were observed under a microscope. Hsf1 solution at pH 7.2 remained clear (Figure 4.1A), while Hsf1 solution at pH 5.5 was turbid, which was associated with the droplet formation following microscopic observation (Figure 4.1B). Differential interference contrast microscopy images revealed that droplets having round, globular shape were formed in the solution (Figure 4.1B). The incorporation of Hsf1 in the droplet was verified by confocal microscopy of the droplets formed in the presence of 0.1 equivalent Hsf1-green fluorescent protein (GFP), showing GFP-derived fluorescence in the droplets (Figure 4.1B). Thus, the data show that Hsf1 has the ability to form LLPS droplet under acidic environment.

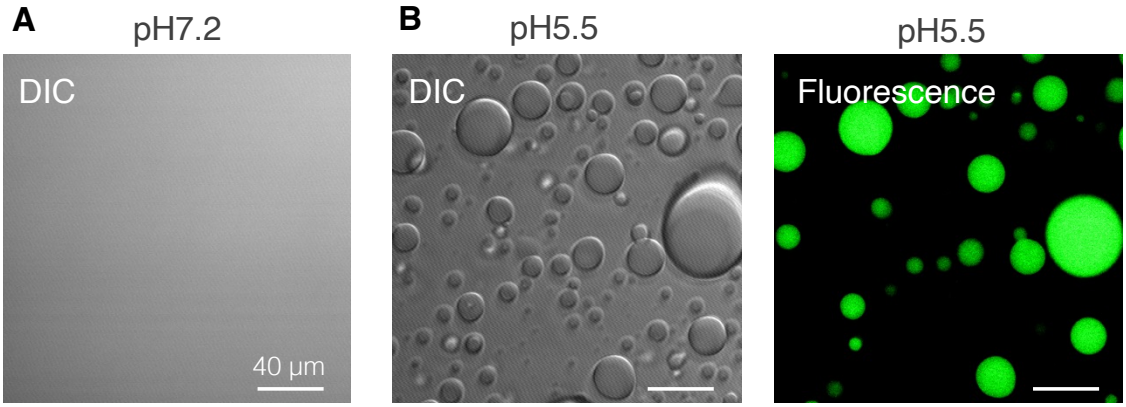

Figure 4.1 Hsf1 forms the droplets *in vitro*
(A) Representative images of differential interference contrast demonstrating the droplets formed by 40 μM Hsf1 in 25 mM HEPES (pH 7.2) 150 mM KCl 10 mM DTT. (B) Representative images of differential interference contrast and fluorescence demonstrating the droplets formed by 40 μM Hsf1 with 0.1 eq Hsf1-GFP in 25 mM MES (pH 5.5) 150 mM KCl 10 mM DTT. Scale bar, 40 μm.

The time-lapse imaging of the droplets using a confocal microscope demonstrated that the droplets fused with each other in approximately 1–2 min (Figure 4.2A), indicating that the internal mobility of Hsf1 droplets enables the rearrangement of

Hsf1 molecules, indicating that Hsf1 droplets are formed via LLPS and are characterized by adequate mobility to fuse with each other under acidic conditions (Figure 4.2). Notably, I evaluated the threshold at which Hsf1 forms droplets by the turbidity measurements, then Hsf1 undergoes LLPS at pH lower than pH 6.0 (Figure 4.2B).

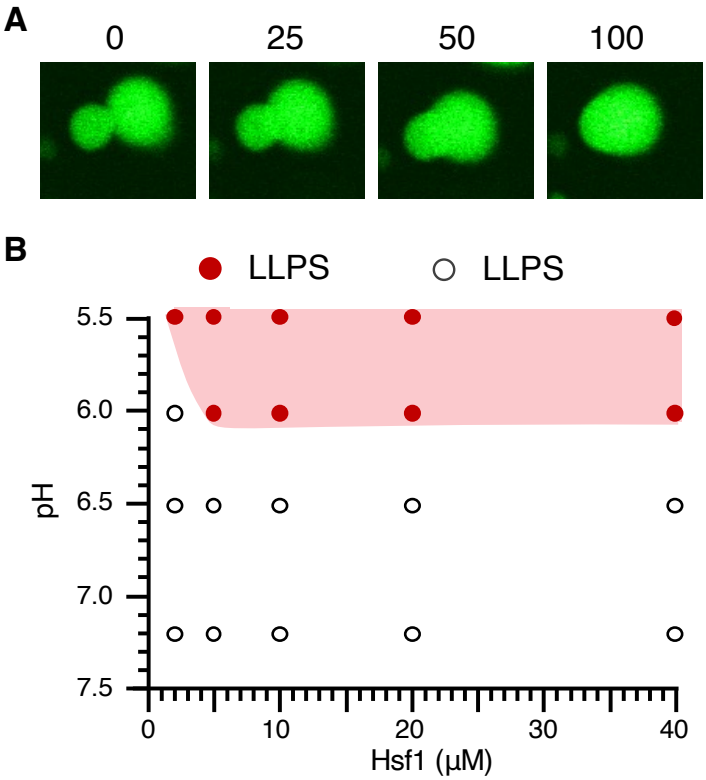

Figure 4.2 Hsf1 undergoes liquid-liquid phase separation at acidic pH
(A) Time-lapse fluorescence microscopy demonstrating fusion dynamics of Hsf1-GFP droplets. (B) Phase diagram of Hsf1 LLPS (Hsf1 concentration versus pH).

4.3.2 Synergetic Effects of Acidification and Heat on LLPS of Hsf1

To investigate whether acidic pH and heat can affect to Hsf1 droplet formation, the droplet formation was evaluated by turbidity of the solution at a wavelength of 600 nm under various conditions. The increase in turbidity was not observed with increasing temperature at pH 7.2 and 6.5 (Figure 4.3A, B). In contrast to these, the turbidity increased from around 32℃ at pH 6.0 and from around 22℃ at pH 5.5, and the solution was cloudy

after the measurements, suggesting that acidic conditions promoted phase separation (Figure 4.3A, B). Thus, LLPS of Hsf1 was enhanced by synergetic effect of the acidification and I found that Hsf1 has properties as a LCST (lower critical solution temperature) - type temperature-responsive polymer, which the solubility decreases and the solution becomes insoluble as the temperature increases.

To investigate whether heat-induced oligomerization of Hsf1 is required for the phase separation, the turbidity assay of Hsf1 monomer as an initial material at pH 5.5 was performed. While Hsf1 oligomer undergoes phase separation with a midpoint at 29.3 ℃, the turbidity of Hsf1 monomer solution increased with a midpoint at 35.7 ℃ (Figure 4.3C). It was shown that Hsf1 monomer undergoes oligomerization around 32 ℃ in Chapter II, then Hsf1 oligomer is a nucleus of the phase separation, and it is also indicated that the LZ4, which interacts with LZ1-3 when monomer and becomes free when oligomer, mediates the intermolecular interactions that drive phase separation.

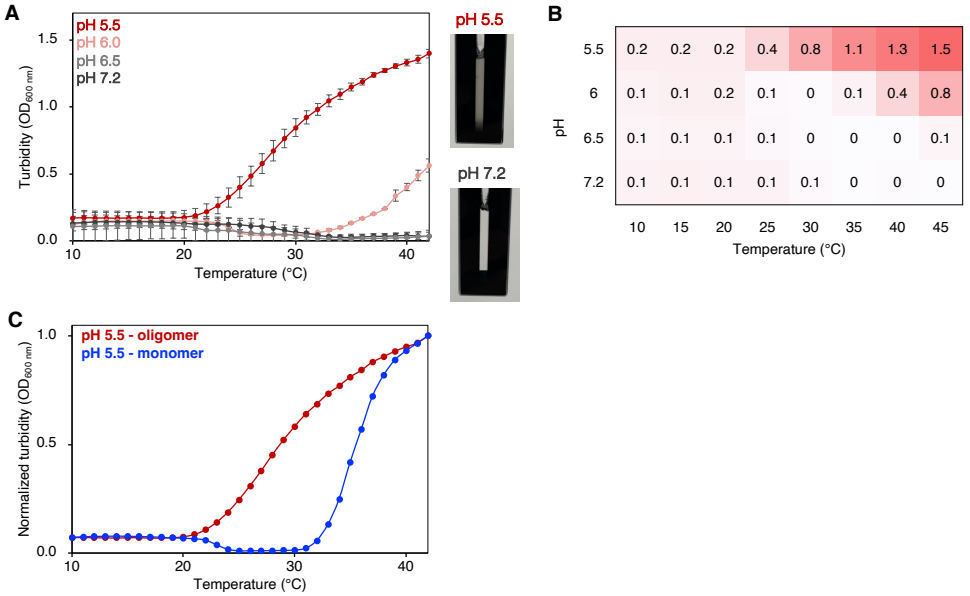

Figure 4.3 Turbidity assay to evaluate the effects of heat and pH for the droplet formation
(A) Turbidity of 10 μM Hsf1 oligomer in pH 5.5, 6.0, 6.5 (MES), and 7.2 (HEPES) buffer. (B) Heat map of turbidity. The numbers in the table represent the turbidity under each condition. (C) Turbidity of 10 μM Hsf1 oligomer and monomer in pH 5.5 buffer. Data were plotted as mean ± s.d., with n = 3 independent experiments (A, C).

4.3.3 Phase Separation Mediated by Secondary Structural Formation in the Hsf1 Intrinsically Disordered Domain

To clarify the molecular mechanism of Hsf1 droplet formation, I investigate the conformational changes of Hsf1 drive the phase separation. Previous studies on proteins forming phase-separated droplets have reported that liquid-liquid phase separation is driven by multivalent interactions between intrinsically disordered regions (IDR)[1314]. In the Hsf1 sequence, the regulatory domain (RegD), LZ4, and C-terminal activation domain (CTAD) are predicted to be IDR (Figure 4A). Furthermore, the 321-residue amino acid sequence of the Hsf1 IDR contains 16 basic amino acids, Arg and Lys, and 25 and 21 acidic amino acids, Asp (D) and Glu (E), respectively, and has a high net charge at neutral pH (pI 4.2) (Figure 4.4B, C). Ile, Leu, Val, Met, and Ala are contained in 89 residues (27.8 %), which is a relatively large number of hydrophobic amino acid residues for a general IDR (Figure 4.4B, C). This relatively high content of hydrophobic residues is one of the characteristics of IDRs that exhibit LCST-like phase separation behavior[15]. Thus, acidic conditions that decrease the net charge and high temperature that increase the hydrophobicity would be expected to induce the partial folding of Hsf1 IDR.

First, to test whether the interaction between Hsf1 IDR drives the phase separation of Hsf1, I expressed IDR and performed the microscopic observations of IDR solution in pH 4.0, pH 5.5, and pH 7.2. While IDR could not form droplets at pH 5.5 and pH 7.2, it was found that IDR alone also formed round-shape droplets at pH 4.0 (Figure 4.4D). As a control experiment, I evaluated the droplet formation of DBD, but no droplet formation was observed (Figure 4.4D). Then, it is showed that the interaction between IDR drives the droplet formation of Hsf1. Next, I performed the CD spectroscopic experiments to investigate the secondary structural change of IDR caused by the acidification. The CD spectra of IDR showed a minimum ellipticity at 200 nm, with the absence of characteristic bands in the 210-230 nm region, indicating that IDR is unfolded at pH 7.2. However, the minimum ellipticity of CD spectra shifted to 204 nm and the intensity around 220 nm increased at pH 4.0 (Figure 4.4E), reflecting pH-induced formation of secondary structure.

Since the excess negative charge of Hsf1 IDR at neutral pH would be neutralized at lower pH, this secondary structure formation leads to the formation of hydrophobic clusters. Then we performed the ANS fluorescence experiment to monitor the formation of such hydrophobic cluster. A decrease in pH led to a large blue shift of the ANS fluorescence maximum from ~530 to ~475 nm (Figure 4.4F), indicating the pH-induced formation of hydrophobic cluster. Therefore, Hsf1 IDR changes the conformation from unfolded state to ordered secondary structure, and this hydrophobic cluster formed by conformational changes drives the phase separation of Hsf1.

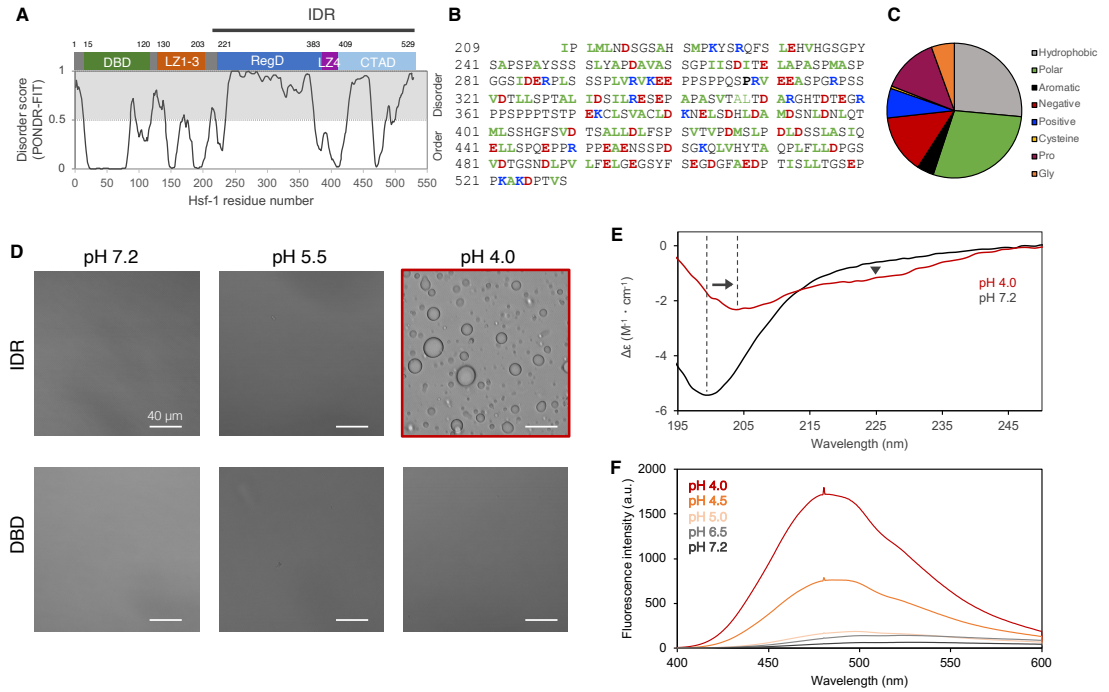

Figure 4.4 pH-induced droplet formation and conformational change of Hsf1 IDR
(A) Domain organization, location of cysteine residues in Hsf1, and disorder prediction of Hsf1 derived from PONDR program. (B) Amino acid sequence of IDR. Hydrophobic residues colored in green, acidic residues colored in red, and basic residues colored in blue. (C) Fraction types of amino acid residues of IDR. (D) Representative images of differential interference contrast demonstrating the droplets formed by 40 μM Hsf1 IDR in pH 7.2, pH 5.5, and pH 4.0. (E) CD spectra of Hsf1 IDR at pH 4.0 and 7.2. (F) ANS fluorescence spectra mixed with IDR at varying pH 4.0, 4.5, 5.0, 6.5, 7.2.

4.3.4 Intermolecular Interaction between LZ4 Drives LLPS of Hsf1

To clarify which region in the IDR is involved in the interaction in more detail, the IDR was divided into four fragments, regulatory domain-1 (RegD-1) (Hsf1 209-294), RegD-2 (Hsf1 284-370), LZ4 (Hsf1 367-446), and C-terminal transactivation domain (CTAD) (Hsf1 437-529), and NMR measurements were performed at different protein concentrations. Notably, I performed NMR experiments at pH 6.5 because the formation of phase-separated droplets significantly reduces the NMR signal intensity, making it difficult to track the NMR signal. NMR results showed that the intensity of some signals derived from RegD-1, RegD-2, and CTAD were decreased (Figure 4.5A, B, D). This signal intensity reduction suggests that these residues are involved in intermolecular interactions. However, the number of signals was small, suggesting that the intermolecular interactions between RegD-1, RegD-2, and CTAD are weak. On the other hand, the chemical shifts of LZ4-derived signals were most significantly perturbed in a concentration-dependent manner (Figure 4.5C), indicating that LZ4 has the largest contribution to the intermolecular interactions. The directions of the concentration-dependent chemical shift perturbations of LZ4 roughly coincided with those resulting from the lowering pH to 4.0 (Figure 4.5C), indicating that LZ4 forms secondary structure at bound state. Thus, concentration-dependent analysis by NMR reveals that secondary structural formation in the LZ4 region promotes intermolecular interactions.

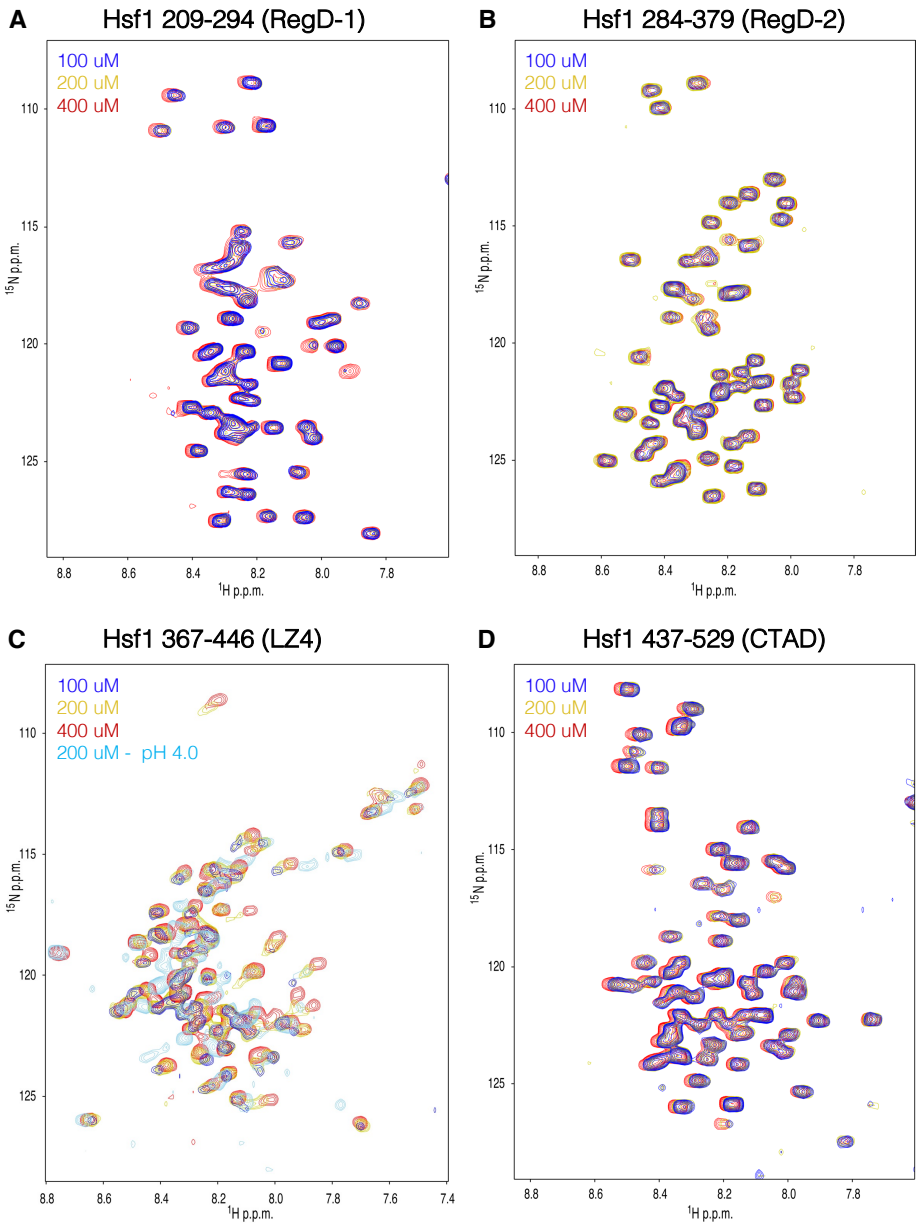

Figure 4.5 The Hsf1 IDR self-assembles via LZ4 domain
(A-D) ^{1}H-^{15}N HSQC spectra of Hsf1 209-294 (A), 284-379 (B), 367-446 (C), and 437-529 (D).

To evaluate the effect of the LZ4-mediated intermolecular interaction on phase separation, turbidity assay was performed with IDR and IDR ΔLZ4. The turbidity of IDR solution increased from around 15°C at pH 4.0, but that of IDR ΔLZ4 solution remained near zero (Figure 4.6A). The CD spectra of IDR ΔLZ4 at pH 4.0 showed a minimum ellipticity at 200 nm, with the absence of characteristic bands in the 210-230 nm region,

showing that IDR ΔLZ4 almost lost the ability of pH-induced secondary structure formation (Figure 4.6B). Therefore, it is showed that the secondary structure formation of LZ4 drives the intermolecular interactions and LLPS of Hsf1.

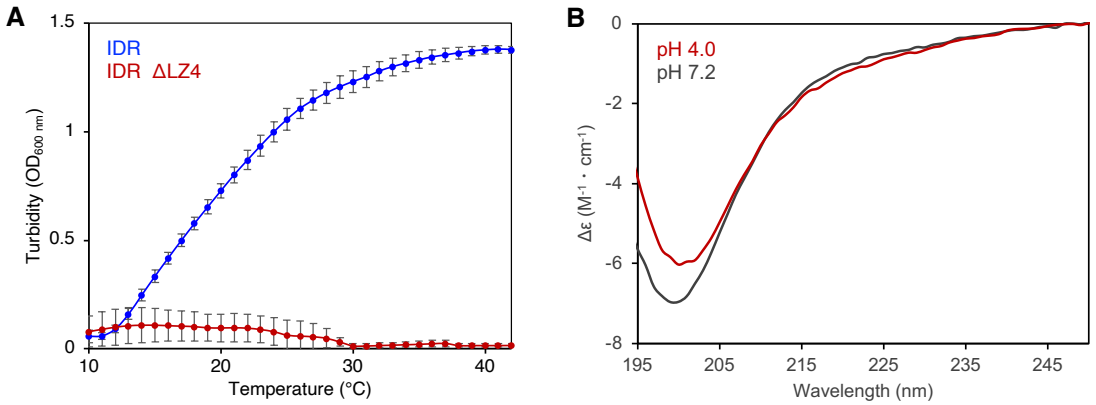

Figure 6 LZ4 is responsible for LLPS and conformational changes of Hsf1
(A) Turbidity of 10 μM IDR and IDR ΔLZ4 in pH 4.0 buffer. Data were plotted as mean ± s.d., with n = 3 independent experiments. (B) CD spectra of IDR ΔLZ4 at pH 4.0 and 7.2.

4.3.5 PPIase Promotes the Droplet Formation of Hsf1

As described above, Hsf1 undergoes LLPS via the formation of LZ4 secondary structure and hydrophobic clusters at acidic pH. Here, I hypothesized that the PPIase also regulates LLPS of Hsf1 because PPIase assists the protein folding by catalyzing the proline isomerization in the hydrophobic region of the substrate protein, as revealed in Chapter II. Then, we tested that whether FKBP52, a PPIase that has been shown to interact with Hsf1 in vivo [16], promotes the LLPS of Hsf1. In this experiment, I formed Hsf1 droplets by adding 10% (w/v) ficoll 400, a crowding agent. Previous reports on other IDRs of protein demonstrating that LLPS was enhanced by the excluded volume effect of the molecular crowders[17]. It was showed that the increase of turbidity is enhanced by the addition of 1 equivalent FKBP52 (Figure 4.7A). Furthermore, an increase in the number of Hsf1 droplets by the addition of FKBP52 was observed by fluorescence microscopy (Figure 4.7B). Here, to clarify whether this enhancement of droplet formation by FKBP52 is dependent on its PPIase activity, I compared the structure of the PPIase

domain of FKBP52 (FKBP52^{PPD}) and TF^{PPD}, and designed FKBP52 I87P mutant in which proline replaced I87 of FKBP52, corresponding to I195, the active center of TF^{PPD} (Figure 4.7C). Turbidity measurements showed that the increase in turbidity of Hsf1 was suppressed by the addition of FKBP52 I87P mutant compared to that before addition (Figure 4.7A), indicating that the PPIase activity of FKBP52 promotes phase separation of Hsf1. To evaluate whether FKBP52 could interact with LZ4 and promote its folding, I conducted NMR interaction analysis using FKBP52 and ^{15}N Hsf1 367-446 containing LZ4. Then, the chemical shift of ^{15}N Hsf1 367-446 derived NMR signal were perturbed by the addition of FKBP52, showing that FKBP52 could interacts with Hsf1 LZ4 (Figure 7D). Thus, it was suggested that FKBP52 interacts with LZ4 and catalyzes proline *cis/trans* isomerization to promote folding and phase separation of Hsf1.

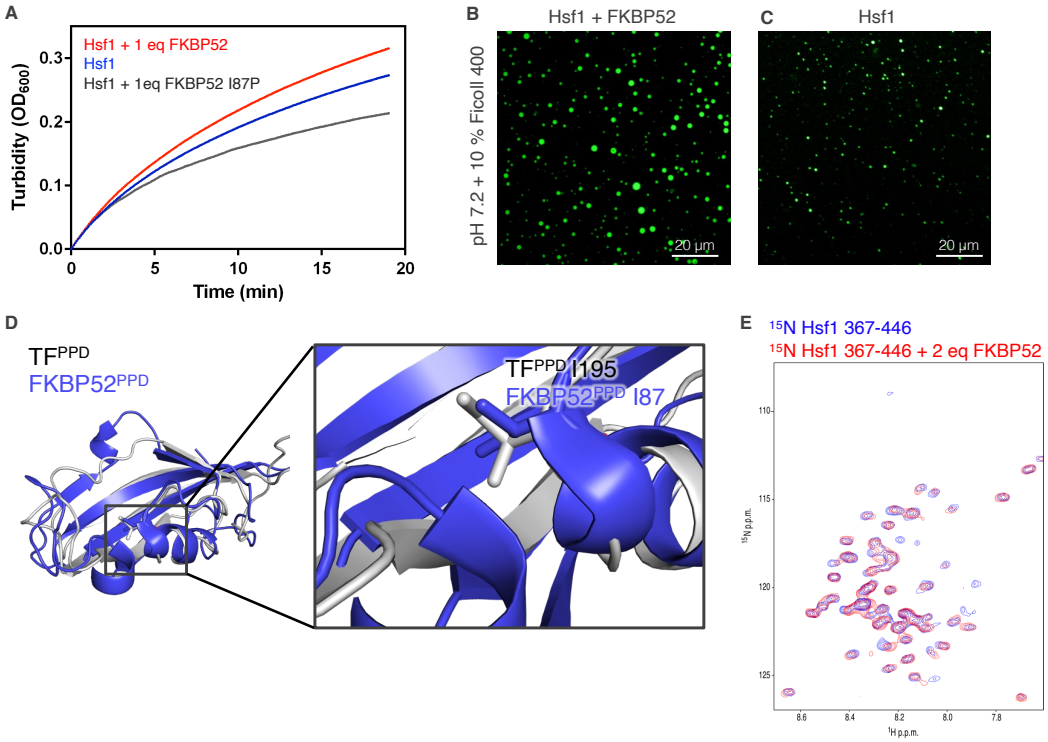

Figure 4.7 FKBP52 promotes the LLPS of Hsf1
(A) Turbidity of 10 μM Hsf1 oligomer in 25 mM HEPES (pH 7.2) 150 mM KCl 10 mM DTT 10% ficoll400. (B, C) Representative images of fluorescence demonstrating the droplets formed by 20 μM Hsf1 with 0.1 eq Hsf1-GFP in 25 mM HEPES (pH 7.2) 150 mM KCl 10 mM DTT with 1 eq FKBP52 (B) and without FKBP52 (C). Scale bar, 20 μm. (D) Comparison of the structure of TFPPD (PDB ID: 1w26) with that of human FKBP52^{PPD} (PDB ID: 6RCY). TF^{PPD} and FKBP52^{PPD} are colored gray and blue, respectively. (E) ^{1}H-^{15}N HSQC spectra of Hsf1 367-446 in the absence (blue) and presence (red) of 2 eq FKBP52.

4.4. Discussion

The present study revealed that LLPS of Hsf1 was driven by synergetic effect of the acidification and heat (Figure 4.1, 4.2, 4.3A, B). The elevated temperatures lead to a temporary drop in the pH of cells[8], and it has been shown in experiments with yeast that an increase in temperature causes a decrease in intracellular pH, which in turn induces expression of chaperones[10]. While the pH in normal cells is around 7.2-7.4, the pH in tumor cells is known to decrease to around 5.5 in malignant cases. Cellular observations using patient specimens have reported that more nSBs are observed in tumor cells than in normal cells[18], which may be a result of enhanced phase separation of Hsf1 due to the decrease in pH.

Turbidity assay showed that phase separation of Hsf1 proceeds with the oligomer as the nucleus (Figure 4.3C). While the IDR alone undergoes phase separation at pH 4.0 (Figure 4.4D, 4.6A), the full length of Hsf1 forms droples at above pH 6.0 (Figure 4.2B). The local concentration of IDR will be increased by oligomerization, which may promote the interaction between oligomers. TDP-43 and p53, which has phase-separating properties, also have oligomerization domain[19,20], then the regulation of phase separation through changes in oligomeric state may be a common mechanism in droplet formation. Although the interaction of each IDR molecule is weak[21], it is possible that the enough stability in the complex is achieved to undergo phase separation by oligomerization.

CD and NMR measurements showed that the acidification and heat induced the secondary structural formation of IDR, especially in LZ4 region (Figure 4.4E, F, 4.5, and 4.6). And turbidity assay shows that the intermolecular interaction between LZ4 is the main driving force for Hsf1 phase separation (Figure 4.6A). The large negative net charge of IDR (pI 4.2) is neutralized at acidic pH, and the overall hydrophobicity of a protein will increase with increasing temperature [22]. Although the LZ4 forms a helix with LZ1-3 at monomeric state and unfolds at oligomeric state at neutral pH, the LZ4 drives the intermolecular interaction with other Hsf1 molecules by the secondary structure

formation at acidic pH (Figure 4.4E, 4.6B). Therefore, the dehydration from the LZ4 region may promote secondary structure formation and hydrophobic interactions between LZ4. Since most phase-separating proteins have IDR, interactions between IDRs are supposed to drive phase separation, but several reports have proposed the importance of secondary structural formation in phase separation. TDP-43 has regions in the IDR that forms α-helix, and the interactions between these α-helix promote phase separation[19]. Moreover, the droplet of Fused in sarcoma (FUS) or hnRNPA2 were proposed to be stabilized by intermolecular interaction between cross-beta structure in IDR[2324]. Although there are few reports of secondary structure changes in phase-separated proteins, interestingly, the contribution of the structural formation in the phase separation of polymers exhibiting LCST is well studied in the field of polymer chemistry[25]. Then the secondary structural formation in IDR to facilitate intermolecular interactions may be a common mechanism to phase-separating proteins, not limited to Hsf1. In summary, acidification-induced LZ4 folding and binding drives the LLPS of Hsf1 (Figure 4.8).

One of the PPIases, FKBP52, was found to promote phase separation of Hsf1 (Figure 4.7, 4.8). This finding suggests that molecular chaperones, such as PPIase, not only assist in protein folding, but also promote the LLPS of Hsf1 and strengthen the transcriptional level of chaperones. I propose that this cycle in which chaperones, whose transcriptional upregulated by Hsf1, promote LLPS of Hsf1 would have the advantage of raising the stress response level of the Hsf1-chaperone system under stressed condition. Interestingly, Hsf1 droplets are more abundant in tumor cells than in normal cells[18], and FKBP52 is also upregulated in tumor cells[26]. Furthermore, elevated expression of FKBP52 in cancer cells is associated with poor prognosis in that cancer patient[27]. Therefore, it is possible that the enhancement of cytoprotective function by this cycle in Hsf1-chaperone system contributes to the malignant transformation of cancer, and it will be important to elucidate the mechanism of interaction between chaperones and Hsf1 from the viewpoint of disease therapy.

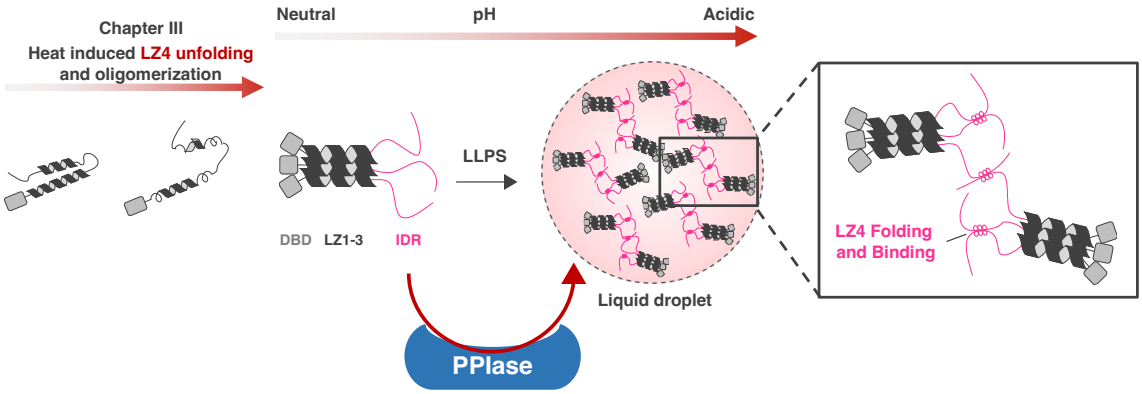

Figure 4.8 Proposed model of acidification-induced droplet formation of Hsf1
LLPS of Hsf1 is induced at acidic pH. pH-dependent LZ4 folding and binding drives the LLPS.

References

1. Zhang, H., Shao, S., Zeng, Y., Wang, X., Qin, Y., Ren, Q., Xiang, S., Wang, Y., Xiao, J., Sun, Y. Reversible Phase Separation of HSF1 Is Required for an Acute Transcriptional Response during Heat Shock. *Nat. Cell Biol.* **24**, 340–352 (2022).
2. Jolly, C., Konecny, L., Grady, D. L., Kutskova, Y. A., Cotto, J. J., Morimoto, R. I., Vourc'h, C. In Vivo Binding of Active Heat Shock Transcription Factor 1 to Human Chromosome 9 Heterochromatin during Stress. *J. Cell Biol.* **156**, 775–781 (2002).
3. Biamonti, G., Vourc'h, C. Nuclear Stress Bodies. *Cold Spring Harb. Perspect. Biol* **2**, a000695 (2010).
4. Biamonti, G. Nuclear Stress Bodies: A Heterochromatin Affair? *Nat. Rev. Mol. Cell Biol*. **5**, 493–498 (2004).
5. Ninomiya, K., Adachi, S., Natsume, T., Iwakiri, J., Terai, G., Asai, K., Hirose, T. LncRNA-Dependent Nuclear Stress Bodies Promote Intron Retention through SR Protein Phosphorylation. *EMBO J.* **39**, e102729 (2020).
6. Ninomiya, K., Iwakiri, J., Aly, M. K., Sakaguchi, Y., Adachi, S., Natsume, T., Terai, G., Asai, K., Suzuki, T., Hirose, T. M6A Modification of HSATIII LncRNAs Regulates Temperature-Dependent Splicing. *EMBO J.* **40**, e107976. (2021).
7. Goenka, A., Sengupta, S., Pandey, R., Parihar, R., Mohanta, G. C., Mukerji, M., Ganesh, S. Human Satellite-III Non-Coding RNAs Modulate Heat-Shock-Induced Transcriptional Repression. *J. Cell Sci.* **129**, 3541–3552 (2016).
8. Weitzel, G., Pilatus, U., Rensing, L. Similar Dose Response of Heat Shock Protein Synthesis and Intracellular PH Change in Yeast. *Exp. Cell Res.* **159**, 252–256. (1985).
9. Díaz, F. E., Dantas, E., Cabrera, M., Benítez, C. A., Delpino, M. v., Duette, G., Rubione, J., Sanjuan, N., Trevani, A. S., Geffner, J. Fever-Range Hyperthermia Improves the Anti-Apoptotic Effect Induced by Low PH on Human Neutrophils Promoting a Proangiogenic Profile. *Cell Death Dis.* **7**, e2437–e2437. (2016).
10. Triandafillou, C. G., Katanski, C. D., Dinner, A. R., Allan Drummond, D. Transient Intracellular Acidification Regulates the Core Transcriptional Heat Shock Response. *Elife* **9**, 1–30 (2020).
11. Gerweck, L. and Seetheraman, K. Cellular pH Gradient in Tumor versus Normal Tissue: Potential Exploitation for the Treatment of Cancer. *Cancer Res.* **56**, 1194-8 (1996).
12. Kondo, A., Yamamoto, S., Nakaki, R., Shimamura, T., Hamakubo, T., Sakai, J., Kodama, T., Yoshida, T., Aburatani, H., Osawa, T. Extracellular Acidic PH Activates the Sterol Regulatory Element-Binding Protein 2 to Promote Tumor Progression. *Cell Rep.* **18**, 2228–2242 (2017).
13. Kato, M., Han, T. W., Xie, S., Shi, K., Du, X., Wu, L. C., Mirzaei, H., Goldsmith, E. J., Longgood, J., Pei, J., Grishin, N. v., Frantz, D. E., Schneider, J. W., Chen, S., Li, L., Sawaya, M. R., Eisenberg, D., Tycko, R., McKnight, S. L. Cell-Free Formation of RNA Granules: Low Complexity Sequence Domains Form Dynamic Fibers within Hydrogels. *Cell* **149**, 753–767 (2012).
14. Ray, S., Singh, N., Kumar, R., Patel, K., Pandey, S., Datta, D., Mahato, J., Panigrahi, R., Navalkar, A., Mehra, S., Gadhe, L., Chatterjee, D., Sawner, A. S., Maiti, S., Bhatia, S., Gerez, J. A., Chowdhury, A., Kumar, A., Padinhateeri, R., Riek, R., Krishnamoorthy, G., Maji, S. K. α-Synuclein Aggregation Nucleates through Liquid–Liquid Phase Separation. *Nat. Chem.* **12**, 705–716 (2020).
15. Ruff, K. M., Roberts, S., Chilkoti, A., Pappu, R. v. Advances in Understanding Stimulus-

Responsive Phase Behavior of Intrinsically Disordered Protein Polymers. *J. Mol. Biol.* **430**, 4619–4635 (2018).
16. Guo, Y., Guettouche, T., Fenna, M., Boellmann, F., Pratt, W. B., Toft, D. O., Smith, D. F., Voellmy, R. Evidence for a Mechanism of Repression of Heat Shock Factor 1 Transcriptional Activity by a Multichaperone Complex. *J. Biol. Chem.* **276**, 45791–45799 (2001).
17. André, A. A. M., Spruijt, E. Liquid–Liquid Phase Separation in Crowded Environments. *Int. J. Mol. Sci.* **21**, 5908 (2020).
18. Gaglia, G., Rashid, R., Yapp, C., Joshi, G. N., Li, C. G., Lindquist, S. L., Sarosiek, K. A., Whitesell, L., Sorger, P. K., Santagata, S. HSF1 Phase Transition Mediates Stress Adaptation and Cell Fate Decisions. *Nat. Cell Biol*. **22**, 151–158 (2020).
19. Conicella, A. E., Zerze, G. H., Mittal, J., Fawzi, N. L. ALS Mutations Disrupt Phase Separation Mediated by α-Helical Structure in the TDP-43 Low-Complexity C-Terminal Domain. *Structure* **24**, 1537–1549 (2016).
20. Kamagata, K., Kanbayashi, S., Honda, M., Itoh, Y., Takahashi, H., Kameda, T., Nagatsugi, F., Takahashi, S. Liquid-like Droplet Formation by Tumor Suppressor P53 Induced by Multivalent Electrostatic Interactions between Two Disordered Domains. *Sci. Rep.* **10**, 1–12 (2020).
21. Boyko, S., Qi1, X., Chen, T. H., Surewicz, K., Surewicz, W. K. Liquid-Liquid Phase Separation of Tau Protein: The Crucial Role of Electrostatic Interactions. *J. Biol. Chem.* **294**, 11054–11059 (2019).
22. Wolfenden, R., Lewis, C. A., Yuan, Y., Carter, C. W. Temperature Dependence of Amino Acid Hydrophobicities. *Proc. Natl. Acad. Sci. U S A* **112**, 7484–7488 (2015).
23. Murray, D. T., Kato, M., Lin, Y., Thurber, K. R., Hung, I., McKnight, S. L., Tycko, R. Structure of FUS Protein Fibrils and Its Relevance to Self-Assembly and Phase Separation of Low-Complexity Domains. *Cell* **171**, 615-627:e16 (2017).
24. Xiang, S., Kato, M., Wu, L. C., Lin, Y., Ding, M., Zhang, Y., Yu, Y., McKnight, S. L. The LC Domain of HnRNPA2 Adopts Similar Conformations in Hydrogel Polymers, Liquid-like Droplets, and Nuclei. *Cell* **163**, 829–839 (2015).
25. Quiroz, F. G., Li, N. K., Roberts, S., Weber, P., Dzuricky, M., Weitzhandler, I., Yingling, Y. G., Chilkoti, A. Intrinsically Disordered Proteins Access a Range of Hysteretic Phase Separation Behaviors. *Sci. Adv.* **5**, 5177–5195 (2019).
26. Habara, M., Sato, Y., Goshima, T., Sakurai, M., Imai, H., Shimizu, H., Katayama, Y., Hanaki, S., Masaki, T., Morimoto, M., Nishikawa, S., Toyama, T., Shimada, M. FKBP52 and FKBP51 Differentially Regulate the Stability of Estrogen Receptor in Breast Cancer. *Proc. Natl. Acad. Sci. U S A* **119**, e2110256119 (2022).
27. Storer, C. L., Dickey, C. A., Galigniana, M. D., Rein, T., Cox, M. B. FKBP51 and FKBP52 in Signaling and Disease. *Trends in Endocrinol. Metab.* **22**, 481–490 (2011).

CHAPTER V

Oxidative Hyperoligomerization Drives Phase Transition of Heat Shock Factor 1

Abstract

The assembly of Hsf1 proceeds depending on the length and intensity of the stress, and Hsf1 becomes a gel-like droplet with reduced internal-mobility under excessive stress. It has been reported that cells with such gel-like Hsf1 droplets are reduced transcriptional level of chaperones and a higher tendency to apoptosis. The phase transition of Hsf1 to gel-like droplet is regarded as a reaction that mediates Hsf1 function from cytoprotection to cell death, but the mechanism of phase transition remains unclear. In this chapter, I found that Hsf1 undergoes phase transition into gel-like droplets in response to oxidative conditions. The mechanism for formation and oxidative phase transition of the Hsf1 liquid droplets were investigated by observation of the internal architecture of the Hsf1 droplets by holotomography imaging, corroborated by molecular dynamics simulation and biophysical/biochemical experiments. These data showed that oxidative condition is sensed by the disulfide-bond–mediated hyperoligomerization of Hsf1, leading to formation of core particles in the heterogeneous architecture of the droplet. Collectively, the presented data demonstrate how Hsf1 undergoes oxidative phase transition by sensing redox conditions to potentially drive the cell fate decision.

5.1. Introduction

In Chapter IV, I revealed that Hsf1 forms liquid droplets via liquid-liquid phase separation under acidic condition. Conversely, under prolonged stress, Hsf1 foci and nSBs undergo decreased fluidity and liquid-to-gel–like phase transition [1], which has been linked to down-regulation of chaperones and mediate apoptosis. In stressed conditions, including heat, pH change, and oxidation, cells are subjected to either survival via increased expression of stress response proteins or cell death signaling[2]. Such cell fate decision is a strategy for homeostasis in higher organisms, and the liquid-to-gel–like phase transition of Hsf1 may be the key response in cell fate decision. Nevertheless, the mechanism of phase transition of Hsf1 droplet in response to stress remain to be elucidated.

In this chapter, I demonstrated that purified Hsf1 undergoes phase transition into gel-like condensates in the oxidative conditions. Moreover, the internal architecture of the Hsf1 droplets were visualized by holotomography (HT) imaging that is a label-free microscopic method to reconstitute images from three-dimensional refractive index (RI) tomogram[3]. HT on Hsf1 droplet at oxidative condition showed inhomogeneous distribution of the protein, forming core particles. Further biochemical and biophysical experiments suggested that the core particles consist of hyper-oligomerized Hsf1 mediated by disulfide bonds among conserved Cys residues. This oxidative hyperoligomerization of Hsf1 was also formed in the cell treated in the oxidative condition. The data demonstrate the ability of Hsf1 to sense redox conditions in the cytosol and nucleus. Although cytosol and nucleus are regulated in the reductive condition, several reports have shown that the continuous stress induce oxidation of the cytosol[4–6], highlighting the importance of redox-dependent hyperoligomerization and phase transition of Hsf1 to sense duration and extent of the stress.

5.2. Materials and methods

Expression and purification of protein samples

Hsf1 CS mutant (C36S/C103S/C153S/C373S/C378S) was then constructed through site-directed mutagenesis using the PrimeSTAR Mutagenesis Basal Kit (Cat. No. R046A, Takara Bio, Shiga, Japan). The expression and purification of Hsf1, Hsf1 CS mutant, and Hsf1-GFP are described in Chapter III.

Confocal microscopy

To prepare Hsf1 droplets, 45 μM Hsf1 and 5 μM Hsf1-GFP were incubated in the presence/absence of 10 mM DTT and 10% (w/v) ficoll 400 (Cat. No. 16006-92, Nacalai Tesque, Kyoto, Japan), dextran 200 (Cat. No. 10927-12, Nacalai Tesque), or PEG 8000 (Cat. No. HR2-515, Hampton Research, Journey Aliso Viejo, CA, USA). Fluorescence images of the Hsf1 droplets were obtained using a confocal microscope (FV1200, Olympus, Tokyo, Japan) equipped with a UPLSAPO 40X2 objective lens (NA 0.95).

Fluorescence recovery after photobleaching

FRAP experiments was performed in in vitro droplets formed by Hsf1, that were mixed with Hsf1-GFP, using the 473 nm laser line of a confocal microscope (FV1200, Olympus) that was equipped with a UPLSAPO 40X2 objective lens (NA 0.95). For each droplet, either the whole droplet or a specific spot (diameter of 5 μm) was bleached at 80% transmission (50 mW laser power) for 2–10 s, after which post-bleach time-lapse images were collected (0.5 s frame rate, 180 frames). The resulting images were analyzed as follows: A 5 μm diameter region of interest (ROI) was placed on the bleached whole droplet or the bleached spot. Fluorescence intensity of the ROI was then calculated using FV10-ASW (Olympus). The post-irradiation fluorescence intensity was then normalized, using the difference between the intensity before irradiation and the intensity of the first frame immediately after irradiation as one. Finally, the recovery of the post-irradiation

fluorescence intensity was analyzed using Prism 5 (GraphPad Software, San Diego, CA, USA).

SEC-MALS experiments

SEC-MALS method is described in Chapter II Bio SEC-5, 1000Å gel filtration column (Cat. No. AG5190-2536, Agilent Technologies, Santa Clara, CA, USA) was connected to an SEC-MALS system.

Holotomography imaging

Three-dimensional (3D) quantitative phase imaging and its corresponding fluorescence live BM2 cell images were obtained using a commercial holotomography instrument (HT-2H, Tomocube Inc, Daejeon, Korea), which is based on Mach–Zehnder interferometry, equipped with a digital micromirror device. The coherent monochromatic laser ($\lambda = 532$ nm) was divided into two paths, a reference, and a sample beam, respectively, using a 2×2 single-mode fiber coupler. Visualization of 3D RI maps was then performed using a commercial software (TomoStudio, Tomocube Inc.). The RI reference buffer was 25 mM HEPES/KOH (pH 7.2), 150 mM KCl, and 5% (w/v) ficoll 400, 200 μL. Moreover, 75 μM Hsf1 that was incubated in the presence/absence of 10 mM DTT and 5% (w/v) ficoll 400 was added to 50 μL of the RI reference buffer, after which RI images of Hsf1 droplets were measured. To determine the mean RI of the Hsf1 droplets, the images of the slices in the xy-plane at the center of the droplet were initially exported, with the RI ranging from 1.349–1.402 as a gray gradient color image. In order to quantify the RI inside the Hsf1 droplets, 3−8 μm droplets were selected and the mean RI of each droplet was then determined to generate a scatter plot. Finally, the exported image was analyzed using the ImageJ software (National Institutes of Health, Bethesda, MD), and its gradients were numerically converted to 256 steps. The mean RI of each

droplet was also determined using Prism 5 (GraphPad Software). Data were analyzed using Welch's *t* test.

Gel-based analysis of Hsf1 redox states under oxidative or reductive conditions

Hsf1 (50 μM) was incubated with a reaction buffer, containing 25 mM HEPES-KOH (pH 7.2) and 150 mM KCl in the absence or presence of 10 mM DTT at 20°C for 1 h. To prepare NEM quenched samples, a 12 μL aliquot was collected from the reaction mix, after which 48 μL of 90 mM NEM (Cat. No. 15512-24, Nacalai Tesque) were added to quench the reaction. Additionally, 60 μL of Laemmli 4 × sodium dodecyl sulfate (SDS)-sample buffer[7] were added to these samples (total volume: 120 μL). Samples were then separated by SDS-PAGE using 8% bis-tris gels (Cat. No. NW00080BOX, Thermo Fisher Scientific, Waltham, MA, USA). To prepare reducing samples, a 12 μL sample aliquot, 48 μL distilled water, and 60 μL SDS-sample buffer, containing 5% (v/v) β-mercaptoethanol (Cat. No. 15512-24, Nacalai Tesque) were mixed to reduce and denature the samples.

Gel-based analysis of Hsf1 oligomeric states in redox buffers

Redox buffers were prepared by mixing reduced glutathione (GSH, Cat. No. 17050-14, Nacalai Tesque) and oxidized glutathione (GSSG, Cat. No. 06440-31, Nacalai Tesque) in the following final concentration ratios: 9.8 mM GSH and 0.1 mM GSSG (100:1), 6.0 mM GSH and 2.0 mM GSSG (3:1), or 0.2 mM GSH and 4.9 mM GSSG (1:25). Hsf1 (5 μM) was incubated at 37˚C 1 h with reaction buffer containing 50 mM Tris-HCl (pH 8.0), 150 mM KCl in the absence/presence of 10 mM DTT, or in the presence of a redox buffer. A 40 μL aliquot was taken from reaction mix and 10 μL of 40 mM NEM (Nacalai Tesque) was added to quench the reaction. In addition, 50 μL of Laemmli 4 × SDS-sample buffer[7] was added to these samples (total volume: 100 μL), and they were separated by SDS-PAGE using 8% bis-tris gels (Thermo Fisher Scientific).

Cell culture

HAP1 cells were cultured and maintained in Iscove's modified Dulbecco's medium containing L-Gln and HEPES (Cat. No. 11506-05, Nacalai Tesque) and 10% fetal bovine serum (FBS, Cat. No. S-FBS-NL-015, Serana, Brandenburg, Germany).

Immunofluorescence under various stressed conditions

To analyze the formation of Hsf1 foci in HAP1 cells, the cells were seeded on coverslips (Cat. No. C018001, Matsunami Glass Ind., Osaka, Japan) pre-treated with ε-poly-L-lysine coating solution (Cat. No. SPL01, Cosmo Bio Co., Tokyo, Japan). After a 1-day incubation, the cells were treated with fresh cell culture medium (37°C control) or pre-warmed cell culture medium at 43°C (heat shock) for 1 h on a water bath of the respective temperature, with cell culture medium in the absence/presence of 0.5, 1.0 mM H_2O_2, 1.0, 3.0 mM TBH for 1 h, or with cell culture medium containing 0.1% (v/v) DMSO in the absence/presence of 2 μM MG132 (Cat. No. CS-0471, ChemScene, Monmouth Junction, NJ, USA) or 2 μg/mL tunicamycin (Cat. No. 202-08241, Fujifilm Wako Pure Chemical, Osaka, Japan) for 2 h. The treated cells were washed twice with phosphate-buffered saline (PBS, 10 mM Na_2HPO_4, 1.76 mM KH_2PO_4, 137 mM NaCl, 2.7 mM KCl) at room temperature (RT) and fixed with 4%-paraformaldehyde phosphate buffer solution (Cat. No. 09154-58, Nacalai Tesque) for 15 min at RT. The fixed cells were washed four times with PBS at RT, permeabilized with PBS containing 0.1% TritonX-100 (Cat. No. 12967-32, Nacalai Tesque) for 15 min, and blocked with PBS containing 2% FBS for 1 h at RT. The cells were then incubated at 4°C with the corresponding antibodies against Hsf1 (Cat No. 4356, Cell Signaling Technology, Danvers, MA, USA, 1:500) and HSP70 (Cat No. sc-24, Santa Cruz Biotechnology, Santa Cruz, CA, USA, 1:200) diluted in PBS containing 2% FBS overnight. Following the incubation, the samples were washed thrice with PBS at RT. The cells were then incubated at 4°C for 1 h with CF488A-conjugated donkey anti-rabbit IgG (Cat No. 20015-

1, Biotium, Hayward, CA, USA, 1:2000) and CF568-conjugated goat anti-mouse IgG (Cat No. 20101-1, Biotium, 1:2000) antibodies diluted in PBS containing 2% FBS as secondary antibodies. Finally, the nuclei of the cells were stained with DAPI solution (Cat. No. 19178-91, Nacalai Tesque, 1:10000). The fluorescent images were obtained using a confocal microscope (FV1200, Olympus) equipped with a 60× silicon oil-immersion objective lens (UPLSAPO60XS2, Olympus, NA 1.30).

Immunoblotting under oxidative conditions

To investigate Hsf1 oligomerization under oxidative stress, HAP1 cells (5.0×10^4 cells) were plated on a 6-well plate. After a 3-day incubation, the cells were treated with cell culture medium in the absence/presence of 0.5, 1.0 mM H_2O_2, or 1.0, 3.0 mM TBH (Cat. No. 026-13451, Fujifilm Wako Pure Chemical). The treated cells were incubated for an additional 1 h and then washed twice with PBS at 37°C, following which they were acid quenched with ice-cold 10%(w/v) TCA (Cat. No. 34637-14, Nacalai Tesque) on ice[8]. The harvested cells were centrifuged at 15,000 ×g for 2 min at 4°C. The precipitants were washed and sonicated twice in ice-cold acetone with Bioruptor UCD-300 (Tosho Denki, Yokohama, Japan) before being dissolved in SDS-sample buffer containing NEM (2% (w/v) SDS, 100 mM Tris-HCl (pH 6.8), 50 mM NEM). The samples were separated by SDS-PAGE using 6% tris-glycine gels (Cat. No. XP00060BOX, Thermo Fisher Scientific), transferred to PVDF membranes (Cat. No. IPVH07850, Merck Millipore, Darmstadt, Germany) using eBlot L1 (GenScript, Piscataway, NJ, USA), and blotted with anti-Hsf1 antibody (Cat. No. 4356, Cell Signaling Technology, 1:1000) diluted in Signal Enhancer HIKARI Solution A (Cat. No. 02270-81, Nacalai Tesque) and secondary anti-rabbit antibody (Cat. No. 711-035-152, Jackson ImmunoResearch Laboratories, West Grove, PA, USA, 1:10000) diluted in Signal Enhancer HIKARI Solution B. Chemiluminescent signals were visualized using Chemi-Lumi One Ultra (Cat. No. 11644-24, Nacalai Tesque) and scanned using the ImageQuant LAS 4000 Mini (Fujifilm,

Tokyo, Japan) and Amersham ImageQuant 800 (Cytiva). Total protein concentration was measured by CBB staining (Appendix Figure. S2). Signal intensities were analyzed using ImageJ/Fiji[9] and Microsoft Excel. Signal intensities of chemiluminescence were normalized by the signal intensity of CBB staining for total proteins. The Relative signal intensities corresponding to higher-order oligomeric Hsf1 were calculated by comparison with the control lane of each membrane. Data were processed by analysis of variance (ANOVA), followed by Tukey–Kramer test.

5.3. Results

5.3.1 Redox-dependent Formation of Hsf1 Droplets in Cell

It was previously shown that the formation of Hsf1 droplets progress in correlation to the duration and intensity of the stress[1], but the mechanism of phase transition has not been fully elucidated. To evaluate Hsf1 droplet formation under various types of stress, I observed Hsf1 in the cultured HAP1 cells treated with heat shock (HS), oxidant H_2O_2 or *tert*-butyl hydroperoxide (TBH), proteasome inhibitor MG132, and endoplasmic reticulum (ER) stress inducer tunicamycin (TM) (Figure 5.1A). In microscopic observation, foci in the nucleus were observed after HS, indicating that HS induced Hsf1 droplet formation (Figure 5.1A), as seen in the previous works[10–13]. In addition, H_2O_2, TBH, and MG132 also induced nSB formation for a subset of the cells (Figure 5.1A). Because change in Hsf1 localization modulates chaperone expression, localization of HSP70 chaperone was monitored (Figure 5.1A). The data showed that HSP70 migrated to the nucleus after HS (Figure 1.1A). After H_2O_2 and TBH treatment, a subset of the cells showed HSP70 migrated to the nucleus and formed foci (Figure 5.1A). Furthermore, the production of reactive oxygen species (ROS) is enhanced in cells stressed by HS and MG132, and the intracellular environment becomes more oxidative[4–6]. These results suggest that oxidative stress can also induce Hsf1 droplet formation.

To evaluate the assembly state of Hsf1 in an oxidizing environment, the oligomerization of Hsf1 was further evaluated in redox conditions that correspond to intracellular environments (Figure 5.1B, C). The redox conditions, in particular, were set by varying ratios of reduced glutathione (GSH) and oxidized glutathione (GSSG). In the relatively oxidative condition, with a GSH:GSSG ratio of 3:1 (corresponding to the ER environment)[14], the fraction of higher-order oligomers increased while the fraction of monomers decreased (Figure 5.1B, C) compared with the fractions in the relatively reducing condition with a ratio of 100:1 (corresponding to the cytosolic environment)[14]. The trend of increasing fraction of the disulfide-bonded Hsf1 higher-order oligomers was

even more robust in more oxidative conditions, with a ratio of 1:25. To examine the redox sensing by Hsf1 in cells, Hsf1 oligomerization was assessed using immunoblotting in HAP1 cells treated with the oxidants H_2O_2 or TBH. Under unstressed conditions (none), most Hsf1 existed as a monomer (Figure 5.1D). In the cells treated with oxidants showed more content of higher-order oligomers of Hsf1, and the amount of its higher-order oligomers increased significantly in a dose-dependent manner of the oxidants (Figure 5.1D-F). Based on the fact that the redox conditions in the cytosol vary depending on the external or local conditions[15–17], these data indicate that Hsf1 can sense the redox environment in the cell by modulating the abundance of the disulfide-linked oligomers.

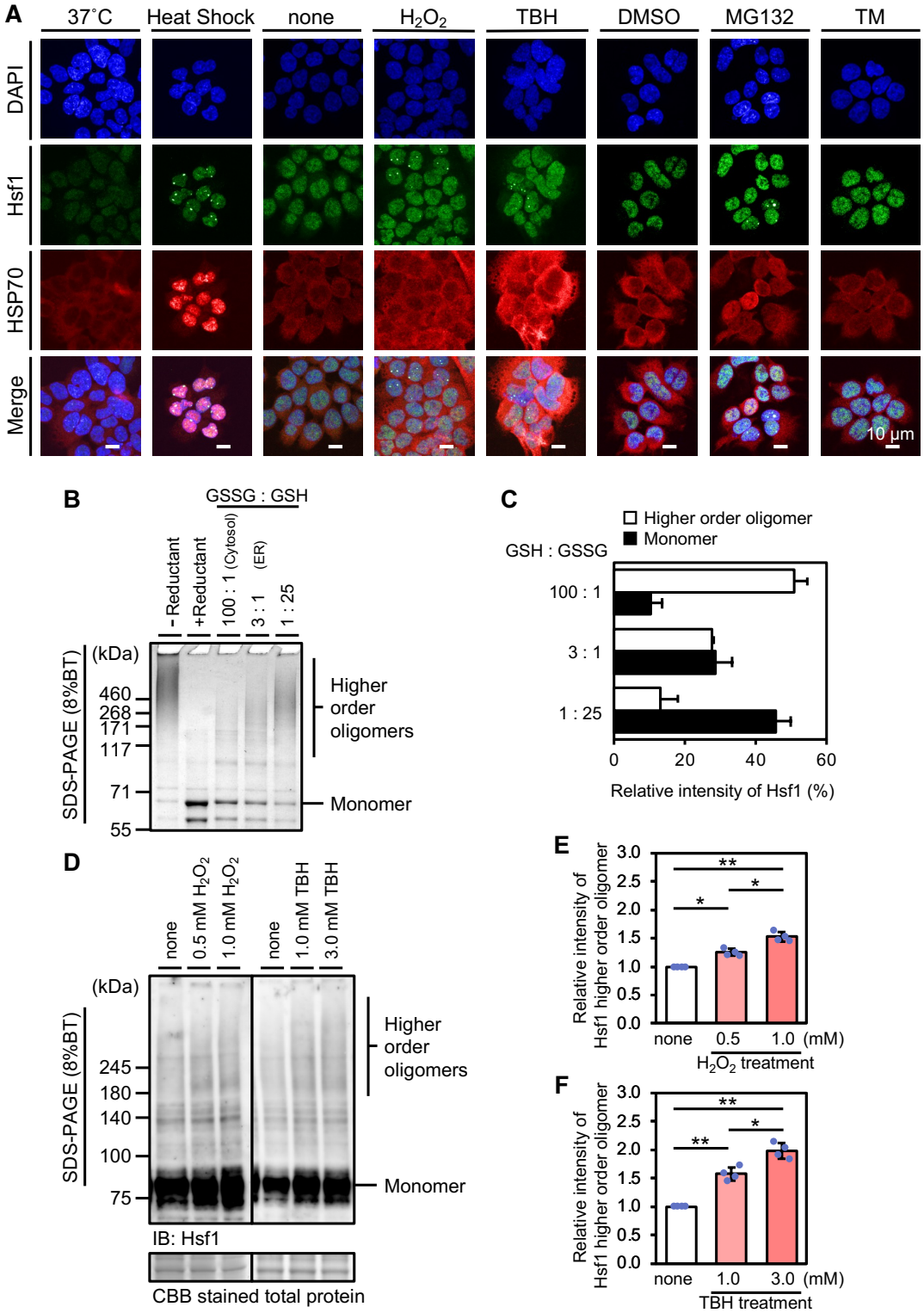
A
37˚C
Heat Shock
none
H2O2
TBH
DMSO
MG132
TM
DAPI
Hsf1
HSP70
Merge
10 μm
B
GSSG : GSH
- Reductant
+Reductant
100 : 1 (Cytosol)
3 : 1 (ER)
1 : 25
(kDa)
460
268
171
117
71
55
SDS-PAGE (8%BT)
Higher order oligomers
Monomer
C
Higher order oligomer
Monomer
GSH : GSSG
100 : 1
3 : 1
1 : 25
0
20
40
60
Relative intensity of Hsf1 (%)
D
none
0.5 mM H2O2
1.0 mM H2O2
none
1.0 mM TBH
3.0 mM TBH
(kDa)
245
180
140
100
75
SDS-PAGE (8%BT)
Higher order oligomers
Monomer
IB: Hsf1
CBB stained total protein
E
Relative intensity of Hsf1 higher order oligomer
3.0
2.5
2.0
1.5
1.0
0.5
0.0
**
*
*
none
0.5
1.0 (mM)
H2O2 treatment
F
Relative intensity of Hsf1 higher order oligomer
3.0
2.5
2.0
1.5
1.0
0.5
0.0
**
**
*
none
1.0
3.0 (mM)
TBH treatment

Figure 5.1 Redox dependent Hsf1 droplet formation and oligomerization of Hsf1 in cell
(A) Confocal immunofluorescence images showing the subcellular localization and foci formation of Hsf1 in HAP1 cells (scale bar, 10 μm). Cells were co-stained with an antibody to HSP70 and with DAPI. Cells were treated with various stress conditions: 43°C heat shock for 1 h, 1.0 mM H_2O_2 for 1 h, 3.0 mM TBH for 1 h, 2 μM MG132 or 2 μg/mL tunicamycin (TM) for 2 h. (B) Oligomeric states of Hsf1 in redox buffers, 5 μM Hsf1 were incubated without reductant (−Reductant), with 10 mM DTT (+Reductant), or in the presence of redox buffers (GSH : GSSG = 100 : 1, 3 : 1, 1 : 25) at 37˚C. Samples were quenched by addition of NEM, and samples were separated by SDS-PAGE using an 8% gel. (C) Quantification of the relative band intensities of the higher-order oligomer forms of Hsf1 compared to the band intensity of -Reductant lane (white bar graphs) and the monomer forms of Hsf1 compared to the band intensity of +Reductant lane (black bar graphs) in C. Error bars correspond to the means ± s.d. of three independent experiments. (D) Oligomeric states of intracellular Hsf1 under oxidative stress. HAP1 cells were treated with a oxidant (H_2O_2 or TBH). Cell lysates were separated with SDS-PAGE and visualized with anti-Hsf1 antibody. (E, F) Quantification of the relative signal intensities of the higher-order oligomer forms of Hsf1 compared to the signal intensity of none in D. Error bars correspond to the means ± s.d. of four independent experiments. Data were analyzed for statistical significance using the Tukey-Kramer test. *, $p < 0.05$, **, $p < 0.01$.

5.3.2 Droplet Formation of Hsf1 under Crowding Condition

I have shown that the formation of nSBs and changes in the association state of Hsf1 occur in response to the redox environment. Next, I further investigated the effect of redox environment to Hsf1 droplet *in vitro*. I demonstrated the acidification-induced phase separation of Hsf1 in chapter IV, but in this chapter, I examined the droplet formation under adding of the crowding agents because the exchange reaction of disulfide bonds between cysteine residues are unlikely to occur at acidic pH *in vitro*. Notably, the enzymes such as PDI could promote the exchange reaction at acidic pH in cell. Enhanced LLPS droplet formation under crowding conditions observed for Hsf1 was consistent with previous reports on other low-complexity proteins demonstrating that LLPS was enhanced by the excluded volume effect of the molecular crowders[18–21]. To verify whether Hsf1 forms liquid-like droplets, purified Hsf1 solutions under crowding conditions were observed under a microscope. It was observed that the addition of a molecular crowder ficoll 400 to Hsf1 solution makes it turbid, which was associated with the droplet formation following microscopic observation (Figure 5.2A). Differential interference contrast microscopy images revealed that droplets having round, globular shape were formed in the solution. The incorporation of Hsf1 in the droplet was verified

by confocal microscopy of the droplets formed in the presence of 0.1 equivalent Hsf1-green fluorescent protein (GFP), showing GFP-derived fluorescence in the droplets (Figure 5.2A). The time-lapse imaging of the droplets using a confocal microscope demonstrated that the droplets fused with each other in approximately 1–2 min (Figure 5.2B), indicating that the internal mobility of Hsf1 droplets enables the rearrangement of Hsf1 molecules. The mobility of Hsf1 molecule in the droplet was also examined using fluorescence recovery after photobleaching (FRAP) analysis (Figure 5.2C)[22], where a small segment of the droplet was bleached and the degree of the fluorescence recovery was monitored. Approximately 25% of signal intensity was recovered within 140 sec (Figure 5.2C). The collected data indicated that Hsf1 droplets are formed via LLPS and are characterized by adequate mobility to fuse with each other under reductive conditions (Figure 5.2B, C). Importantly, it was confirmed that the addition of other crowding agents, including polyethylene glycol (PEG) 8000 and dextran 200, also results in the formation of Hsf1 droplets (Figure 5.2A). Thus, the data show that Hsf1 has the ability to form LLPS droplet in a crowding environment. Moreover, a higher concentration of Hsf1 decreased the critical concentration of the crowder for droplet formation (Figure 5.2D), indicating that an increase in the Hsf1 concentration in the crowding environment can trigger droplet formation. Given the fact that Hsf1 is translocated to the nucleus in the stressed condition, an increase in the local concentration of Hsf1 can trigger droplet formation in cell.

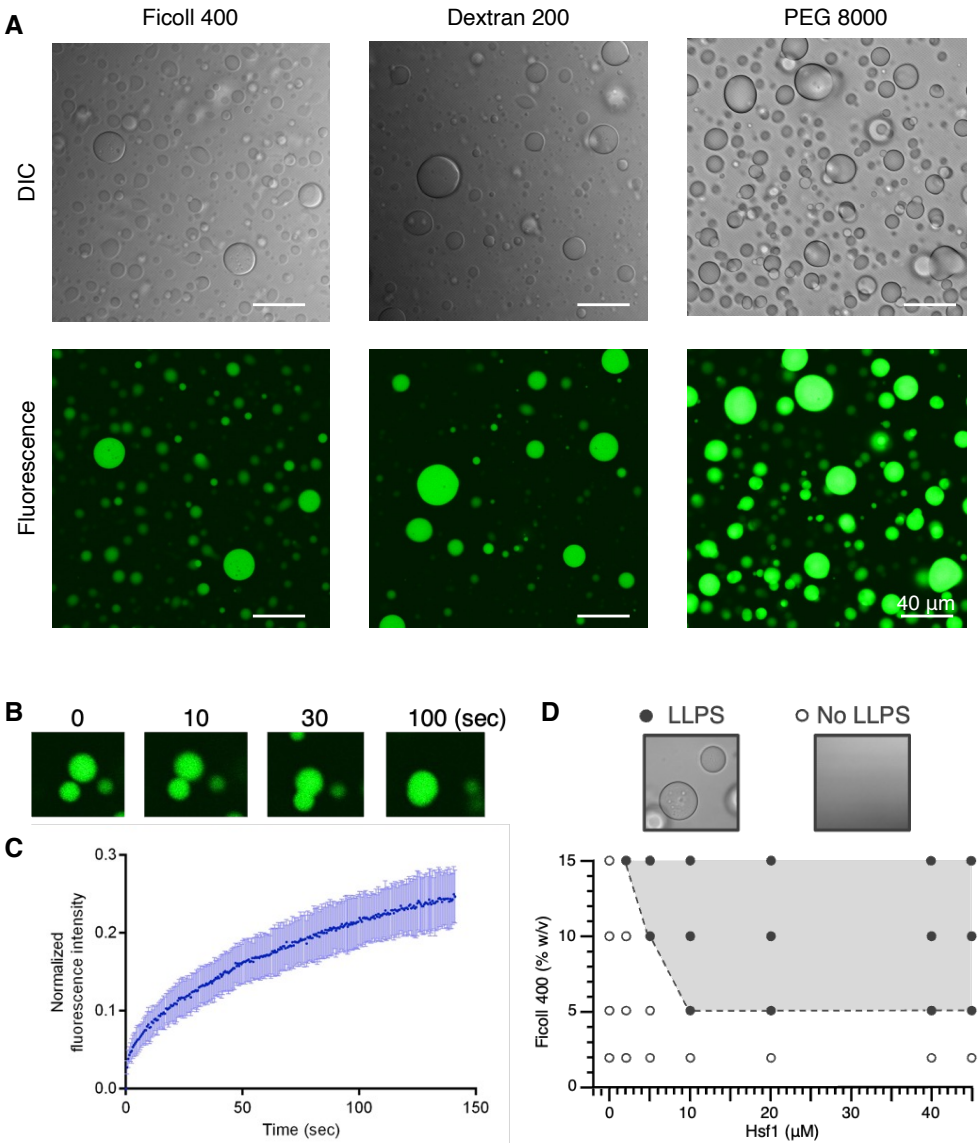

Figure 5.2 Droplet formation of Hsf1 under crowding condition
(A) Representative images of differential interference contrast and fluorescence demonstrating the droplets formed by 45 μM Hsf1 with 0.1 eq Hsf1-GFP in the presence of 10% (w/v) ficoll 400, dextran 200, or PEG 8000. Scale bar, 40 μm. (B) Time-lapse fluorescence microscopy demonstrating fusion dynamics of Hsf1-GFP droplets. (C) FRAP of a small segment of the droplets is used to evaluate the internal mobility of Hsf1 droplets. The bleached event occurs at 0 sec. The post-irradiation fluorescence intensity was normalized by the difference in the intensity before irradiation and the intensity of the first frame immediately after irradiation as one and recovery of the post-irradiation fluorescence intensity was analyzed. Data were plotted as mean ± s.d., with n = 7 independent experiments. (D) Phase diagram of Hsf1 LLPS (Hsf1 concentration versus ficoll 400 concentration). A representative example of LLPS, containing Hsf1 40 μM, ficoll 400 15% (w/v), and a representative example of no LLPS, containing Hsf1 2 μM, ficoll 400 2% (w/v) are presented.

5.3.3 Redox-dependent Phase Transition of Hsf1 Droplets in vitro

To evaluate the effect of oxidative conditions on the Hsf1 droplets, the shape and fluidity of the droplets under reductive and oxidative conditions were examined *in vitro*. The Hsf1 droplets were observed to be distorted in the absence of the reducing agent (Figure 5.3A, C, D). These distorted shapes are a characteristic property of LLPS droplets modified from mobile to immobile gel-like states[23], indicating that Hsf1 droplets undergo phase transition in oxidative conditions. Furthermore, the shape distortion of Hsf1 droplets was monitored in the presence of H_2O_2 (Figure 5.3E). FRAP studies were also performed to investigate the internal mobility of Hsf1 droplets under oxidative and reductive conditions. These studies revealed that the degree of fluorescence recovery of Hsf1 droplets in oxidative conditions was lower compared with that under reductive conditions, demonstrating the decreased internal mobility of Hsf1 molecules in the droplet in oxidative conditions (Figure 5.3B). Based on the above findings regarding the shape and internal mobility of the droplets, I concluded that Hsf1 droplets undergo phase transition from liquid to a gel-like state in oxidative conditions.

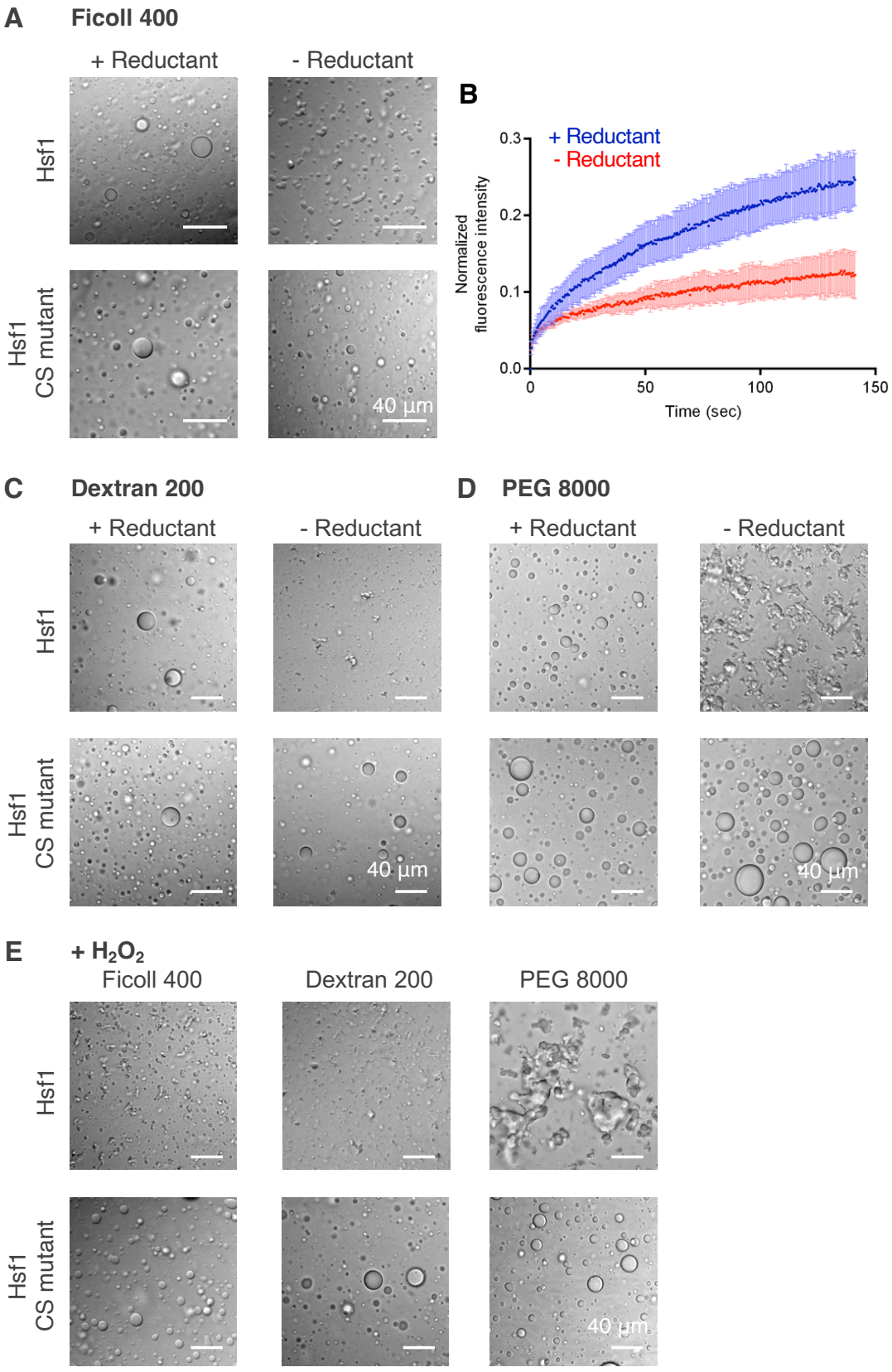
A
Ficoll 400
+ Reductant
- Reductant
Hsf1
Hsf1 CS mutant
40 µm
B
+ Reductant
- Reductant
Normalized fluorescence intensity
0.3
0.2
0.1
0.0
0
50
100
150
Time (sec)
C
Dextran 200
+ Reductant
- Reductant
Hsf1
Hsf1 CS mutant
40 µm
D
PEG 8000
+ Reductant
- Reductant
40 µm
E
+ H2O2
Ficoll 400
Dextran 200
PEG 8000
Hsf1
Hsf1 CS mutant
40 µm

Figure 5.3 Redox-dependent phase transition of Hsf1 droplet
(A) Differential interference contrast images of Hsf1 droplets and Hsf1 CS mutant droplets in the presence of 10% (w/v) ficoll 400. The left panels correspond to 10 mM DTT (+ Reductant) incubations and the right panels correspond to samples in absence of reductant (− Reductant). Scale bar, 40 μm. (B) FRAP data demonstrating the decreased fluidity of Hsf1 droplet under oxidative conditions. The bleached event occurs at 0 sec. Data are plotted as means ± s.d., with n = 7 independent experiments. (C, D) Differential interference contrast images of Hsf1 droplets and Hsf1 CS mutant droplets in the presence of 10% (w/v) dextran 200 (C) or PEG 8000 (D). Left and right panels represent the images of Hsf1 in the presence (+ Reductant) and absence (− Reductant) of 10 mM DTT, respectively. Hsf1 droplets have a round globular shape under reductive conditions and a distorted gel-like shape under oxidative conditions. On the other hand, the droplets of Hsf1 CS mutant have a round globular shape in all conditions. (E) Differential interference contrast images of Hsf1 droplets and Hsf1 CS mutant droplets in the presence of 10 mM H_2O_2. As a crowder, 10% (w/v) ficoll 400 (left panels), 10% (w/v) dextran 200 (center panels), and 10% (w/v) PEG 8000 (right panels) were used for droplet formation. Hsf1 droplets have a distorted gel-like shape, while Hsf1 CS mutant droplets have a round globular. Scale bar, 40 μm.

Although it is recognized that Hsf1 senses heat stress directly[24–26], the redox sensing by Hsf1 is poorly understood. Redox conditions can be sensed by Cys residues that are able to form intermolecular or intramolecular disulfide bonds. Hsf1 contains five cysteine residues, which are highly conserved in mammals (Figure 5.4), and intermolecular disulfide bond formation in stress response has been reported[24,25], suggesting that these five cysteine residues could sense the redox conditions. To evaluate the effect of disulfide bond formation on the properties of Hsf1 droplets, the Hsf1 CS mutant wherein all five Cys residues were replaced with Ser residues was prepared and subjected to microscopic observation. Accordingly, Hsf1 CS mutant droplet shapes remained spherical, even under oxidative conditions (Figure 5.3B, D-F), indicating that the Cys residues of Hsf1 can be critical in sensing redox environments.

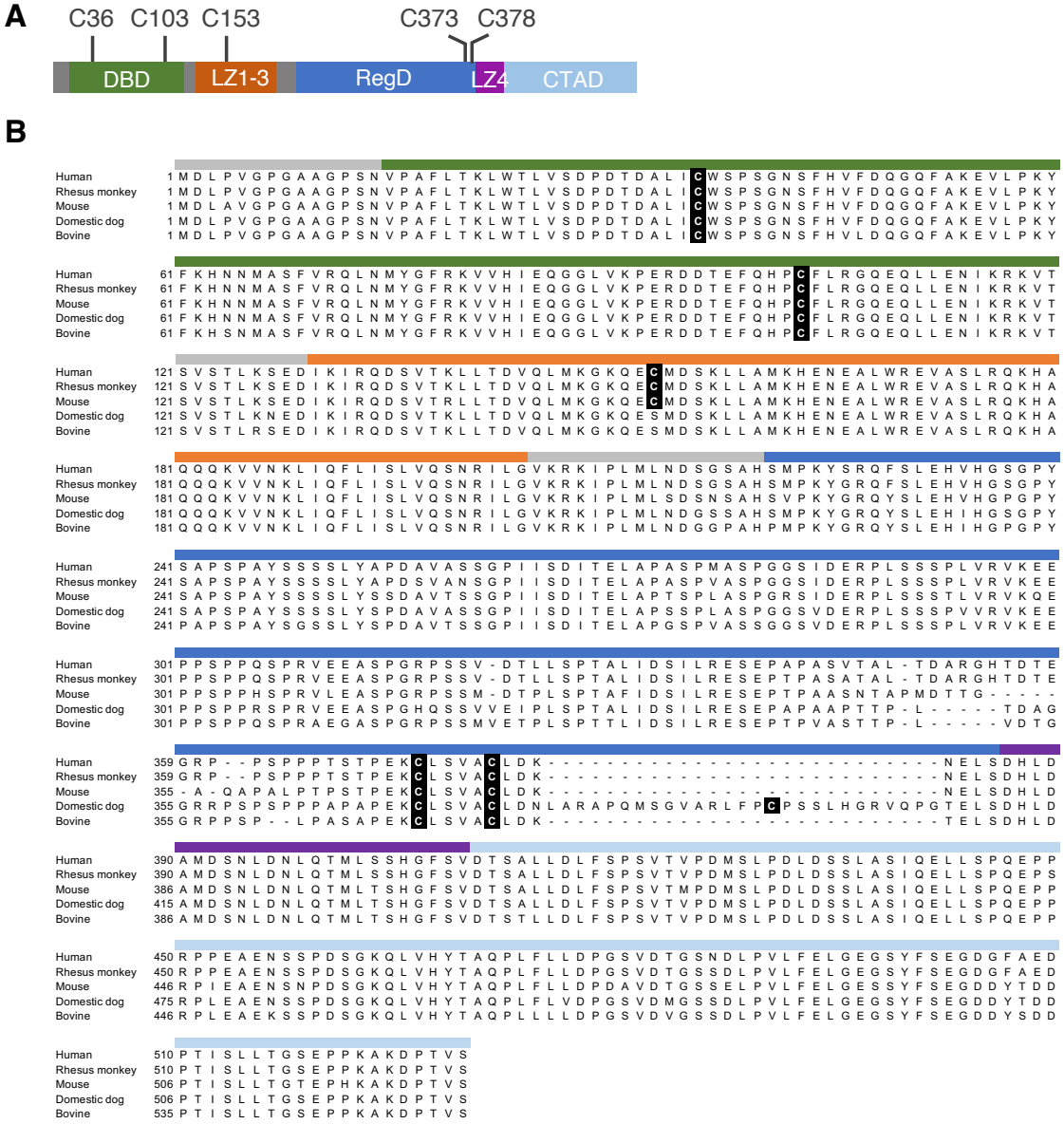

Figure 5.4 Conservation of the amino acid residues of Hsf1
(A) Domain organization and location of cysteine residues in Hsf1. (B) Multiple sequence alignment for Hsf1 from a variety of organisms, human (*Homo sapiens*, Q00613), rhesus monkey (*Macaca mulatta*, A0A5K1U5D2), mouse (*Mus musculus*, P38532), domestic dog (*Canis lupus familiaris*, F1PDU7), and bovine (*Bos taurus*, Q08DJ8). Cysteine residues are highlighted in black.

5.3.4 Oxidative Environments Promote Accumulation of Highly Condensed Structures inside the Hsf1 Droplets

As presented above, it was discovered that Hsf1 droplets undergo a redox-dependent phase transition. To uncover the mechanism of phase transition, HT imaging, an approach that can visualize the internal structure of the droplet based on the refractive index (RI), was exploited[27]. Hsf1 droplets that were formed after addition of ficoll 400 were observed under a HT microscope (Figure 5.5). As observed in confocal microscopy (Figure 5.3), HT imaging also showed that the shape of Hsf1 droplets was round and globular under reductive conditions and distorted under oxidative conditions (Figure 5.5A). In addition, quantitative evaluation of RI values was performed to investigate the distribution of Hsf1 molecules inside the droplet. RI mapping of the droplets demonstrated that RI values were not uniform, but the regions with higher RI values were sporadically scattered in the droplets. This distribution pattern of RI values implies the heterogeneous distribution of Hsf1 molecules in the droplet (Figure 5.5B). Regions with higher RI values are expected to contain higher concentrations of Hsf1, suggesting the presence of "core particles" in the droplets. Interestingly, comparison between RI mapping under reductive and oxidative conditions indicated that droplets under oxidative conditions have higher content of the core particles compared to those in reductive conditions (Figure 5.5B). The scatter plot of the mean RI values for each droplet revealed that droplets at under oxidative conditions contain significantly higher mean RI values compared to those under reductive conditions (Figure 5.5C), indicating that droplets under oxidative conditions have higher average Hsf1 concentrations. Importantly, the higher density and content of core particles in the oxidative droplets can be key features in understanding the mechanism of their phase transition. The presented data thus suggest that the tighter packing of Hsf1 molecules forming core particles leads to gel-like droplet properties.

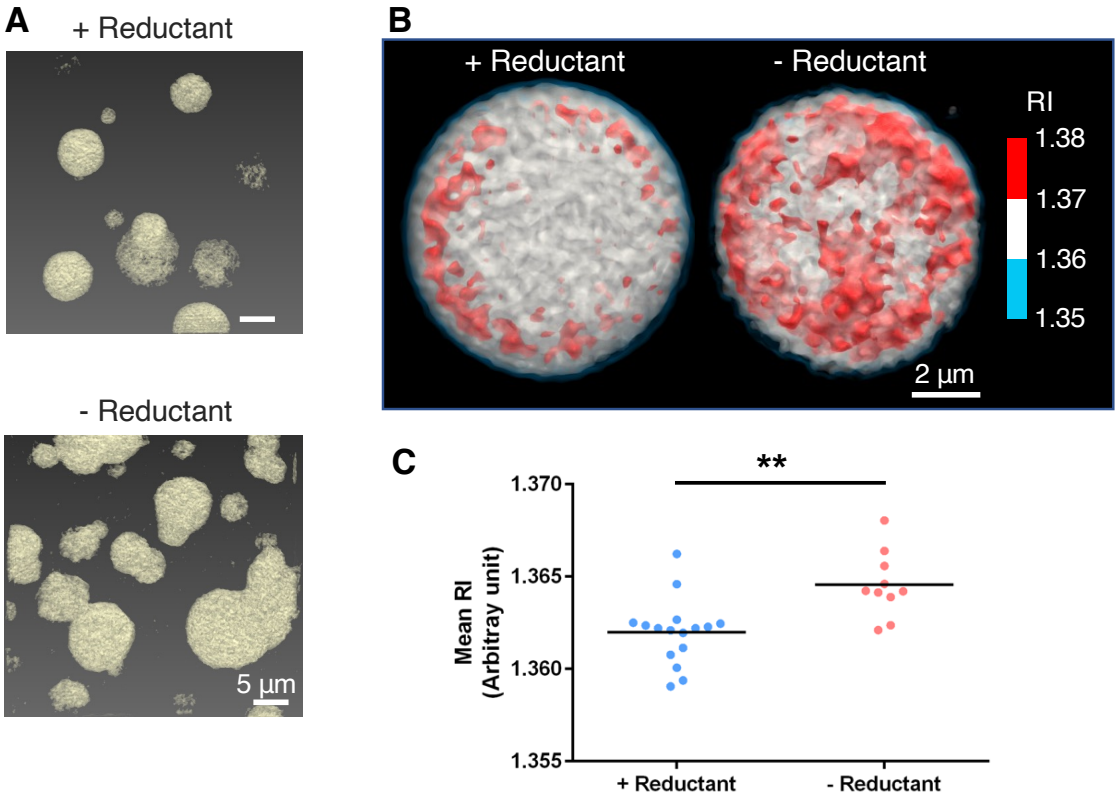

Figure 5.5 Observation of internal state of Hsf1 droplets using a holographic tomography microscope
(A) 3D RI images of Hsf1 droplets. Left and right panel correspond to the RI images of Hsf1 droplets in the presence or absence of 10 mM DTT (+, − Reductant), respectively. The areas with RI above 1.353 are colored in yellow. (B) Quantitative analysis of tomographic images, measuring the mean RI of the Hsf1 droplets in the presence of 10 mM DTT (+ Reductant) and in the absence of reductant (− Reductant). (C) A scatter plot of mean RI of Hsf1 droplet in the presence or absence of 10 mM DTT (+, − Reductant) with N = 16 (+ Reductant) and 10 (− Reductant). Each plot presents the mean RI of the average of the individual droplets. **, $p < 0.01$, statistical significance among mean RI values in the absence or presence of the reductant.

5.3.5 Enhanced Oligomerization of Hsf1 through Disulfide Bonds

HT imaging revealed that Hsf1 droplets under oxidative conditions are characterized by enhanced formation of the core particles with higher density. To unveil the mechanism of the enhanced formation of the core particles under oxidative conditions, SEC-MALS was exploited to investigate the oligomeric state of Hsf1 molecules in solution under reductive and oxidative conditions (Figure 5.6A–C). The Hsf1 solution in the absence of the crowding reagent was subjected to SEC-MALS. Under reduced

conditions, the elution profile of Hsf1 in the gel filtration chromatography was highly symmetric (Figure 5.5A). The median molar mass of Hsf1 at an injection concentration of 50 μM was measured to be 379 kDa, corresponding to approximately a 7-mer (Figure 5.6A, D). On the other hand, under oxidative conditions, the elution peak turned asymmetric, and the median molar mass increased to 540 kDa, corresponding to approximately a 9-mer (Figure 5.6B, D). Furthermore, the data demonstrated that the majority of Hsf1 was found as larger oligomers up to approximately a 16-mer under oxidative conditions. Hsf1 CS mutants under oxidative conditions did not form such higher-order oligomers and their median molar mass was 308 kDa, corresponding to approximately a 5-mer (Figure 5.6C, D). To verify that this higher-order oligomer was formed through intermolecular disulfide bonds between Hsf1 molecules, sodium dodecyl sulfate–polyacrylamide gel electrophoresis (SDS-PAGE) was performed. N-ethylmaleimide (NEM) quenched non-reducing SDS-PAGE revealed that disulfide-bonded higher-order oligomers (higher than 460 kDa) were detected only for wild type Hsf1 prepared under oxidative conditions (Figure 5.6E). The data thus suggest that Hsf1 under oxidative conditions forms larger oligomers mediated by disulfide bonds that consequently form the core particles in the droplets.

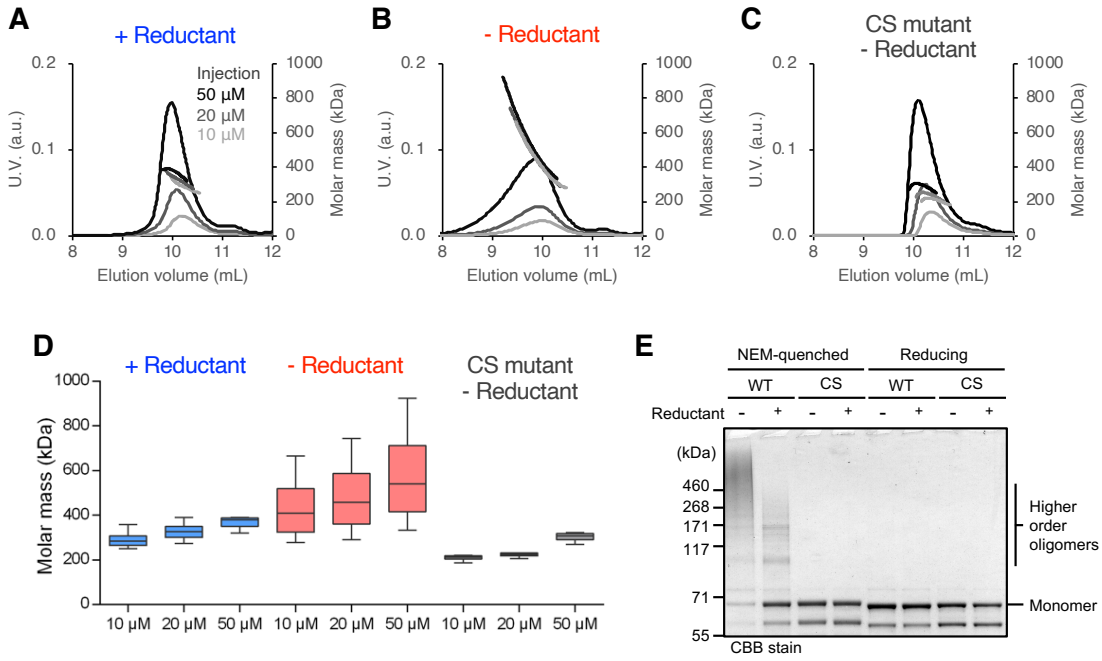

Figure 5.6 Oxidative oligomerization of Hsf1

(A, B) SEC-MALS of Hsf1 in the presence (A) or absence (B) of 10 mM DTT. SEC-MALS experiments were performed using a range of injection concentrations: 10 µM (light gray), 20 µM (dark gray), and 50 µM (black). (C) SEC-MALS of Hsf1 CS mutant in the absence of the reductant. SEC-MALS experiments were performed with a range of injection concentration: 10 µM (light gray), 20 µM (dark gray), and 50 µM (black). (D) A box and whisker plot of Hsf1 molar mass at various conditions. (E) SDS-PAGE used for evaluation of the redox states of Hsf1. Hsf1 was incubated in the absence or presence of DTT. Samples were quenched by a large excess of NEM (NEM quenched) or by SDS-sample buffer containing a reductant (reducing), and samples were then separated by SDS-PAGE. Reductant (−/+) corresponds to the Hsf1 in the presence or absence of DTT, respectively.

5.4. Discussion

The phase transition to gel-like state of Hsf1 droplet is a critical event in cell fate decision. However, due to the scarcity of *in vitro* studies, the exact mechanism of phase transition remained uncovered. The data showed that Hsf1 droplet were formed in the cultured cells in response to oxidative stress (Figure 5.1A). Interestingly, microscopic observations and FRAP measurements demonstrated that the fluidity of the Hsf1 droplets was modified in redox conditions, causing the droplets to undergo phase transition from fluid to a gel-like state under oxidative conditions *in vitro* (Figure 5.3A, B). This observation indicates the mechanism of phase transition of Hsf1 droplets under continuous stress[1] where cytosol becomes oxidative due to excessive ROS generation[4–6]. Since phase transition of hsf1 droplets leads to apoptosis[1], the present study's data suggest that oxidative phase transition of Hsf1 is a key factor responding to continuous stress for the regulation of apoptosis.

Importantly, the investigation of the internal architecture of the Hsf1 droplet by HT imaging unveiled the phase transition mechanism (Figure 5.5E). RI imaging demonstrated that Hsf1 molecules were heterogeneously distributed in the droplet, forming core particles with higher density. Furthermore, the data showed that oxidative conditions induced the formation of core particles, therefore leading to more condensed droplets (Figure 5.5B, C). Moreover, SEC-MALS data showed that under oxidative conditions Hsf1 molecules formed larger disulfide-linked oligomers (Figure 5.6B, D, E). The oligomers observed in the SEC-MALS experiments represent the tight oligomeric units that weakly interact with each other when they drive droplet formation (Figure 5.7). Larger oligomeric units are expected to have a higher affinity to other oligomeric units, resulting in higher Hsf1 density to form core particles and consequently, reduced mobility of the Hsf1 molecules in the droplet (Figure 5.7). Indeed, SDS-PAGE data showed that the Cys residues in Hsf1 directly sense changes in the redox environment and modulate the population of the disulfide-linked oligomers of Hsf1 and their intracellular population

also change in response to oxidative stress (Figure 5.1B-F), suggesting that Hsf1 responds to the redox environment change in the cell by modulating disulfide-bonded oligomers. The formation of intermolecular disulfide bonds in cells by heat treatment supports this hypothesis significantly[25]. Additionally, because the Cys residues in Hsf1 have been reported to form intramolecular as well as intermolecular disulfide bonds[24,25], the compaction of a Hsf1 molecule by intramolecular disulfide bonds can also accelerate oligomerization. Taken together, a mechanism of Hsf1 phase transition is proposed as follows: In oxidative conditions, the synergistic effect of the intermolecular and intramolecular disulfide bonds of Hsf1 tighten the interactions between the Hsf1 oligomers to promote the formation of core particles (Figure 5.7). The increased core particle formation ultimately results in higher density and lower fluidity within the droplet. This mechanism of redox condition-dependent phase transition of Hsf1 droplets can explain the phase transition of Hsf1 droplets under continuous stress and potentially mediates the cell fate decision.

Furthermore, the data obtained in this study revealed that Hsf1 oligomers are larger than those described in the previous schemes[28–30]. The conventional models describe that Hsf1 exists as a monomer in the cytoplasm under normal conditions, while stressed conditions induce trimerization, leading to its translocation in the nucleus[28,30–32]. Alternatively, several previous studies using electrophoresis and gel filtration column chromatography indicated that Hsf1 forms a larger oligomer than trimer[25,33,34]. In the present study, the quantitative analysis of oligomers in solution using SEC-MALS demonstrated that Hsf1 forms oligomers with a median mass of a 7-mer in reductive conditions and a median mass of a 9-mer in oxidative conditions, with up to approximately a 16-mer in oxidative conditions. In the oxidative conditions, such "hyperoligomerization" can be particularly important in driving the phase transition of the Hsf1 droplets.

Since nSBs comprise RNA polymerase II and bromodomain-containing protein

4 (BRD4), the redox-dependent phase transition of Hsf1 is expected to perturb the activity of these components. Both RNA polymerase II and BRD4 are involved in the transcription of the satellite III RNA[35,36] and assembly of other nSB components as well as the associated DNA/RNA metabolism, biosynthesis, stress response, and cell cycle[37,38]. Hsf1 may affect the regulation of these cellular events through redox-dependent phase transition, modulating the intracellular stress response system and thus cell fate decision.

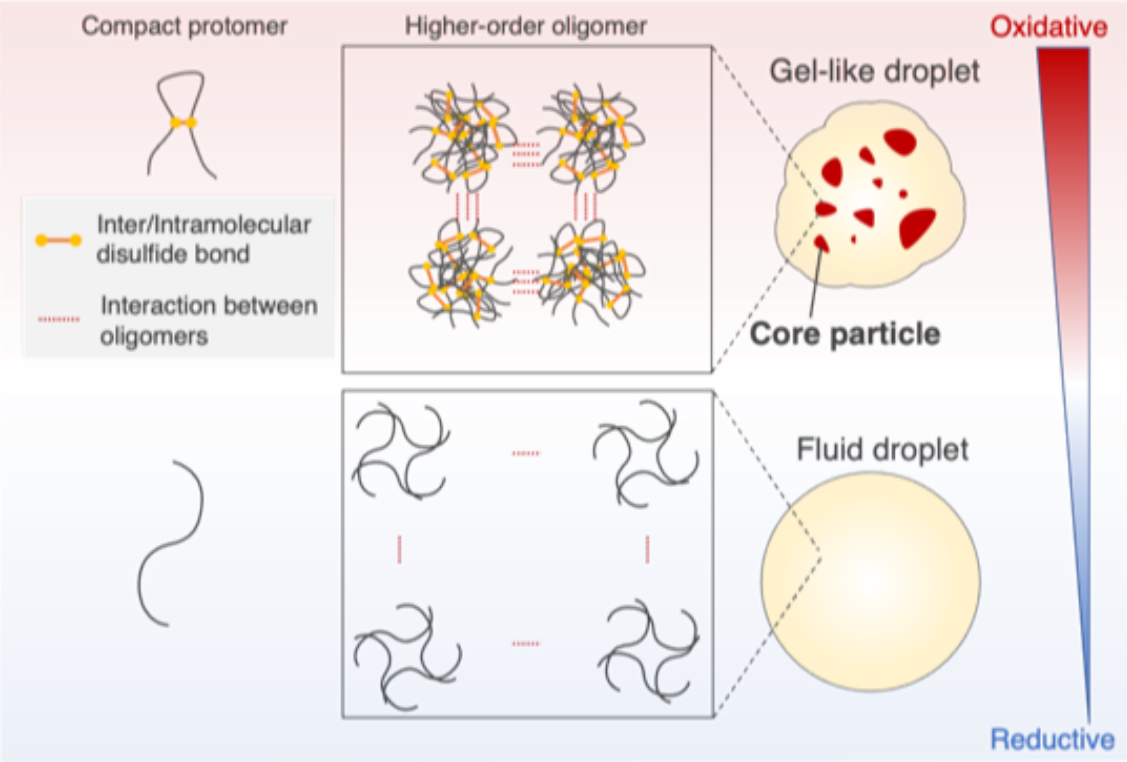

Figure 5.7 The proposed phase transition mechanism of Hsf1 droplet
Hsf1 undergoes phase transition to gel-like droplet in a redox-dependent manner. The synergistic effect of the Hsf1 oligomer packing by disulfide bonds and an increase in intermolecular interactions due to the formation of larger oligomers induced the formation of core particles, which eventually resulted in a higher density and lower fluidity inside the Hsf1 droplet.

References

1. Gaglia, G. *et al.* HSF1 phase transition mediates stress adaptation and cell fate decisions. *Nat. Cell Biol.* **22** 151–158 (2020).
2. Pakos-Zebrucka, K. *et al.* The integrated stress response. *EMBO Rep.* **17**, 1374–1395 (2016).
3. Lee, M. *et al.* Label-free optical quantification of structural alterations in Alzheimer's disease. *Sci. Rep.* **6**, 1–7 (2016).
4. Wang, Y. *et al.* HO-1 reduces heat stress-induced apoptosis in bovine granulosa cells by suppressing oxidative stress. *Aging* **11**, 5535–5547 (2019).
5. Maharjan, S., Oku, M., Tsuda, M., Hoseki, J. & Sakai, Y. Mitochondrial impairment triggers cytosolic oxidative stress and cell death following proteasome inhibition. *Sci. Rep.* **4**, 1–11 (2014).
6. Liu, G. *et al.* Caspase-Dependent and Caspase-Independent Pathways Are Involved in Cadmium-Induced Apoptosis in Primary Rat Proximal Tubular Cell Culture. *PLoS One* **11**, e0166823 (2016).
7. Laemmli, U. K. Cleavage of Structural Proteins during the Assembly of the Head of Bacteriophage T4. *Nature* **227**, 680–685 (1970).
8. Fujimoto, T., Inaba, K. & Kadokura, H. Methods to identify the substrates of thiol-disulfide oxidoreductases. *Protein Sci.* **28**, 30–40 (2019).
9. Schindelin, J. *et al.* Fiji: an open-source platform for biological-image analysis. *Nat. Methods* **9**, 676–682 (2012).
10. Jolly, C. *et al.* In vivo binding of active heat shock transcription factor 1 to human chromosome 9 heterochromatin during stress. *J. Cell Biol.* **156**, 775–781 (2002).
11. Sarge, K. D., Murphy, S. P. & Morimoto, R. I. Activation of heat shock gene transcription by heat shock factor 1 involves oligomerization, acquisition of DNA-binding activity, and nuclear localization and can occur in the absence of stress. *Mol. Cell. Biol.* **13**, 1392–1407 (1993).
12. Jolly, C., Usson, Y. & Morimoto, R. I. Rapid and reversible relocalization of heat shock factor 1 within seconds to nuclear stress granules. *Proc. Natl. Acad. Sci. U S A* **96**, 6769–6774 (1999).
13. Mähl, P., Lutz, Y., Puvion, E. & Fuchs, J.-P. Rapid Effect of Heat Shock on Two Heterogeneous Nuclear Ribonucleoprotein-associated Antigens in HeLa Cells. *J. Cell Biol.* **109**, 1921–35 (1989).
14. Bass, R., Ruddock, L. W., Klappa, P. & Freedman, R. B. A Major Fraction of Endoplasmic Reticulum-located Glutathione Is Present as Mixed Disulfides with Protein. *J. Biol. Chem.* **279**, 5257–5262 (2004).
15. Mochizuki, A. *et al.* Balanced Regulation of Redox Status of Intracellular Thioredoxin Revealed by in-Cell NMR. *J. Am. Chem. Soc.* **140**, 3784–3790 (2018).
16. Hatori, Y. *et al.* Visualization of the Redox Status of Cytosolic Glutathione Using the Organelle- and Cytoskeleton-Targeted Redox Sensors. *Antioxidants* **9**, 129 (2020).
17. Gutscher, M. *et al.* Real-time imaging of the intracellular glutathione redox potential. *Nat. Methods* **5**, 553–559 (2008).
18. André, A. A. M. & Spruijt, E. Liquid–Liquid Phase Separation in Crowded Environments. *Int. J. Mol. Sci.* **21**, 5908 (2020).
19. Wegmann, S. *et al.* Tau protein liquid–liquid phase separation can initiate tau aggregation. *EMBO J.* **37**, e98049 (2018).
20. Ray, S. *et al.* α-Synuclein aggregation nucleates through liquid–liquid phase separation. *Nat. Chem.* **12**, 705–716 (2020).
21. Boehning, M. *et al.* RNA polymerase II clustering through carboxy-terminal domain phase separation. *Nat. Struct. Mol. Biol.* **25**, 833–840 (2018).
22. Kato, M. *et al.* Cell-free formation of RNA granules: Low complexity sequence domains

form dynamic fibers within hydrogels. *Cell* **149**, 753–767 (2012).
23. Mateju, D. *et al.* An aberrant phase transition of stress granules triggered by misfolded protein and prevented by chaperone function. *EMBO J.* **36**, 1669–1687 (2017).
24. Manalo, DJ., Lin, Z. & Liu, A. Y.-C. Redox-Dependent Regulation of the Conformation and Function of Human Heat Shock Factor 1. *Biochemistry* **41**, 2580–2588 (2002).
25. Lu, M. *et al.* Two Distinct Disulfide Bonds Formed in Human Heat Shock Transcription Factor 1 Act in Opposition To Regulate Its DNA Binding Activity. *Biochemistry* **47**, 6007–6015 (2008).
26. Kmiecik, S. W., Breton, L. le & Mayer, M. P. Feedback regulation of heat shock factor 1 (Hsf1) activity by Hsp70-mediated trimer unzipping and dissociation from DNA. *EMBO J.* **39**, e104096 (2020).
27. Choi, W. H. *et al.* Aggresomal sequestration and STUB1-mediated ubiquitylation during mammalian proteaphagy of inhibited proteasomes. *Proc. Natl. Acad. Sci. USA* **117**, 19190–19200 (2020).
28. Neef, D. W., Jaeger, A. M. & Thiele, D. J. Heat shock transcription factor 1 as a therapeutic target in neurodegenerative diseases. *Nat. Rev. Drug Discov.* **10** 930–944 (2011).
29. Kmiecik, S. W. & Mayer, M. P. Molecular mechanisms of heat shock factor 1 regulation. *Trends Biochem. Sci.* **47**, 218–234 (2022).
30. Masser, A. E., Ciccarelli, M. & Andréasson, C. Hsf1 on a leash – controlling the heat shock response by chaperone titration. *Exp. Cell Res.* **396**, 112246 (2020).
31. Gomez-Pastor, R., Burchfiel, E. T. & Thiele, D. J. Regulation of heat shock transcription factors and their roles in physiology and disease. *Nat. Rev. Mol. Cell Biol.* **19** 4–19 (2018).
32. Åkerfelt, M., Morimoto, R. I. & Sistonen, L. Heat shock factors: integrators of cell stress, development and lifespan. *Nat. Rev. Mol. Cell Biol.* **11**, 545–555 (2010).
33. Hentze, N., le Breton, L., Wiesner, J., Kempf, G. & Mayer, M. P. Molecular mechanism of thermosensory function of human heat shock transcription factor Hsf1. *Elife* **5**, e11576 (2016).
34. Rossin, F. *et al.* TG2 regulates the heat-shock response by the post-translational modification of HSF1. *EMBO Rep.* **19**, e45067 (2018).
35. Hussong, M. *et al.* The bromodomain protein BRD4 regulates splicing during heat shock. *Nucleic Acids Res.* **45**, 382–394 (2017).
36. Col, E. *et al.* Bromodomain factors of BET family are new essential actors of pericentric heterochromatin transcriptional activation in response to heat shock. *Sci. Rep.* **7**, 1–12 (2017).
37. Ninomiya, K. *et al.* LncRNA-dependent nuclear stress bodies promote intron retention through SR protein phosphorylation. *EMBO J.* **39**, e102729 (2020).
38. Ninomiya, K. *et al.* m6A modification of HSATIII lncRNAs regulates temperature-dependent splicing. *EMBO J.* **40**, e107976 (2021).

CHAPTER VI

Conclusions

Hsf1-chaperone system contributes to maintaining the proteostasis through assisting productive protein folding[1]. In this thesis, to elucidate the molecular mechanism of the Hsf1-chaperone system, I focused on two reactions that occur within this system: (1) substrate protein folding assistance by chaperone (Chapter II), and (2) transcriptional induction of chaperones via stress-sensing assembly state changes of Hsf1 (Chapter III-V). Additionally, I showed that FKBP52, a PPIase, promotes Hsf1 assembly (Chapter IV), suggesting that the Hsf1-chaperone system involves (3) chaperone-mediated regulation of Hsf1 assembly. The results and conclusions drawn from experimental data are highlighted below

Structural Insight into Proline *cis/trans* Isomerization of Unfolded Proteins Catalyzed by PPIase (Chapter II)

In Chapter II, I focused on the PPIase activity to uncover the foldase mechanism of molecular chaperone because PPIase catalyzes the proline *cis/trans* isomerization that can be a rate-limiting step of protein folding[2]. The solution structure of TF chaperone, which has a PPIase domain (TF^{PPD})[3], in a complex with the client protein showed that TF^{PPD} recognizes the proline-aromatic motif located in the hydrophobic stretch of the unfolded client protein through its conserved hydrophobic cleft, which suggests that TF^{PPD} preferentially accelerates the isomerization of the peptidyl-prolyl bond that is eventually folded into the core of the protein in its native fold. Molecular dynamics simulation revealed that TF^{PPD} exploits the backbone amide group of I195 to form an intermolecular hydrogen bond with the carbonyl oxygen of the amino acid residue preceding the proline residue at the transition state, which presumably stabilizes the transition state and thus accelerates the isomerization. The importance of such intermolecular hydrogen bond formation during the catalysis was confirmed by the activity assay and NMR relaxation analysis. Therefore, PPIase activity of TF^{PPD} is expressed by lowering the activation energy of *cis/trans* isomerization of proline residues

in the hydrophobic region by intermolecular hydrogen bonding, revealing one aspect of the foldase mechanism of chaperone. Moreover, this is the first study from a view of structural chemistry that identify the active center of FKBP-type PPIase, to which TF^{PPD} belongs and which performs various functions in cell[4].

Stress-sensing Assembly State Changes of Hsf1 (Chapter III-V)

As described above, chaperones express their foldase function through PPIase activity to assist the protein folding. Since the amount of misfolded protein increases during stress, the Hsf1-chaperone system takes a countermeasure by upregulating the amount of chaperones having foldase function to prevent the accumulation of misfolded protein in the cell. The regulation of Hsf1 transcriptional activity is linked to a stress level-dependent stepwise state changes of Hsf1, with the monomeric form being transcriptionally inactive, while the oligomeric and liquid droplet state promotes chaperone transcription[5,6], and the gel-like droplet state causes a decrease in chaperone transcription and apoptosis[7]. I found that the steps of oligomerization, liquid-liquid phase separation (LLPS), and phase transition to gel-like droplets are caused by heat (Chapter III), acidification (Chapter IV), and oxidation (Chapter V), respectively. Heat-stressed cells often induce their acidification, and stresses such as heat and acidification are known to cause an oxidative condition in the intracellular environment due to the production of ROS[8,9]. Then, in the case of heat stress alone, the cell is under relatively weak stress, whereas as acidification and oxidative stress are added, the stress level in the cell would be higher. I propose that Hsf1 distinguishes the types of stress to sense intracellular stress levels, thereby regulating the transcriptional level of chaperones via changing its own assembly state.

I further investigated how the different types of stress sensing induce the assembly state changes of Hsf1, then I found a relationship between local reactions such as stress sensing-induced LZ4 folding/unfolding and disulfide bond formation and the

intermolecular interactions that drive the assembly process. In Chapter III, I examined the oligomerization mechanism, which is the first step in the assembly state changes of Hsf1. I revealed that Hsf1 monomer undergoes conformational change from closed state to open state and this conformational change is coupling with the heat-induced unfolding of LZ4. The dissociation of LZ4 from LZ1-3 by the LZ4 unfolding causes the intermolecular interactions between LZ1-3, leading to the oligomerization of Hsf1 (Figure 6.1). In Chapter IV, I investigated the mechanism of LLPS, which is the next process of Hsf1 oligomerization. LZ4 was disordered at neutral pH, while it formed a secondary structure and hydrophobic cluster at acidic pH. Since the full length of Hsf1 IDR formed liquid droplets at acidic pH, while IDR ΔLZ4 could no longer undergo LLPS, I proposed that intermolecular interactions between LZ4 coupling with acidification-induced LZ4 folding drive the LLPS of Hsf1 (Figure 6.1). Therefore, the results of chapters III and IV indicate that the changes in the tertiary structure and even the quaternary structure of Hsf1, are controlled by changes in the secondary structure of LZ4. In Chapter V, I examined the mechanism of the phase transition of Hsf1 droplet to less fluid gel-like droplets induced by oxidation. In the oxidative condition, Hsf1 forms higher-order oligomer mediated by the disulfide-bond, and the intermolecular interaction between such oligomers leads the core particle in the Hsf1 droplet (Figure 6.1). The formation of these core particles is supposed to reduce the internal mobility of the droplets and leads to phase transition to gel-like droplet. The progress of the association state changes could be described as a process of enhanced intermolecular interactions. I propose that Hsf1 assembly events proceed by increasing the number of intermolecular interaction points such as LZ1-3/LZ1-3 interaction, LZ4/LZ4 interaction, and higher-order oligomer/higher-order oligomer interaction, coupling with stress-induced local reactions that are LZ4 folding/unfolding and disulfide bonds formation.

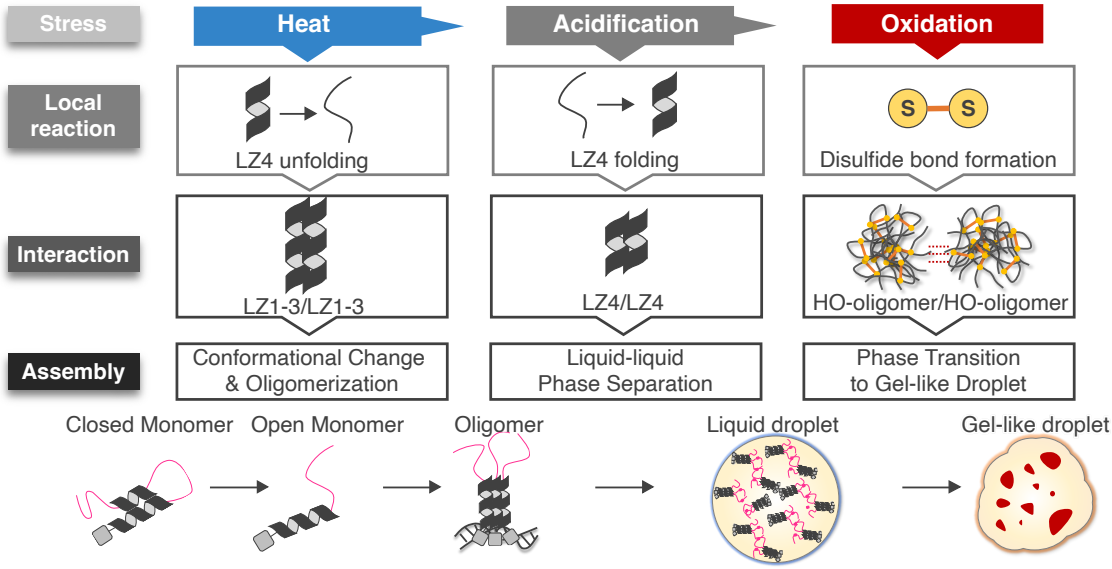

Figure 6.1 Proposed mechanism of Hsf1 state changes
Hsf1 changes its state by sensing temperature, pH, and redox conditions. While heat-induced LZ4 unfolding drives the conformational transition and oligomerization (Chapter III), acidification-induced LZ4 folding drives LLPS (Chapter IV). Hsf1 undergoes phase transition to gel-like droplet by intermolecular interaction between higher-order (HO) oligomers in the oxidative condition (Chapter V). Hsf1 mediates the cell fate decision by these stress-dependent state changes.

Feedback Regulation in Hsf1-Chaperone System and Future Perspectives

In this thesis, I revealed that the mechanisms of (1) substrate protein folding assistance by chaperone (Chapter II), and (2) transcriptional induction of chaperones via stress-sensing assembly state changes of Hsf1 (Chapter III-V). Furthermore, I found that FKBP52, a PPIase, promotes Hsf1 assembly in Chapter IV. Then, it was proposed that the Hsf1-chaperone system is not formed by the one-way flow of Hsf1 regulating transcription of chaperones and the synthesized chaperones functioning as foldases, but the cycle is generated by the reaction of (3) chaperone-mediated regulation of Hsf1 assembly (Figure 6.2). In this cycle, foldase such as FKBP52 would strengthen the transcriptional level of chaperones by promoting the LLPS of Hsf1. This positive feedback reaction could contribute to enhanced stress response of Hsf1-chaperone system.

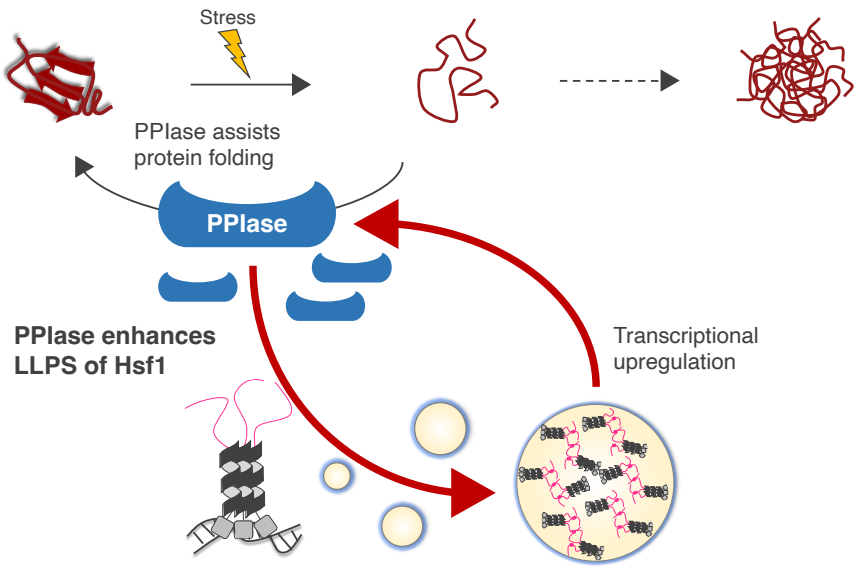

Figure 6.2 Feedback cycle in Hsf1-chaperone system
In the Hsf1-chaperone system, it was found that there is feedback cycle. Hsf1 regulates transcription of chaperones, the synthesized chaperones such as PPIase function as foldase, and chaperone enhances the regulation of Hsf1 assembly.

This study has revealed that local reactions of protein are involved not only in folding but also in assembly. Molecular chaperones may contribute to the maintenance of protein homeostasis by regulating molecular assembly through the control of local structure formation. Hsf1 regulates the transcription of various types of chaperones such as Hsp70, Hsp90, and Hsp110[1]. To elucidate the mechanism of the Hsf1-chaperone system, it is important to elucidate not only the mechanism of individual chaperones, but also the regulatory mechanism of Hsf1 assembly by chaperones and the feedback system in the Hsf1-chaperone system. Moreover, Hsf1 undergoes various post-translational modifications in the cell[5], then the studying how these post-translational modifications affect Hsf1 assembly and how multivalent interactions of Hsf1 drive the assembly will be important for understanding the real Hsf1 dynamics. More precise elucidation of the mechanism of the Hsf1-chaperone system will lead to a deeper understanding of the intracellular proteostasis that supports the basis of life.

References

1. Gomez-Pastor, R., Burchfiel, E. T. & Thiele, D. J. Regulation of heat shock transcription factors and their roles in physiology and disease. *Nat. Rev. Mol. Cell Biol.* **19** 4–19 (2018).
2. Wedemeyer, W. J., Welker, E. & Scheraga, H. A. Proline cis-trans isomerization and protein folding. *Biochemistry* **41**, 14637–14644 (2002).
3. Hoffmann, A., Bukau, B. & Kramer, G. Structure and function of the molecular chaperone Trigger Factor. *Biochim. Biophys. Acta.* **1803**, 650–61 (2010).
4. Storer, C. L., Dickey, C. A., Galigniana, M. D., Rein, T., Cox, M. B. FKBP51 and FKBP52 in Signaling and Disease. *Trends in Endocrinol. Metab.* **22**, 481–490 (2011).
5. Zhang, H. *et al.* Reversible phase separation of HSF1 is required for an acute transcriptional response during heat shock. *Nat. Cell Biol.* **24**, 340–352 (2022).
6. Kmiecik, S. W. & Mayer, M. P. Molecular mechanisms of heat shock factor 1 regulation. *Trends Biochem. Sci.* **47**, 218–234 (2022).
7. Gaglia, G. *et al.* HSF1 phase transition mediates stress adaptation and cell fate decisions. *Nat. Cell Biol.* **22** 151–158 (2020).
8. Triandafillou, C. G., Katanski, C. D., Dinner, A. R. & Allan Drummond, D. Transient intracellular acidification regulates the core transcriptional heat shock response. *Elife* **9**, 1–30 (2020).
9. Yang, K. *et al.* A redox mechanism underlying nucleolar stress sensing by nucleophosmin. *Nat. Commun.* **7**, 1–16 (2016).